Computational Mechanics of fracture on advanced aerospace structures

The University Of Sheffield.

by

Joaquín Navarro Zafra

Mechanical Engineering Department

University of Sheffield

A thesis submitted for the degree of

Doctor of Philosophy

2016, November

Declaration

I, Joaquín Navarro Zafra, declare that I have produced this thesis entitled, "Computational mechanics of fracture on advance aerospace structures" without the assistance of third parties and without making use of aids other than those specified.

The thesis work was conducted from June 2013 to November 2016 under the supervision of Dr. José Luis Curiel-Sosa at the University of Sheffield.

Sheffield, November

Abstract

In this thesis, the computational simulation of cracks in advanced composite structures subjected to biaxial loading is studied. A structural integrity analysis using the eXtended Finite Element Method (XFEM) is considered for simulating the crack behaviour of a chopped fibre-glass-reinforced polyester (CGRP) cruciform specimen subjected to a quasi-static tensile biaxial loading [99]. This is the first time this problem is accomplished for computing the stress intensity factors (SIFs) produced in the biaxially loaded area of the cruciform specimen. SIFs are calculated for infinite plates under biaxial loading as well as for the CGRP cruciform specimens in order to review the possible edge effects. A new ratio relating the side of the central zone of the cruciform and the crack length is proposed. Additionally, the initiation and evolution of a three-dimensional crack are successfully simulated. Specific challenges such as the 3D crack initiation, based on a principal stress criterion, and its front propagation, in perpendicular to the principal stress direction, are conveniently addressed. No initial crack location is pre-defined and an unique crack is developed.

A three-dimensional progressive damage model (PDM) is implemented within a CGRP cruciform structure for modelling its damage under loading [100]. In order to simulate the computational behaviour of the composite, the constitutive model considers an initial elastic behaviour followed by strain-softening. The initiation criterion defined is based on the maximum principal stress of the composite and once this criterion is satisfied, stiffness degradation starts. For the computation of damage, the influence of the fibre and the matrix are taken into account within the damage rule. This is the first time a three-dimensional PDM is implemented into a composite cruciform structure subjected to biaxial loading.

A new approach for dynamic analysis of stationary cracks using XFEM is

derived. This approach is capable of addressing dynamic and static fracture mechanics problems. Additionally, by means of this relatively simple approach, it is possible to address correctly the crack pattern of the 10° off-axis laminate manufactured solving the limitation observed with progressive damage modelling. During the whole thesis, the computational outcomes have been validated by means of comparison with theoretical and experimental results.

Acknowledgements

First and foremost, I would like to extend my appreciation to my supervisor, Dr.Curiel-Sosa. I will be forever grateful for giving me the opportunity of being part of this prestigious university. His vast knowledge and expertise in the field of computational modelling of composite has been an inspiration to me. I would also like to thank my secondary supervisor, Dr. Christophe Pinna, for always being helpful and friendly, whenever I have had any questions. Thanks to Dr. Serna Moreno for helping me during these years and enrich me with her experience. I would like to acknowledge my parents for their support during all my life and for the example that they are for me. Thanks to my siblings and cousins for helping me being a better person and sharing with me all their experiences that contributed to my personal development. Thank to my colleagues at work and friends from Sheffield for helping me during my 3 years in the UK and make home seems to be closer. Thanks to my friends from Spain for supporting me.

Contents

List of Figures

LIST OF FIGURES

LIST OF FIGURES

List of Tables

1

Introduction

1.1 Motivation

It is well known that the power of computers has been notably increased in the last decades. Considering this fact, a huge development in, for instance, computational mechanics (CM) is been a reality nowadays. CM is interdisciplinary because many concepts, methods and principles are applied in order to successfully simulate complex physical events such as, for instance, a car crash, a human aorta containing an aneurism, etc [103]. Great news that so many physical phenomena of interest are been reproduced by means of a computer. For example, stress analysis is an excellent tool for predicting the distribution of loads in the structure when the behaviour of the material is linear-elastic. Nonetheless, when modelling material failure, the computational tools available are not as robust as linear stress analysis. In the literature, different approaches deal with this problem but limitations exits generally e.g. divergence of the numerical technique before virtual failure. Hence, failure modelling of materials is still in ongoing research. In particular, for Advanced Composite Materials (ACM), computational modelling of fracture is being a challenging task. ACM are formed by two different materials: fibres (e.g. carbon or glass) and matrix (e.g. epoxy). The matrix is responsible for supporting and protecting the fibres and in the other hand, the fibres are the reinforcement of the matrix and provides the majority of the strength and stiffness in the material [151]. The amount of engineering applications using composite materials have been increased significantly in the last decades e.g. military and civil aircraft, automotive industry, etc [72]. This huge increment is attributed, mainly, to

the high strength-weight ratio that these materials provide, its excellent resistance to fatigue and corrosion as well as its satisfactory durability.

When modelling computational failure in ACM, different scales of interest may be chosen from microlevel to macrolevel passing though mesolevel (see Figure 1.1). The microscale is the level where fibres and matrix are considered individually while in the mesolevel the material is homogenized. In other hand, when there is a homogenization through the thickness the analysis is understood to be at the macrolevel. It is understandable that when considering the micromechanics effects, a computational solution closer to reality is expected. However, the computational cost may be unaffordable. Therefore, depending of the interest of the user, a scale or another is preferred. In this work, the attention is focused in the mesolevel and macrolevel. Depending of the type of composite under analysis, the material is defined with orthotropic or isotropic properties.

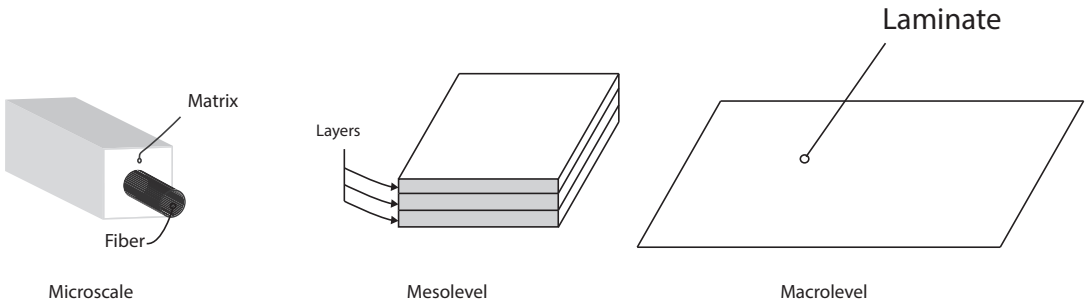

Figure 1.1: Three different approaches of study composite materials.

Computational simulation of failure for composite materials has been an area of interest for many years because experimental costs of these materials may be reduced by means of computer simulations. For instance, according to Cox and Yang [33], a typical airframe on which the human lives depends currently requires $\sim 10^4$ experimental tests of material specimens to reach safe certification. Taking the previous example into account, it is noticed how important is to obtain more reliable computational tools for these kind of materials in order to reduce experimental tests.

The motivation of this thesis is the computational simulation of cracks in structures subjected to multiaxial loading using XFEM and PDM. The structures under consideration in this thesis are form by two types of ACM: a chopped fibre glass reinforced

polyester (CGRP) and a carbon fibre reinforced polymer (CFRP). The CGRP presented in this work is used in internal coating and frontal parts of trains (see Figure 1.2 (a)). In the other hand, the CFRP laminate extensively used in the fuselage of aircraft such as, for instance, a Boeing 787 (see Figure 1.2 (b)).

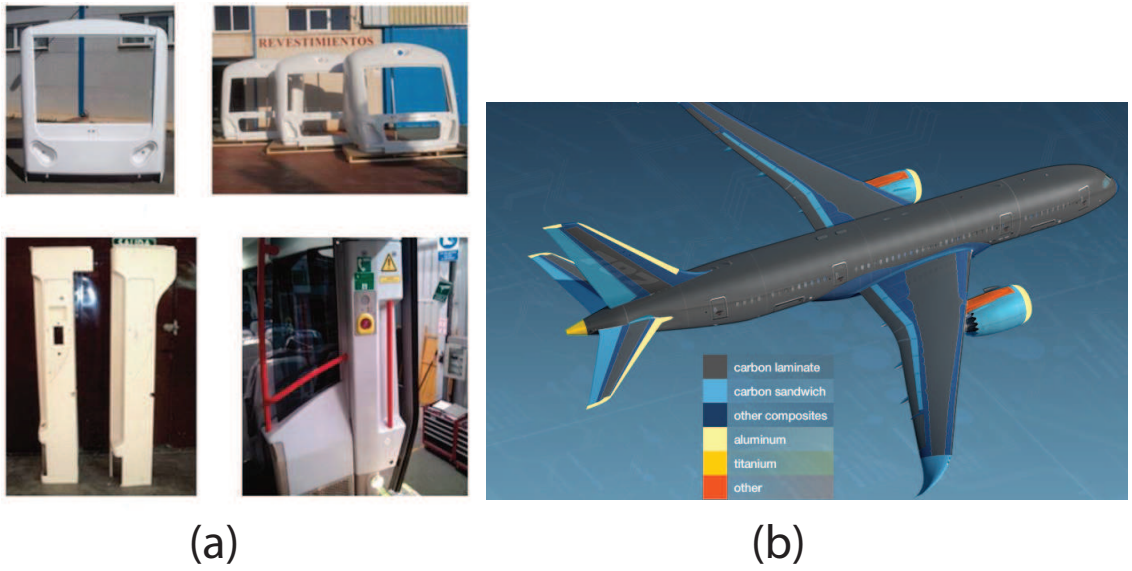

Figure 1.2: (a) The CGRP composite under analysis is used for internal coating and the frontal parts in trains. (b) The CFRP laminate is used in the fuselage of a Boeing 787 [1]

1.2 Advanced composite materials

The material under consideration in this research is a fibre-reinforced composite composed of fibres embedded in a matrix. In particular, two main types of composite are considered, the first type of composite is form by continuous fibres that provide the majority of the stiffness and strength and the matrix provides protection and support to the fibres (see an schematic representation in Figure 1.3 (b)). The second one is a composite form by short or chopped glass fibres (see an schematic representation in Figure 1.3 (a)). In this case, each lamina contains short fibres distributed randomly and several laminae are stacked into a laminate forming the desired structure. The load is mainly carried by the matrix and the fibres provide some stiffening.

The mechanical properties of the composite depends on the properties of the fibres and matrix and also about the orientation and amount of fibres. Considering a scale

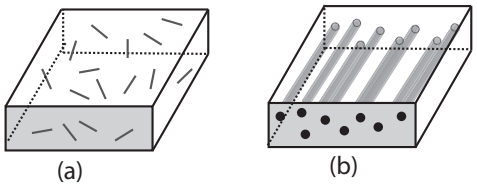

Figure 1.3: Schematic representation of a (a) chopped fibre composite and (b) a continuous fibre composite.

that is large compared to the fibre diameter, it can be assumed that the composite may be treated as homogeneous [74]. This implies that the properties are the same at every point. The orientation of the fibres determines the behaviour of the composite under loading. As mention previously, two type of composite are considered in this thesis. The first type considers continuous unidirectional fibres. In this type of composite, in order to define the elasticity properties, a local coordinate system $\{123\}$ (see Figure 1.4) is defined aligned with the fibre direction where direction 1 corresponds with the fibre orientation, direction 2 is the first in-plane transverse direction and direction 3 is the second out-of-plane direction. The modulus of elasticity for direction 1, E_1, is typically higher that those in the transverse direction (E_2 and E_3). When $E_1 \neq E_2 \neq E_3$, the material behaves as a orthotropic. It is common to assume that the plane transverse properties to the fibre direction are isotropic i.e. $E_2 = E_3$. Therefore, the material is so-called transversely isotropic. Thus, the transversally isotropic Hooke's law for a ply is defined as:

$$\bar{\sigma} = \bar{D}\bar{\epsilon} \tag{1.1}$$

where

$$[\bar{D}]^{-1} = \begin{bmatrix} \frac{1}{E_1} & \frac{-\nu_{21}}{E_2} & \frac{-\nu_{21}}{E_2} & 0 & 0 & 0 \\ \frac{-\nu_{21}}{E_2} & \frac{1}{E_2} & \frac{-\nu_{23}}{E_2} & 0 & 0 & 0 \\ \frac{-\nu_{21}}{E_2} & \frac{-\nu_{23}}{E_2} & \frac{1}{E_2} & 0 & 0 & 0 \\ 0 & 0 & 0 & \frac{1}{G_{23}} & 0 & 0 \\ 0 & 0 & 0 & 0 & \frac{1}{G_{12}} & 0 \\ 0 & 0 & 0 & 0 & 0 & \frac{1}{G_{12}} \end{bmatrix} \tag{1.2}$$

$\bar{\sigma}$ is the stress tensor with respect to the local coordinate system $\{123\}$, $\bar{\epsilon}$ is the strain tensor with respect to the local coordinate system $\{123\}$, ν_{12} and ν_{23} are the longitudinal and transverse Poisson ' s ratios, G_{12} is the longitudinal shear modulus

and G_{23} is the transverse shear modulus which for a transverse isotropic material is defined as;

$$G_{23} = \frac{E_2}{2(1+\nu_{23})} \tag{1.3}$$

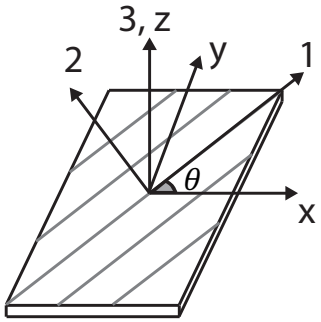

Figure 1.4: Local coordinate system defined in unidirectional (UD) layers.

The second type considers a glass reinforced composite with fibres oriented randomly. In this case, under linearly elastic conditions, the material is defined as linear elastic. For this kind of material the coordinate system is chosen arbitrary and in this case is defined respect to the local coordinate system {123}. The stress-strain relation is defined by means of two independent material constants E, ν ($E = E_1 = E_2 = E_3$ and $\nu = \nu_{23} = \nu_{13} = \nu_{12}$) as;

$$\bar{\sigma} = \bar{D}\bar{\epsilon} \tag{1.4}$$

with

$$[\bar{D}]^{-1} = \begin{bmatrix} \frac{1}{E} & \frac{-\nu}{E} & \frac{-\nu}{E} & 0 & 0 & 0 \\ \frac{-\nu}{E} & \frac{1}{E} & \frac{-\nu}{E} & 0 & 0 & 0 \\ \frac{-\nu}{E} & \frac{-\nu}{E} & \frac{1}{E} & 0 & 0 & 0 \\ 0 & 0 & 0 & \frac{1}{G} & 0 & 0 \\ 0 & 0 & 0 & 0 & \frac{1}{G} & 0 \\ 0 & 0 & 0 & 0 & 0 & \frac{1}{G} \end{bmatrix} \tag{1.5}$$

where E is the Young modulus and ν the Poisson's ratio.

It is important to notice that the previous stress and strain relations are defined in the local coordinate system {123}. For defining stress and strains in the finite element (FE) context, these vectors have to be defined in the global coordinate system $\{xyz\}$ (see Figure 1.4). Therefore, a rotation from the local coordinate system {123} to the global coordinate system $\{xyz\}$ has to be made. In order to transform the

global stress vector $\sigma = \{\sigma_x, \sigma_y, \sigma_z, \sigma_{yz}, \sigma_{zx}, \sigma_{xy},\}$ to the local coordinate system $\bar{\sigma} = \{\sigma_1, \sigma_2, \sigma_3, \tau_{23}, \tau_{31}, \tau_{12},\}$ the following transformation is considered;

$$\bar{\sigma} = T\sigma \tag{1.6}$$

with

$$T = \begin{bmatrix} cos^2\theta & sin^2\theta & 0 & 0 & 0 & 2sin\theta cos\theta \\ sin^2\theta & cos^2\theta & 0 & 0 & 0 & -2sin\theta cos\theta \\ 0 & 0 & 1 & 0 & 0 & 0 \\ 0 & 0 & 0 & cos\theta & -sin\theta & 0 \\ 0 & 0 & 0 & sin\theta & cos\theta & 0 \\ -sin\theta cos\theta & sin\theta cos\theta & 0 & 0 & 0 & cos^2\theta - sin^2\theta \end{bmatrix} \tag{1.7}$$

where θ is the angle between the x-axis and the 1-axis. The constitutive matrix respect to the global coordinate system is written as $D = T^{-1}\bar{D}T$. Tacking this relation into account, the constitutive relation is defined as $\sigma = D\epsilon$.

1.3 Computational failure of materials

In order to simulate cracks in a material, two main computational approaches can be distinguished: the continuum approach and the discontinuous approach. The continuum approach is based on continuum damage mechanics (CDM) where a crack is view as a band with finite width. In the other hand, the discontinuous approach permits the representation of a crack as a jump in the displacement field. This point of view is more realistic approach because a crack by definition is a discontinuity.
It has to be noticed that when using the FEM for the case of continuum approach a few changes in the formulation are necessary. However, using the discontinuous approach changes are necessary for adapting the FEM scheme to the discontinuous view e.g. introducing enrichment functions. In this Section, several continuous and discontinuous approaches are reviewed.

1.3.1 Continuum approach

1.3.1.1 Plasticity

The theory of plasticity concerns the mathematical study of stress and strain when a solid deforms plastically [26, 61]. During years, this approach mainly has been applied

to metals. Many materials under high load levels i.e. up to yield stress, exhibit non-linear behaviour and this non-linear tendency is usually connected with irreversible processes like plastic behaviour. The main assumptions considered in plasticity when modelling failure is shown in Figure 1.5. In this figure, the stress-strain curve in a uniaxial loading case for hardening plasticity is plotted. At low values of stress i.e. under yield yield stress, loading and unloading presents a elastic behaviour while for higher stress, unloading is still elastic while loading introduces a plastic strain ϵ^P.

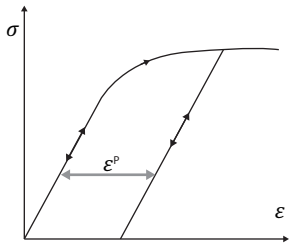

Figure 1.5: Hardening plasticity.

In order to build the finite element implementation of a plasticity mode, a return mapping algorithm [76, 130] is a common way forward.

1.3.1.2 Failure models based on stress quadratic functions

During years, failure models using quadratic stress functions have been used for prediction of failure in ACM [144][112][57]. The majority of theses models were derived from analytical solutions and afterwards implemented on finite element codes. The implementation of these failure models have been successfully applied for commercial finite element e.g. ANSYS (Tsai and Wu criterion [144]) and ABAQUS (Hoffman criterion [66]). It is important to mention that, important efforts have been carried out in order to find a criteria that may be applied for the majority of the problems. For instance, during the world-wide failure exercise (WWFE), a number of these criteria were described and tested with experimental results [63, 64, 65, 133]. For a computational point of view, a finite element that satisfies the stress condition is removed from the discretization. This removal can cause numerical oscillations and as a consequence, the possible divergence of the numerical technique.

It is important to underline that the prediction of the initiation of the failure process is

not enough because the local failure does not imply that the whole structure will fail. For example, in a laminate, once a ply fail the stresses may be redistributed along the structure and consequently the laminate may carry more load.

1.3.1.3 Progressive damage modelling

Progressive damage modelling is based in continuous damage mechanics [26][79]. This discipline considers progressive material strength degradation before one main macroscopic crack appears (final state). For instance, as Kachanov [73] initially proposed for a one-dimensional case, the previous idea is related by means of a damage variable D using the effective stress concept [26]. On a macroscopic scale, the damage variable D takes into account the microscopic deteriorations (voids, microcracks, etc). For instance, modelling isotropic damage processes it suffices to consider a scalar damage variable whereas modelling anisotropic damage a second or fourth order tensor is required [129]. Thus, for example, the constitutive law for isotropic degradation can be written as;

$$\sigma = (1 - \omega) D \epsilon \tag{1.8}$$

The value of ω is ranged between 0 and 1, thus, the value of the damage variable is zero in the case of unstressed material and one when the macroscopic crack is initiated. Several progressive damage for composite materials has been proposed during the last decades e.g. Matzenmiller [85], Lapczyk [77], Edlund [44], Maimí [81], [82],[83].

Mesh-dependency exist when using continuum damage models for failure. Particularly, during strain-softening and strain location i.e. where deformation trends to concentrate in the structure, the results present a strong mesh dependency in the finite element solution where the energy dissipated decreases upon mesh refinement. This behaviour can be relieved using the crack band model proposed by Bazănt and Oh [12]. In this method, local stress-strain behaviour depends of the element size. However, this method does not completely solve the mesh dependency because, for instance, element form and orientation still provoked changes in the solution. Some authors have solved this mesh dependency problem by regularisation techniques [40]. Another possibility is to use nonlocal damage models where the damage variables depend on the strain state of the neighbourhood giving a characteristic length. Additionally, some applications of progressive failure analysis applied to bolted joints or pin-loaded laminates are provided in [23, 24, 28, 113, 118, 145, 157]

1.3.2 Discontinuous approach

1.3.2.1 eXtended Finite Element method

A limitation is observed when using FEM for simulating moving cracks throughout a structure. To accurate represent discontinuities with FEM, it becomes necessary to conform the discretisation to the discontinuity. Then, in the case of crack propagation, the mesh is re-generated at each crack-growth increment with a considerable computational cost. Over the last decades several approaches for modelling material discontinuities have been proposed based on the partition of unity concept [11, 52, 88], as the Generalized Finite Element Method (GFEM) [49] or the XFEM [14] developed by Belytschko and Black in 1999 and improved by Moes et al. [96]. In particular, XFEM has been a robust numerical technique for modelling fracture.

General problem

A two-dimensional dynamic problem is considered where a body Ω with boundary $\partial\Omega$ is defined. This boundary is divided into $\partial\Omega_u$, $\partial\Omega_F$ and Γ_c (see Figure 1.6). Hence, $\partial\Omega = \partial\Omega_u \cup \partial\Omega_F \cup \Gamma_c$, where $\partial\Omega_u$ represents the prescribed displacements in the body Ω, $\partial\Omega_F$ is the part of the body subjected to surface forces and Γ_c corresponds to the displacement discontinuity e.g. a crack. Note that the crack 's faces are traction free. The motion of the body is defined by the displacement $u(x,t)$, which is a function of the location of the material point x and the time t. The material is linear elastic isotropic and its mass density is ρ. The body presents applied displacements $\bar{u}$ on the Dirichlet boundary $\partial\Omega_u$ and applied traction $\bar{t}$ on the Neumann boundary $\partial\Omega_F$; $\partial\Omega_u \cap \partial\Omega_F = \emptyset$, $\partial\Omega_u \cap \Gamma_c = \emptyset$, $\partial\Omega_F \cap \Gamma_c = \emptyset$. The outward normal vector in the material boundary is defined as $n^{\perp}$ and b is the body force per unit mass. Thus, the strong form of the problem is written as follows:

$$\nabla\sigma + \rho b - \rho\ddot{u} = 0 \; in \; \Omega \tag{1.9}$$

subjected to the boundary conditions:

$$u = \bar{u} \; on \; \partial\Omega_u \tag{1.10}$$

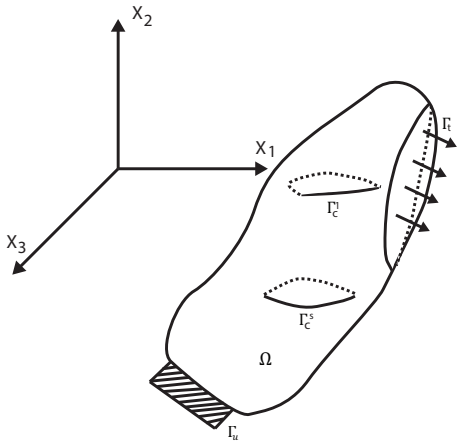

Figure 1.6: A two dimensional body cracked and its boundaries.

$$\sigma n = \bar{t} \; on \; \partial\Omega_F \tag{1.11}$$

$$\sigma n = 0 \; on \; \Gamma_c \tag{1.12}$$

The constitutive relation of the material is written:

$$\sigma(x,t) = C\epsilon(u(x,t)) \tag{1.13}$$

where σ is the Cauchy stress tensor, C the constitutive matrix and ϵ the strain tensor.

Space discretisation

The displacement at a generic point x, $u(x,t)$ is approximated by u^h using continuous and discontinuous terms as follows [95]:

$$u^h(x,t) = u^{cont}(x,t) + u^{cut}(x,t) + u^{tip}(x,t) \tag{1.14}$$

where u^{cont} corresponds to the continuous approximation of the displacement, u^{cut} corresponds to the discontinuous approximation for addressing the crack and u^{tip} denotes the discontinuous approximation corresponding to the crack tip. The continuous part of u^h is approximated by the standard shape functions $N_I(x)$ as follows:

$$u^{cont}(x,t) = \sum_{I \in n^{std}} N_I(x) u_I(t) \tag{1.15}$$

Here, n^{std} is the total number of nodes into the mesh and u_I are the displacement nodal values. The enrichment strategy adopted is illustrated in Figure 1.7. In this Figure, the nodes enriched by the Heaviside functions are marked with circles and the nodes enriched with the crack tips functions are marked by squares.

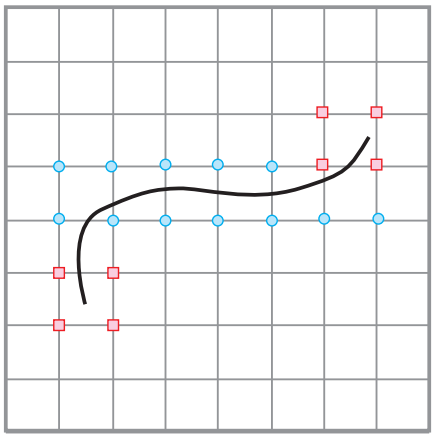

Figure 1.7: Definition of the nodes n^{cut} cut by the crack (circles) and n^{tip} enriched with the crack tip enrichment function (squares).

The discontinuity across the crack is included by the second term of Eq.(1.14) defined as:

$$u^{cut}(x,t) = \sum_{I \in n^{cut}} N_I(x) H(x) a_I(t) \tag{1.16}$$

where a_I are the enriched degrees of freedom and $H(x)$ is the Heaviside function defined as:

$$H(x) = \begin{cases} 1 & \text{if} \quad x \geq 0 \\ \\ -1 & \text{if} \quad x < 0 \end{cases} \tag{1.17}$$

n^{cut} are the nodes corresponding to the crack body (see Figure 1.7). The third displacement contribution in Eq. 1.14, $u^{tip}(x,t)$, corresponds with the displacement field on the crack tip,

$$u^{tip}(x,t) = \sum_{I \in n^{tip}} N_I(x) \Phi(x) b_I(t) \tag{1.18}$$

where b_I are the degree of freedom associated with the crack tip enrichment and n^{tip} is the set of nodes of an element that contains the crack tip. The elements that contain the crack tip are enriched with a function that represents the asymptotic displacement field ahead of the crack tip. This function is responsible for introducing more physics in the solution and also localising the crack throughout an element. As Elguedj et al. [45] points out, the localisation of the crack inside the element is addressed by the function,

$$\Psi(x) = \sqrt{r} sin\left(\frac{\theta}{2}\right) \tag{1.19}$$

where r and θ define the local polar crack tip coordinate system ahead of the crack tip. This function is responsible for the strong discontinuity inside the crack. Note that another set of functions can be used to address the asymptotic displacement field ahead of the crack tip such as [46]:

$$\Psi(x) = \sqrt{r}\left[sin\left(\frac{\theta}{2}\right), cos\left(\frac{\theta}{2}\right), sin\left(\theta\right) sin\left(\frac{\theta}{2}\right), sin\left(\theta\right) cos\left(\frac{\theta}{2}\right)\right] \tag{1.20}$$

In this approach, the standard singular crack tip field for linear elasticity (Eq.(1.19)) is chosen for its simplicity and because it is capable of addressing the strong discontinuity inside the crack. Finally, taking into account all displacement terms, the displacement approximation is expressed as follows:

$$u^h(x) = \sum_{I \in n^{std}} N_I(x) u_I + \sum_{I \in n^{cut}} N_I(x) H(x) a_I + \sum_{I \in N^{tip}} N_I(x) \Psi(x) b_I \tag{1.21}$$

Considering the displacement field (Eq.(1.21)) into the weak form of the momentum equation, the discretised motion equation (see Belytschko et al. [16] for a more detailed description) can be defined as,

$$M_{IJ} \ddot{u}_j^h = f_I^{ext} - f_I^{int} \tag{1.22}$$

where M_{IJ} is the mass matrix for all DOF, $\ddot{u}_j^h$ represents the acceleration, f_I^{ext} and f_I^{int} are external and internal nodal forces respectively. Therefore, the internal forces are defined as:

$$f_I^{int} = \begin{bmatrix} f_I^{u,int} \\ f_I^{a,int} \\ f_I^{b,int} \end{bmatrix} \tag{1.23}$$

The strain is expressed based on the strain-displacement relation:

$$\epsilon(u(x)) = B_I^u u_I + B_I^a a_I + B_I^b b_I \tag{1.24}$$

where

$$B_I^u = \begin{bmatrix} N_{I,x} & 0 \\ 0 & N_{I,y} \\ N_{I,y} & N_{I,x} \end{bmatrix} \tag{1.25}$$

$$B_I^a = \begin{bmatrix} (N_I H)_{,x} & 0 \\ 0 & (N_I H)_{,y} \\ (N_I H)_{,y} & (N_I H)_{,x} \end{bmatrix} \tag{1.26}$$

$$B_{Ij}^b = \begin{bmatrix} (N_I \Phi_j)_{,x} & 0 \\ 0 & (N_I \Phi_j)_{,y} \\ (N_I \Phi_j)_{,y} & (N_I \Phi_j)_{,x} \end{bmatrix} \tag{1.27}$$

New developments in analysis of crack growth modelling are carried out since XFEM came up [2], for instance the implementation of XFEM in 3D [139], the delamination of GLARE [37], frictional contact [42], growth of arbitrary cohesive cracks [94], mesoescale modeling of dislocations in two dimensions [18] and three dimensions [51], etc. For interested readers, a detail understanding of XFEM is presented in the work of Mohammadi [135] and in the reviews of Rabczuk et al.[114] and Belytschko et al. [19].

1.3.2.2 Interface modelling

The interface elements allows the discontinuity to be between the elements. In order to illustrate the formulation of this approach, a simple two-dimensional example is considered where the interface is a line element as depicted in Figure 1.8. Node 3 and 4 are on the top side while 1 and 2 are the bottom side of the interface. Thus, considering two degrees of freedom per node, u and v, the nodal displacements of the top are

$p_{top}^T = (u_3 \quad v_3 \quad u_4 \quad v_4)$ and in the bottom $p_{bot}^T = (u_1 \quad v_1 \quad u_2 \quad v_2)$. The displacement field for the top element is $u_{top} = Np_{top}$ and for the bottom element $u_{bot} = Np_{bot}$ where N are the shape functions. Then, the relative displacement is defined as the different of displacement between the top and bottom surfaces $u = u_{top} - u_{bot}$.

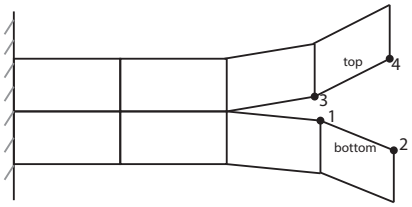

Figure 1.8: Schematic representation of the interface element in a two-dimensional example.

A wide range of examples has shown that interface modelling is a very effective way of modelling discrete failures that are important in fracture of polymer matrix composites [155]. For instance, interface modelling has been applied for delamination [3, 31, 34, 124] and impact in composites [53, 71].

1.3.2.3 Phantom node method

Initially proposed by Hansbo and Hansbo [55]. The method was afterwards related with XFEM using the approach of Hansbo [138] for dynamic crack and shear band propagation. The main advantage of phantom node method is that that its implementation is relatively easy because any changes to the adjacent element are necessary. In this method crack are treated adding phantom nodes and superposing elements on the original mesh. This idea is represented in Figure 1.9. In this figure, it is presented the decomposition of the cracked element into two elements where solid circles are original nodes and hollow circles phantom nodes.

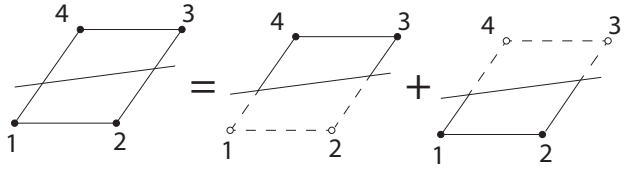

Figure 1.9: Decomposition of a cracked element. Solid circles denoted original nodes and hollow circles denote phantom nodes.

The phanton node method has been considered in 2D [91, 115], 3D [43, 90] and thin shells based on Kirchhoff theory [9, 136, 137]

1.3.3 Phase field methods

Phase-field modelling of brittle fracture has been a topic of interest during the last years [4, 5, 21, 92, 93]. This approach is very attractive because is capable of simulating complicated fracture scenarios such as crack initiation, propagation, merging and branching for general situations without the need of ad-hoc criteria. The crack propagation is tracked automatically by the evolution of the smooth crack field. Accoding to [47], the quasi-static process of crack initiation, propagation and branching is governed by the minimization problem of the free energy functional:

$$E(u,\Gamma) = \int_{\Omega} \Psi_e(\epsilon(u))dx + G_c \int_{\Gamma} ds \tag{1.28}$$

where Ψ_e is the elastic energy density function, ϵ the strain tensor and G_c the material fracture toughness. The solution is valid when $\Gamma \subset \Omega$ and a displacement field $u : \Omega \to \mathbb{R}$ which is discontinuous along Ψ. According to [47], the problems of the classical Griffith theory for brittle fracture are overcome using the formulation presented in Equation 1.28. In order to provide an efficient numerical implementation of Equation 1.28, its regularized formulation was proposed by Bourdin et al. [22]. However, the proposed formulation of Bourin et al. does not make a difference between fracture due to tension or compression. To avoid this fact, a modified regularized formulation was proposed by [6]. Recently, in order to improve the efficiency of phase-field methods, higher-order and hybrid formulations has been proposed [21].

1.4 Biaxial loading analysis

In some cases, for validating material models, an uniaxial loading test is considered. Normally, composite structural components are subjected to general loading scenarios which allow them to developed general stress scenarios. Hence, the real applications require a detailed knowledge of the biaxial if not triaxial state of stresses. Therefore, a better understanding of the response of composite structures to multiaxial loading is desired [62]. In this work, the attention is focused in the study of the behaviour of composites subjected to pure biaxial stress states. There are several ways of reproducing

measurable biaxial stress states [131]. In particular, two principal approaches to deal with biaxial loading in composite materials are well known in the scientific community: the first one using tubular specimens e.g [54, 132] and the second one by means of cruciform specimens where the loads are applied in-plane and perpendicular directions e.g [41, 78, 84, 148, 152, 158]. In the current thesis the attention is focused in cruciform specimens subjected to in-plane tensile loading as well as specimens subjected to tensile loading in one direction.

1.5 A discussion of the current state of art

In this chapter, three main approaches have been considered for the simulation of cracks i.e. continuum approach, discontinuous approach and phase field methods. In the case of continuous approaches, some limitations are observed. For instance, in failure models based on stress quadratic functions, the prediction of the initiation of the fracture process is not enough because local failure does not imply that the considered structure fails. In fact, in a laminate, once a ply fail the stresses can be distributed thought the structure and then, the structure can carry more load. In general, in continuous models such as plasticity and progressive damage modelling, the constitutive equations present a strong softening behaviour as the damage level rises, which induce strain and damage localization. This fact allows the loss of ellipticity of the differential equations and a strong mesh dependency of the results. For solving this issue, a material length scale through non-local or gradient damage approaches has been proposed [13, 109]. Continuous approaches are typically unable to describe the surface decohesion [5]. In additiona, when damage localizes into a macroscopic crack, the continuum models are known to exhibit stress locking (spurious stress transfer) and possible instability (spurious kinematic modes)[70]

On the other hand, discontinuous approaches presents some limitations. In the case of XFEM, in order to simulate cracks, a tracking of the discontinuity is needed, the integration is not straight and a remeshing may be required for curve cracks [87]. Additionally, using discontinuous models based on a cohesive crack model, it is not possible to address the first phase of densely distributed microcracks in the fracture process zone [123].

Recently, there have been some attempts to combine continuous and discontinuous approaches to address localization, crack initiation and propagation [123].

1.6 Thesis outline

The thesis presented is subdivided in six different chapters. In the current chapter, the main concepts of the research work and the literature review are provided.
In Chapter 2, the numerical and experimental analysis of a 10° off-axis laminate are carried out. Considering this laminate, it is pointed out a limitation of progressive damage modelling in correctly address the crack pattern of the laminate under analysis. This example serves to underline that the current state of the art, when dealing with fracture and damage in ACM, is still in ongoing development.

In Chapter 3, the attention is focused in numerical tools for the simulation of a complex loading scenario such as the biaxial loading. Therefore, two new outcomes using the eXtended Finite Element Method (XFEM) are presented, firstly, the 2D crack initiation and propagation of a crack on a chopped glass reinforced polyester (CGRP) composite are simulated by means of XFEM. Secondly, a 3D cruciform structure subjected to different biaxial in-plane loading scenarios is analysed numerically considering XFEM. This is the first time this problem is accomplished for computing the stress intensity factors (SIFs) produced in the biaxially loaded area of the cruciform specimen. A new ratio relating the side of the central zone of the cruciform and the crack length is proposed. It is important to underline that no initial crack location is pre-defined, then, as a natural outcome the 3D crack is initiated and propagated. The numerical results are afterwards validated with experimental tests.

In Chapter 4, a 3D PDM is implemented within a CGRP cruciform structure for modelling its damage under loading. The structure is subjected to a biaxial loading and its damage is addressed. The cruciform is form by chopped fibres and the material is assumed to be computationally isotropic. However, for the computation of damage, a new relation is considered taking into account the influence of the fibre and the matrix within the damage rule. The computational outcomes are then validated with experimental tests.

In Chapter 5, a new dynamic approach for simulating stationary crack using XFEM is proposed. The objective of this chapter is to propose a solution for the limitation

found in chapter 2 with PDM. In order to validate the proposed approach, several numerical examples are simulated and compared with the theoretical solution and experimental outcomes.

In Chapter 6, the main conclusions of the work are underlined as well as the new developments proposed in this thesis.

1.7 Conclusions

In this chapter, an overview of the computational strategies for modelling cracks in ACM has been presented. Hence, for the simulation of cracks in a material, two main approaches have been distinguished: the continuum approach and the discontinuous approach. Although, there are several approaches for simulating fracture and damage in these high performance materials (each one with its advantages and disadvantages), the conclusion extracted from this chapter is that there is not a computational approach good enough to predict the complete mixed damage mode behaviour that appears in ACM.

2

Computational and experimental analysis of a 10° off-axis laminate

2.1 Introduction

In this chapter, a computational limitation encountered in the modelling of damage when dealing with ACM is discussed. The objective of this analysis is to underline that the current state of the art in the simulation of fracture in ACM is still in ongoing development and this outcome serves as a motivation during the work carried out in this thesis.

Chapter 2 is sub-divided into three main parts. Firstly, the design (Section 2.2.1) and linear elastic FE analysis (Section 2.2.2) of a 10° off-axis laminate is carried out. Two different end-tab designs are considered in order to compare the influence of the end-tab design in the strain field of the specimen. Secondly, in Section 2.2.3, an experimental tensile analysis using a non-interferometric technique called Digital Image Correlation (DIC) is carried out. Using this procedure, the full-field maps of strains while loading is addressed. Thus, the influence of the end-tab design will be observed from an experimental point of view validating the results obtained by means of simulations. Finally, a progressive damage model (PMD) is challenged to predict the crack pattern observed during experiments.

In this chapter, the manufacture of the specimens has been carried out by the University of Castilla La Mancha (Spain). On the other hand, the author of the thesis

is responsible for the design of the specimens, the linear and non-linear computational simulations and the experimental tensile testing using Digital image Correlation.

2.2 The 10° off-axis tensile test

In order to determine the shear strength of composite materials, several test methods have been developed [69] [27] [142]. In this chapter, the attention is focused on the 10° off-axis tensile test proposed by Chamis and Sinclair [27]. Considering this approach, a uniaxial tension is applied to a unidirectional composite, such as the fibres, to form an angle of ten degrees with the loading direction. The advantages of rectangular off-axis specimens are notable: those specimens are easy to manufacture and the testing process is relatively simple. To obtain the material constants using this test, a uniform state of stresses is required along the specimen. However, it has been demonstrated [106] that when the ends of the specimen are clamped using a straight end-tab, the application of constant end displacement induces shearing forces and bending moments in the specimen. Consequently, perturbations in the stress and strain field are observed. In order to overcome this limitation, Sun and Chung [140] proposed the use of an oblique-shaped end-tab design that resulted in a better estimation of the shear modulus and a more homogeneous stress distribution throughout the specimen. Several authors have been dealing with this test in experiments (using distributed strain gauges throughout the specimen) and by means of FEA [102, 111, 140, 149, 150, 156]. In this Chapter, the laminate is analysed computationally using linear/non-linear FE simulations and experimentally using DIC.

2.2.1 Material and geometries

The major dimensions of the rectangular specimens are 200 x 10 mm. The specimens were fabricated from commercially available (Hexcel Corporation) carbon/epoxy pre-impregnated tapes of 0.25 mm thick having a total thickness of 1.5 mm. Six specimens were cut for a 200 x 200 mm panel of carbon/epoxy IMA/M21. Six-ply unidirectional (UD) were stacked at ten degrees forming a $[10°]_6$ laminate. Additionally, two different end-tab designs are considered with 1 mm thickness, a traditional straight end-tab (see Figure 2.1) and an oblique end-tab (see Figure 2.2). The proposed specimen and loading condition may be observed in the fuselage of a commercial aircraft such as the

	Specimen	$A[m^2]$
Straigh glass/epoxy tabs	1	$1.59 \cdot 10^{-5}$
	2	$1.75 \cdot 10^{-5}$
	3	$1.42 \cdot 10^{-5}$
Oblique glass/epoxy tabs	4	$1.42 \cdot 10^{-5}$
	5	$1.46 \cdot 10^{-5}$
	6	$1.45 \cdot 10^{-5}$

Table 2.1: Measured values of cross section A for 6 different specimens.

Boeing 787 (see Figure 2.1).

The theoretical cross section A for the specimens presented in Figure 2.1 and 2.2 is $A = 1.5 \cdot 10^{-5} m^2$. However, due to the manufacturing process a different value is obtained for each specimen considered. The values of the cross section for each specimen are presented in Table 2.1. In that table, A is obtained as the average area for three different sections along each specimen.

The material properties in the principal directions are presented on Table 2.2 and its fibre volume fraction V_{fibre} is 59.2 % . Following the work carried out by [111], the end-tabs are formed by a ± 45 glass/epoxy laminate. The off-axis composite specimen under analysis is subjected to a uniaxial loading stress and different end-tab designs are considered: a straight and an oblique design.

The angle of the straight design in respect to the horizontal is 90 degrees. However, the angle of the oblique end-tab ϕ in respect to the x-axis is obtained using the following equation proposed by Sun and Chung [140]:

$$cot\phi = -\frac{C_{16}}{C_{11}} \tag{2.1}$$

Here C_{11} and C_{16} are the elements of the compliance matrix with respect to the global coordinate system {x,y}. Therefore, the strain in x-direction ϵ_{xx} is defined as $\epsilon_{xx} = C_{11}\sigma_{xx}$ and the shear strain is defined as $\gamma_{xy} = C_{16}\sigma_{xx}$. The load applied in x-direction σ_{xx} is the only non zero component of the stress tensor, σ. Tacking that

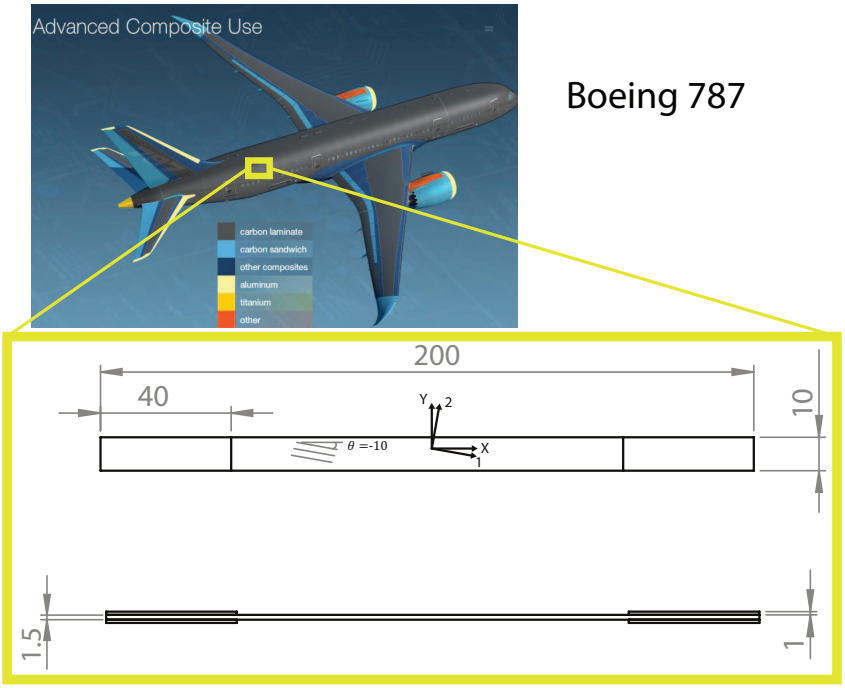

Figure 2.1: The image of the Boeing 787 has been extracted from www.boeing.com. Below this image the dimensions of the specimen with straight end-tab are presented. All dimensions in millimeters.

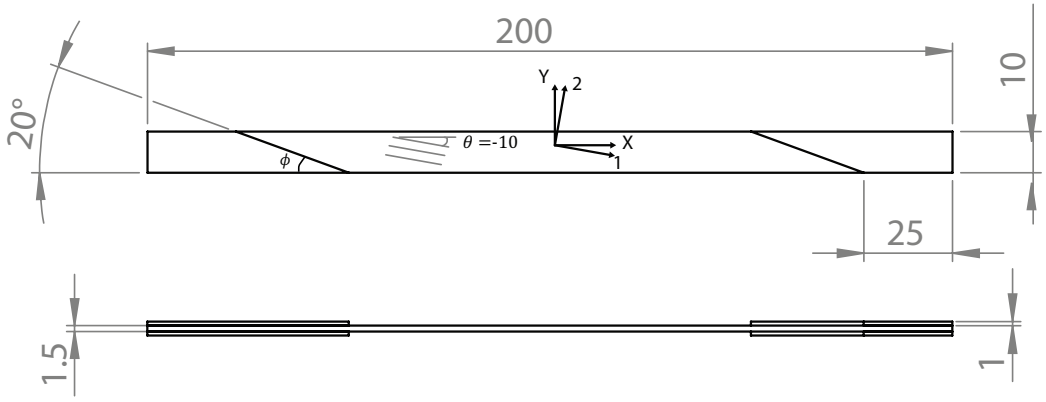

Figure 2.2: Dimensions of the specimen with oblique end-tab. All dimensions in millimeters.

into account, the strain-stress relation in respect to the global coordinate system is written as:

$$\epsilon = T^T \bar{C} T \sigma \tag{2.2}$$

Where ϵ is the strain tensor in respect to the {x,y} coordinate system, T is the coordinate transformation matrix and $\bar{C}$ is the compliance matrix in respect to the local coordinate system {1,2}. Considering the material properties of the CFRP provided on Table 2.2, the angle of the oblique end-tab ϕ following Eq.(2.1) is calculated as $\phi = 20°$ in respect to the x-axis.

Elasticity	Ply strength
E_1 174.4 GPa	X_t 2600 MPa
E_2 11.84 GPa	X_c 1500 MPa
ν_{12} 0.39	Y_t 56 MPa
G_{12} 5.15 GPa	Y_c 56 MPa
G_{13} 5.15 GPa	S_L 89.6 MPa
G_{23} 3.1 GPa	

Table 2.2: Material parameters in the principal directions.

2.2.2 Linear FE analysis of the 10° laminate

In this subsection, a numerical analysis using the FE code ABAQUS is carried out. The purpose of this analysis is to address the linear elastic behaviour of the $[10°]_6$ laminate. A 2D finite element model for the simulation of the off-axis specimens with oblique (see Figure 2.2) and straight end-tab (see Figure 2.1) is developed. From the ABAQUS FE library, a shell element S4R is chosen. Those elements are normally used to model structures in which one dimension is significantly smaller than the other two [59]. The elements have displacement and rotational DOF, therefore each node has six DOF. Linear approximation of displacements and reduced integration are considered. In order to avoid zero-energy modes of deformation due to the single integration point, hourglassing control is considered. As depicted in Figure 2.3, a mesh convergence analysis has been carried out considering three different meshes. In this Figure, the convergence analysis for the oblique specimen is presented. The chosen mesh for both specimens has 2400 elements.

The boundary and loading conditions considered for both specimens are presented in Figure 2.4. The boundary conditions are intended to address the rigid gripping

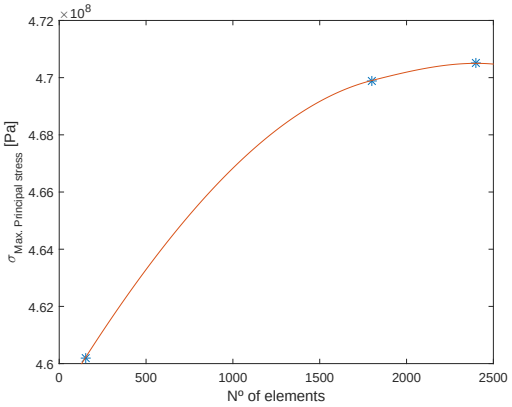

Figure 2.3: Mesh sensitivity analysis of the oblique end-tab design.

arrangement corresponding with the experimental testing. On the nodes of the left edge, the displacements and rotations are constrained to zero and in the right edge the only free DOF is the horizontal displacement u_x where the rest are constrained. The specimens considered for the analysis are the specimens number 3 and 4 since they have the same average cross section (see Table 2.1). For both specimens, the load is applied incrementally by means of a prescribed displacement until the force applied in the right edge reached 4.5 KN. Hence, since both specimens have the same cross section, the same stress is applied in the x-direction i.e. $\sigma_{xx} = 316.9MPa$. In order to achieve this value of force, the horizontal displacement applied in the oblique end-tab was 0.43 mm and for the specimen with the straight end-tab was 0.39 mm. These displacements are different because the specimen with the oblique end-tab is slightly longer than the specimen with the straight end-tab. In this case, the specimen with straight end-tab is 120 mm long and the specimen with oblique end-tab has a length of 122.52 mm.

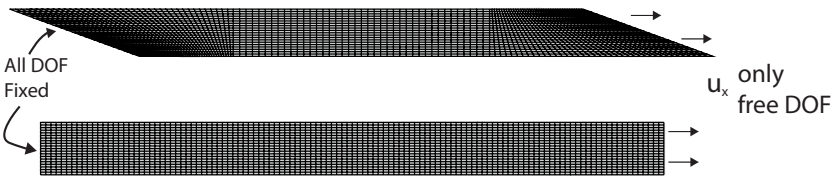

Figure 2.4: Boundary conditions and discretisation for both specimens. The meshes plotted have 2400 elements.

Plane stress conditions are assumed i.e. $\sigma_{33} = \sigma_{23} = \sigma_{13} = 0$, hence, the strain-

stress relation respect to the local coordinate system {123} is defined as;

$$\begin{bmatrix} \epsilon_{11} \\ \epsilon_{22} \\ \epsilon_{12} \end{bmatrix} = \begin{bmatrix} \frac{1}{E_1} & \frac{-\nu_{12}}{E_1} & 0 \\ \frac{-\nu_{21}}{E_1} & \frac{1}{E_2} & 0 \\ 0 & 0 & \frac{1}{G_{12}} \end{bmatrix} \begin{bmatrix} \sigma_{11} \\ \sigma_{22} \\ \sigma_{12} \end{bmatrix} \tag{2.3}$$

Notice that the engineering strain ϵ_{12} is considered in the strain tensor. An implicit solver (Newton method) for solving the static problem is considered.

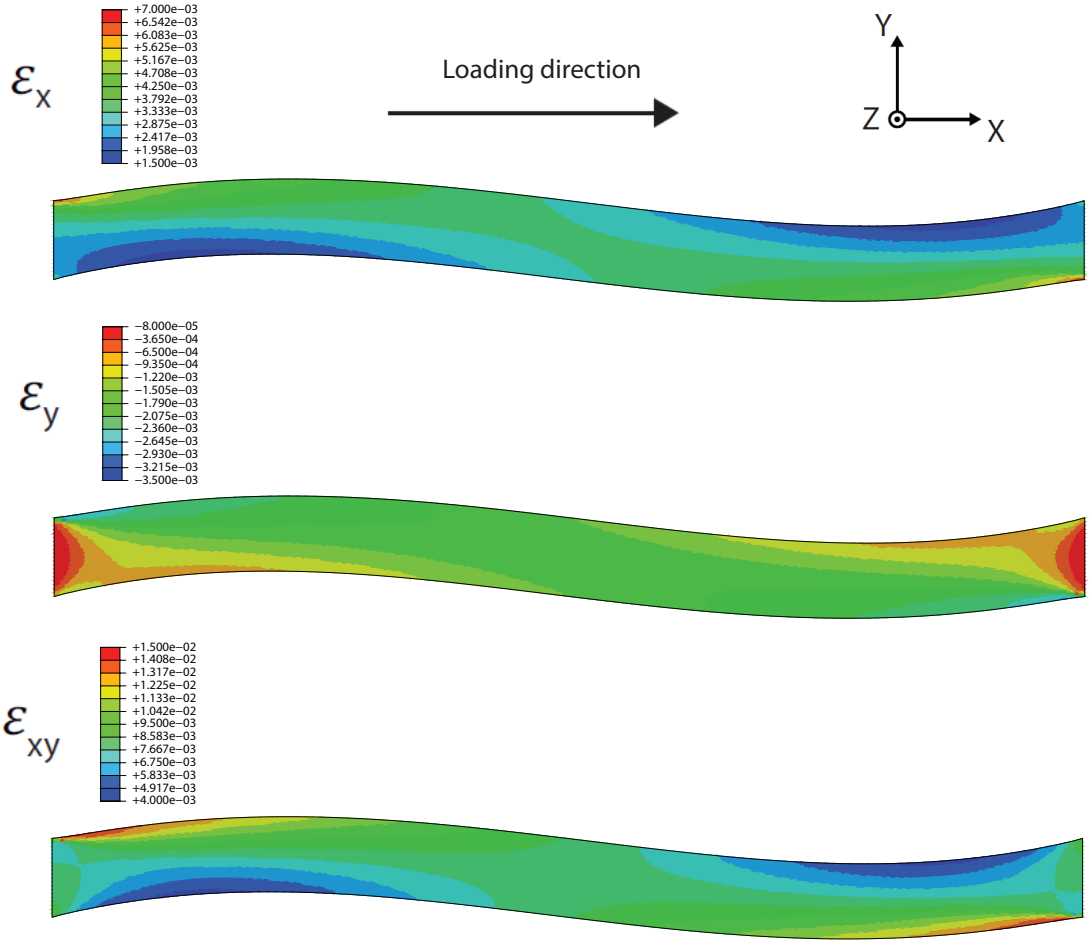

Figure 2.5: Computational maps of global strain for the 10° off-axis laminate with straigh end-tab design at 4.5 KN. It is considered a deformation factor of x30.

In Figure 2.5, the global maps of strains i.e. $\epsilon_x, \epsilon_y, \epsilon_{xy}$, for the specimen with straight end-tab are presented. These maps correspond with a tensile loading of 4.5 KN in x-direction. It is observed that the maps of strains are not homogeneous throughout

the specimen. In particular, the strain in x-direction ϵ_x (positive defined because the specimen is loaded in x-direction) is ranged between $6.54 \cdot 10^{-3}$ and $1.75 \cdot 10^{-3}$. Contrary to the specimen with the straight end-tabs, the specimen with oblique end-tab (see Figure 2.6) presents a homogeneous state of strain in x-direction and its value is $3.7 \cdot 10^{-3}$ throughout the specimen. In the same manner, the strain in y-direction (negative defined because of the Poisson effect) for the specimen with straight end-tabs is not homogeneous and its maximum and minimum values are $-8.84 \cdot 10^{-5}$ and $-3.03 \cdot 10^{-3}$ respectively. On the other hand, the strain in y-direction for the specimen with oblique end-tab remains constant in the specimen and its value is $-1.36 \cdot 10^{-3}$. Finally, for the case of shear strain ϵ_{xy}, the straight specimen has a heterogeneous strain field contrary to the specimen with oblique end-tab which has a homogeneous strain field and its value is constant in the whole specimen and equal to $1.1 \cdot 10^{-2}$.

It is important to notice that the straight end-tabs induce significant shear forces and bending couples, which leads to the characteristic 'S-shape' observed in Figure 2.5. On the other hand, the specimen with oblique end-tab presents a homogeneous state of stresses and lower values of strain (when applying 4.5 KN) compared with the straight end-tab specimen. In order to magnify deformation for both specimens, a deformation scale factor of 30 is considered.

In conclusion, based on the results from simulations, higher values of strain are observed in the specimen with straight end-tab than in the specimen with oblique end-tab for a fixed load of 4.5 KN. Hence, the specimen with straight end-tab will be able to carry less load than the specimen with oblique end-tab since the material is the same for both specimens. This fact is corroborated in Section 2.2.3 by experimental testing.

2.2.3 Experimental testing

In order to validate the computational results obtained for the two different end-tab designs, experimental tensile tests were carried out. The tests were done using a Tinius Olsen 25 KN tensile machine with self-tightening grips. The specimen was loaded at 2 mm per minute in order to apply the load slow enough to be considered as a quasi-static loading. Force over time was recorded during the test. The values of applied ultimate stress for the six specimens tested are presented in Table 2.3 and its values are defined as $\sigma_x^u = \frac{F^u}{A}$, where F^u is the ultimate applied force and A is the average area for three

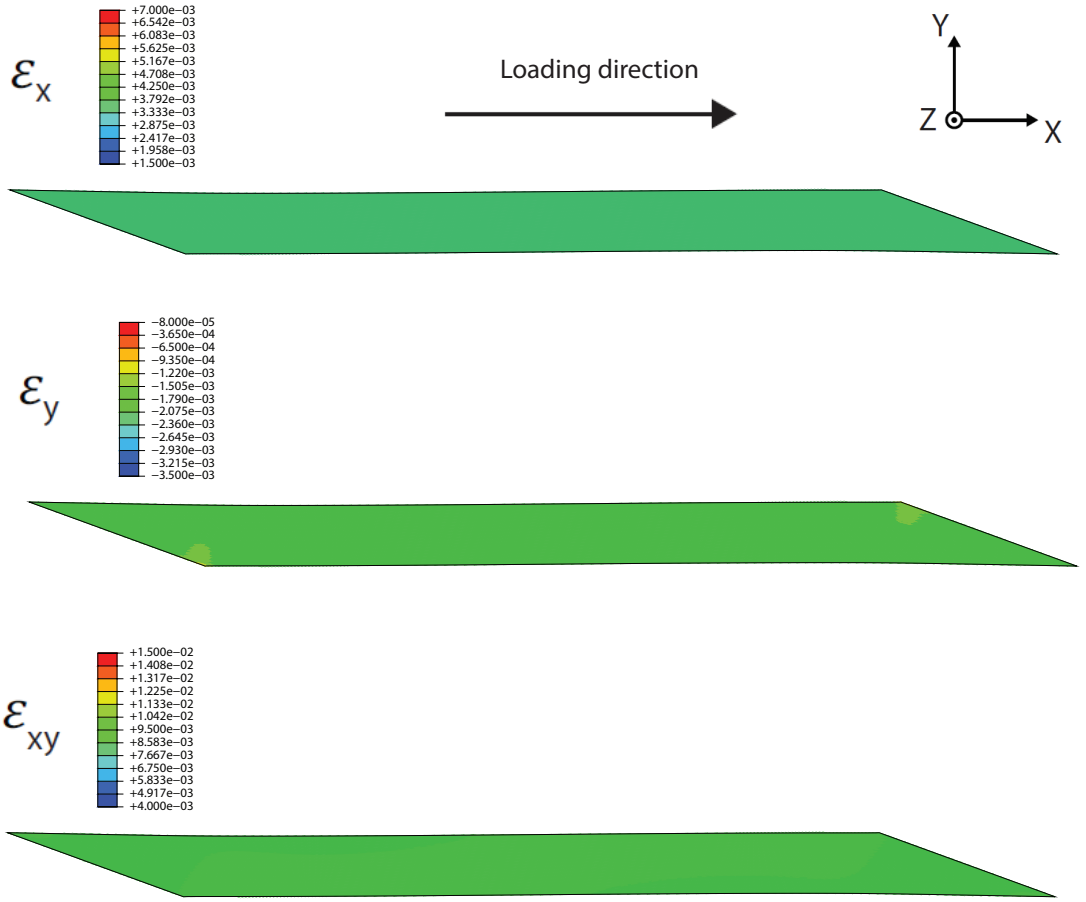

Figure 2.6: Computational maps of global strain for the 10° off-axis laminate with oblique end-tab design at 4.5 KN. It is considered a deformation factor of x30.

different sections along each specimen. As presented in Table 2.3, the values of ultimate stress obtained using oblique end-tab are higher than the ones obtained for the straight end-tab. This fact is justified because the straight end-tabs induce strain concentrations that make the specimen fail prematurely. This fact was clearly observed in Figure 2.5 by means of numerical results. In table 2.3, the mean and standard deviation of the failure stress are calculated for the two different end-tab designs. It is observed that the failure stress for each specimen using oblique end-tab is closer to the mean value than in the case of the straight end-tab, therefore, using the oblique end-tab design, the repeatability of the final applied stress is higher than in the case of the straight end-tab.

In Figure 2.7, the experimental crack pattern for the specimen with straight end-

	specimen	$F^u[N]$	$A[m]$	$\sigma_x^u[MPa]$
Straigh glass/epoxy tabs	1	6020	$1.59 \cdot 10^{-5}$	376.9
	2	6220	$1.75 \cdot 10^{-5}$	354.6
	3	4920	$1.42 \cdot 10^{-5}$	344.6
	Mean			358.7 $\pm$16.53
Oblique glass/epoxy tabs	4	5581	$1.42 \cdot 10^{-5}$	393
	5	5750	$1.46 \cdot 10^{-5}$	393.5
	6	5550	$1.45 \cdot 10^{-5}$	380.6
	Mean			389.03 $\pm$7.3

Table 2.3: Experimental average area A, ultimate force F^u and ultimate stress failure σ_x^u for straigh and oblicue end-tab design

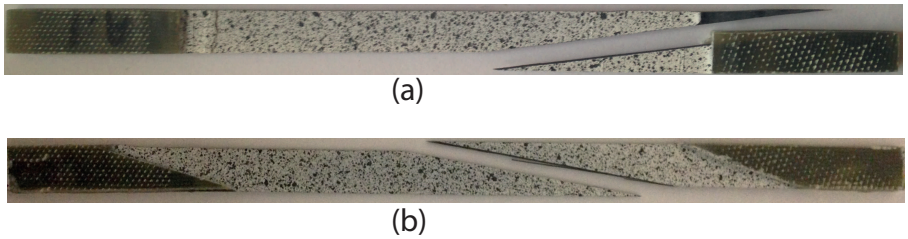

Figure 2.7: (a) Experimental crack path for the specimen with straight end-tab and (b) for the specimen with oblicue end-tab

tab (Figure 2.7 (a)) and for the specimen with oblique end-tab (see Figure 2.7 (b)) are presented. It is observed that the crack runs throughout the matrix following a clean crack path in the fibre direction. Although, the crack runs at 10° for both specimens, different locations of the crack, depending on the end-tab design are observed. In the case of the specimen with straight end-tab, the crack is developed close to the end-tab. This is not surprising since in the FE analysis a strain concentration in the clamped zone (which is induced by bending and shear force) was observed. This fact makes the specimen fail prematurely compared with the specimen with oblique end-tab. On the other hand, the specimen with oblique end-tab presents a clean crack path in the middle of the specimen as a consequence of the homogeneous strain field (see Figure 2.6).

2.2.3.1 Digital Image Correlation (DIC)

In section 2.2.2, the maps of strain along the specimens provided by the FE simulations are presented. Those results allow us to predict that the specimen with oblique end-tab presents a more homogeneous strain field than the specimen with straight end-tab. However, this fact has to be validated. In this subsection, an experimental analysis of the strain field of the specimens is carried out. The results obtained will allow the comparison, in real conditions, of the two different end-tab designs. The experimental technique used is the so-called DIC. This tool was developed in the 1980s and it is based on digital image processing and numerical computing [110] [30] [141]. This technique is a non-interferometric tool that provides the full-field displacements and strains by comparing a digital image reference (un-deformed) with a deformed image stage. In this analysis, it is considered the two-dimensional DIC approach, hence, in-plate deformation measurement of the planar surface is addressed. The DIC technique presents advantages compared with interferometric optical techniques [108] such as its simple setup and specimen preparation, its low dependency for environment conditions and its wide range of measurement sensitivity. In Figure 2.8, the experiment setup made in this experimental analysis is illustrated. The camera was placed perpendicular to the specimen ś flat surface in order to consider the out-of-plane motion of the specimen small enough to be neglected. Two white light sources were placed in both sides of the camera during loading. On the specimen surface, a random speckle patter that deforms with the specimen is artificially made by first spraying, a homogeneous white paint followed by a black speckle. This leads to a random structures aspect that is observed by the camera.

The procedure used for the determination of the whole-field displacements in the specimen is as follows: the random speckle pattern is recorded in two moments; the first one is before loading the specimen and the second is when the specimen is deformed. Afterwards, by correlating sub-images between those images it is possible to determine the surface displacement vector. To address the degree of similarity between the reference and the deformed image a cross correlation (CC) criterion or sum-squared difference (SSD) correlation criterion may be defined [50]. In literature, several correlation criteria may be defined such as CC, SSD, normalised cross-correlation (NCC), zero normalised cross-correlation (ZNCC), normalised sum-squared difference (NSSD)

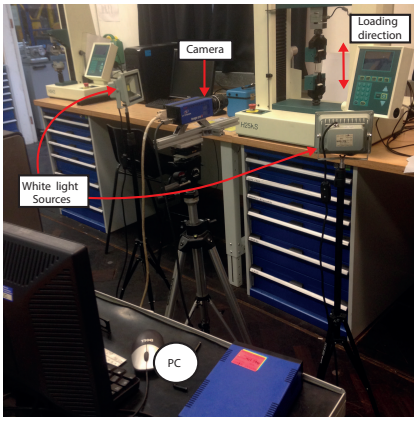

Figure 2.8: Experimental set-up of DIC.

and zero-normalized sum-squared difference (ZNSSD). According to Tong [143], ZNSSD and ZNCC presents higher robustness and reliability especially for variable lighting or exposure problems.

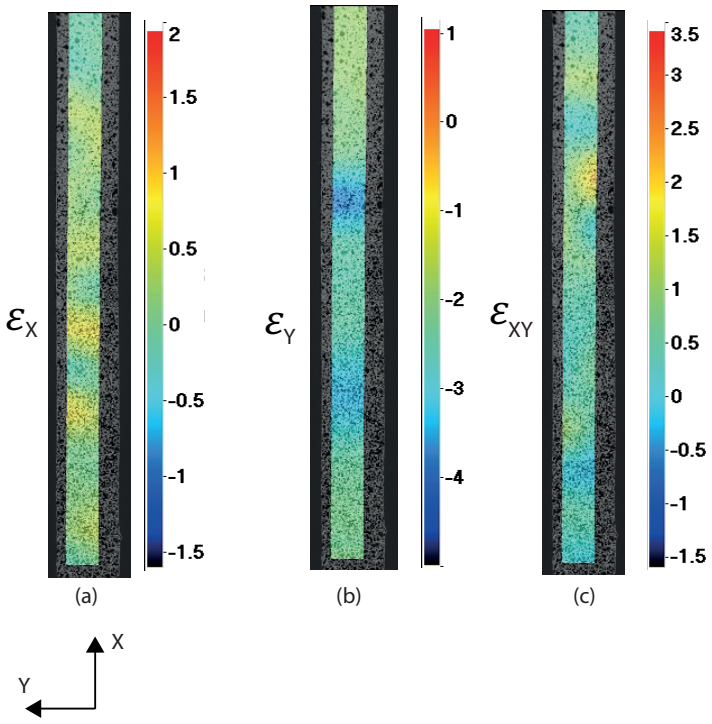

Figure 2.9: DIC analysis of the 10° laminate with oblique end-tab design. The scale represents % of strain

In Figure 2.9, the experimental maps of strains for the oblique specimen are pre-

sented. The load is applied in the x-direction and the average strain in this direction ϵ_x is 0.38 % (see Figure 2.9(a)), which is similar to 0.37 % obtained by means of simulations. As depicted on Figure 2.9 (c), the higher values of strain are observed in the shear strain map ϵ_{xy}. In this case, the average shear strain is calculated as 1.2 % which is similar to the value obtained by means of simulations which was 1.1 % (see Figure 2.6). A shear strain concentration in Figure 2.9(c) (yellow zone) is observed. This zone is where the crack is initiated. Figure 2.10 presents the maps of strain obtained for the specimen with straight end-tab. For a fixed load of 4.5 KN, the values of strain in the loading direction ϵ_x (see Figure 2.10 (a)) for the specimen with straight end-tab are higher than the ones obtained for the specimen with oblique end-tab (see Figure 2.9 (a)). The higher values of strain for this specimen are presented in Figure 2.9 (c) where the map of shear strain is presented. In this case, no peak of shear strain along the specimen is observed. This is justified because the macro crack is located close to the end-tab and it was not addressed by the DIC analysis.

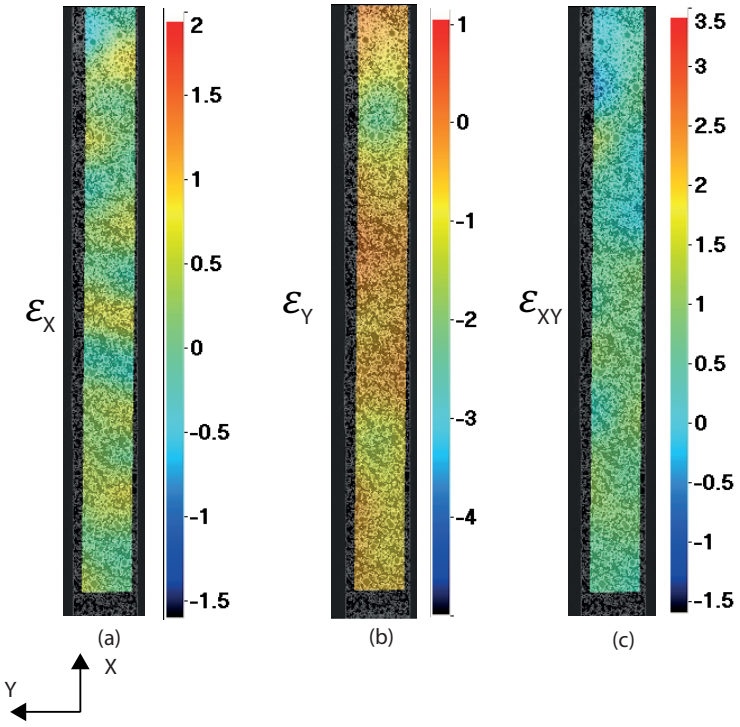

Figure 2.10: DIC analysis of the 10° laminate with straigh end-tab design. The scale represents % of strain

2.3 Limitation of progressive damage modelling

The specimen with oblique end-tab (see Figure 2.2) presents a lay-up sequence where the fibres are oriented in the same direction for all plies. Experimentally, the crack observed follows a 10° path (see Figure 2.7 (b)) and in a quasi-instantaneous event the crack grows though the matrix. In order to assess the computational crack behaviour of the 10° off-axis laminate, the anisotropic damage model proposed by Lapczyk and Hurtado [77] is considered. Through this analysis, it is possible to point out a limitation encountered in PDM and this limitation will serve as a motivation for the work carried out in the following chapters.

2.3.1 2D progressive damage analysis

2.3.1.1 Constitutive model

The model is formulated in plane stress and takes into account the constitutive model proposed by Matzenmiller et al. [86]. Three characteristic parts are considered, in the first stage, the material is linear elastic (see Eq. (2.3)). Once the material achieves a specific state of stresses determined for an initiation criteria based on stress, the material degradation starts. The model is capable of addressing the different damage scenarios and it considers four different damage modes: fibre tension, fibre compression, matrix tension and matrix compression. In order to implement the material degradation in the constitutive relation, a set of damage variables are considered for each of the different damage modes. Then, after damage initiation, the corresponding constitutive damaged matrix D_d is defined as:

$$D_d = \frac{1}{Q}\begin{bmatrix} (1-d_f)E_1 & (1-d_f)(1-d_m)\nu_{12}E_1 & 0 \\ (1-d_f)(1-d_m)\nu_{21}E_1 & (1-d_f)E_2 & 0 \\ 0 & 0 & Q(1-d_s)G_{12} \end{bmatrix} \tag{2.4}$$

where d_f, d_m, and d_s are the damage variables for fibre, matrix and shear failure modes, respectively and $Q = 1-(1-d_f)(1-d_m)\nu_{12}\nu_{21}$. The damage variables are ranged between zero (undamaged state) and one (fully damaged state for the corresponding damage mode). In this model, the damage variable corresponding to shear, d_s is defined as a function of the other two independent damage variables as;

$$d_s = 1-(1-d_{ft})(1-d_{fc})(1-d_{mt})(1-d_{mc}) \tag{2.5}$$

The damage variables d_f and d_m have different values for tension and compression which will be identified by the subscripts t and c. The initiation criteria considered for this model is the Hashin 's initiation criteria [56, 58]. It considers four different damage initiation mechanisms: fibre rupture, fibre compression, matrix tension and matrix compression and its mathematical definition is described as;

Fibre tension ($\hat{\sigma}_{11} \geq 0$)

$$F_{ft} = \left(\frac{\hat{\sigma}_{11}}{X^t}\right)^2 \tag{2.6}$$

Fibre compression ($\hat{\sigma}_{11} \leq 0$)

$$F_{fc} = \left(\frac{\hat{\sigma}_{11}}{X^c}\right)^2 \tag{2.7}$$

Matrix tension ($\hat{\sigma}_{22} \geq 0$)

$$F_{mt} = \left(\frac{\hat{\sigma}_{22}}{Y^t}\right)^2 + \left(\frac{\hat{\sigma}_{12}}{S^L}\right)^2 \tag{2.8}$$

Matrix compression ($\hat{\sigma}_{22} \leq 0$)

$$F_{mc} = \left(\frac{\hat{\sigma}_{22}}{2S^T}\right)^2 + \left[\left(\frac{Y^C}{2S^T}\right)^2 - 1\right]\frac{\hat{\sigma}_{22}}{Y^C} + \left(\frac{\hat{\sigma}_{12}}{S^L}\right)^2 \tag{2.9}$$

In the equation presented above, $\hat{\sigma}_{ij}$ represents the components of the effective stress tensor, X^T and X^C are the tensile and compressive stress in the fibre direction; Y^T and Y^C are the tensile and compressive strength in the matrix direction, S^L and S^T represents the longitudinal and the transverse shear strength, respectively.

The evolution of each damage variable d_i is controlled by an equivalent displacement [77] and the following relation for each failure mode i is defined:

$$d_i = \frac{\delta_i^u(\delta_i - \delta_i^o)}{\delta_i(\delta_i^u - \delta_i^o)} \tag{2.10}$$

where $i \in \{ft, fc, mt, mc\}$, δ_i^o represents the equivalent displacement at the peak for the failure mode i, δ_i^u represents the ultimate displacement for a i damage mode i.e. when $d_i = 1$ (see Figure 2.11) and δ_i satisfies $\delta_i^o \leq \delta_i \leq \delta_i^u$. The equivalent displacements and stresses for each of the damage modes considered are presented in Table 2.4. Note that the symbol <> in the equations presented on Table 2.4 represents the Macaulay operator.

In order to fully define a linear strain-softening, a value of critical fracture energy G^c needs to be specified for each failure mode i.e. fibre tension G_{ft}, fibre compression

Failure mode	δ	σ
Fibre tension ($\hat{\sigma}_{11} \geq 0$)	$L_c < \epsilon_{11} >$	$\frac{L_c(<\sigma_{11}><\epsilon_{11}>)}{\delta_{ft}}$
Fibre compression ($\hat{\sigma}_{11} \leq 0$)	$L_c < -\epsilon_{11} >$	$\frac{L_c(<-\sigma_{11}><-\epsilon_{11}>)}{\delta_{fc}}$
Matrix tension ($\hat{\sigma}_{22} \geq 0$)	$L_c\sqrt{< \epsilon_{22} >^2 + \epsilon_{12}^2}$	$\frac{L_c(<\sigma_{22}><\epsilon_{22}>+\sigma_{12}\epsilon_{12})}{\delta_{mt}}$
Matrix compression ($\hat{\sigma}_{22} \leq 0$)	$L_c\sqrt{< -\epsilon_{22} >^2 + \epsilon_{12}^2}$	$\frac{L_c(<-\sigma_{22}><-\epsilon_{22}>+\sigma_{12}\epsilon_{12})}{\delta_{mt}}$

Table 2.4: Equivalent displacement and stresses for each damage mode considered.

G_{fc}, matrix tension G_{mt} and matrix compression G_{mc}. However, those values were not obtained during experimental testing.

In this model, a characteristic length L_c, which allows to define the constitutive law as a stress-displacement relation (see Figure 2.11), is considered. In Figure 2.11, σ_i^o is the value of peak stress at the i mode of failure. The grey area i.e. the area under the curve stress-displacement, represents the fracture energy for the damage mode considered. Then, the energy for each damage mode i can be obtained as $G_i^c = \frac{\delta_i^u \sigma_i^o}{2}$. Since the material under analysis is brittle, it is assumed that:

- The ultimate displacement δ_i^u for each damage mode is 1% higher than the peak displacement δ^o
- There is no contribution of shear stress to the fibre tensile initiation

Taking into account the equivalent displacement presented in Table 2.4, the fracture energy for fibre rupture is defined as $G_{ft}^c = \frac{1.01 \cdot L_c \cdot \epsilon_{ft}^0 \cdot X_t}{2}$ where ϵ_{ft}^0 is the corresponding strain at the peak value of stresses and its value is obtained as $\epsilon_{ft}^0 = \frac{X_t}{E_1}$ which is a simplification of the constitutive relation. Equivalent to the tensile case, the fracture energy for fibre under compressive loading is defined as $G_{fc}^c = \frac{1.01 \cdot L_c \cdot \epsilon_{fc}^0 \cdot X_c}{2}$ where ϵ_{fc}^0 is the corresponding value of strain for the peak load obtained as $\epsilon_{fc}^0 = \frac{X_c}{E_1}$. In the case of the damage mode connected with the matrix, it is assumed that the significant term that aim failure is the shear since the values of shear strain are one order of magnitude higher than the ones perpendicular to the fibre direction. Hence, the fracture energy for the matrix tensile is calculated as $G_{mt}^c = \frac{1.01 L_c \epsilon_{mt}^0 S_L}{2}$ and for the matrix compression $G_{mt}^c = \frac{1.01 \cdot L_c \cdot \epsilon_{mc}^0 \cdot S_L}{2}$. Taking into account the elastic matrix that relates stress and

strain, the values of fracture energy for each damage mode are presented in Table 2.5. In this case, the characteristic length is defined as $L_c = \sqrt{A_{(e)}} = 7.07e^{-4}m$ being $A_{(e)}$ the average area of an element for a mesh of 2400 elements.

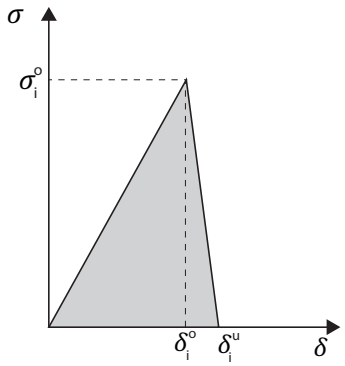

Figure 2.11: Stress-displacement law for each damage mode i.

Ply strength	Energy
X_t 2600 MPa	G^c_{ft} 13834 $\frac{N}{m}$
X_c 1500 MPa	G^c_{fc} 4606.2 $\frac{N}{m}$
Y_t 56 MPa	G^c_{mt} 94.56 $\frac{N}{m}$
Y_c 56 MPa	G^c_{mc} 94.56 $\frac{N}{m}$

Table 2.5: Material parameters for off-axis test in the principal directions.

It is important to note that when the material presents strain-softening and strain localisation, the formulation provides a high mesh dependency of the results, hence the energy dissipated decreased under mesh refinement. In order to correct the mesh dependency, the crack band model proposed by Bažant and Oh [12] is adopted. Considering the crack band model for avoiding mesh dependency, the ultimate strain ϵ^u is not kept constant and it is changed in a way that the fracture energy is conserved;

$$\epsilon^u = \frac{2G}{\sigma^y L_c} \tag{2.11}$$

where σ^y is the peak stress. The model deals with strain-softening and stiffness degradation that may provoke convergence difficulties and so, abortion of the simulation. To overcome this, a viscous regularisation scheme is considered. By means of

this strategy the tangent stiffness matrix of the softening material is positive defined for small time increments during simulations. If viscous regularisation with a small value of viscosity parameter η (small compared with the time increment) is considered, the convergence of the model in the softening state is improved without affecting the results significantly.

2.3.2 Results

Taking into account the 2D PDM presented in Section 2.3.1.1, the specimen with the oblique end-tab design was considered for numerical analysis. In order to aim computational failure, a displacement in x-direction on the right edge is applied incrementally leaving the vertical DOFs free. As shown in Section 2.2.2, the maps of strains in the oblique specimen are homogeneous. Therefore, the corresponding state of stresses are homogeneous and no stress concentration is localised. For a better understanding of this fact, in Figure 2.12 the function F_{mt} (see Eq. 2.8) is plotted for the whole specimen. In this graph, F_{mt} informs when an element along the mesh satisfies the initiation criteria for matrix cracking i.e. failure. As depicted in Figure 2.12, the Hashin initiation criteria for matrix cracking is satisfied in the whole specimen at once due to the homogeneous state of stresses along the specimen.

Due to the homogeneity of the stress field, the crack is obligated to be initiated in the area so-called "weak zone" in Figure 2.15 (a) which is 1x1 mm^2. According to experiments (see Section 2.2.3), this assumption is realistic for the specimen with oblique end-tab since, in all specimens tested, the crack initiates in the central zone of the specimen and not next to the end-tab like the specimens with straight end-tab. The square area defined presents a longitudinal shear strength $S_L = 50MPa$, which is 44 % lower than the intact material (see Table 4.1). For this analysis, the dimensions of the specimen are the ones depicted in Figure 2.2.

Figure 2.13 shows the force-displacement curve for different meshes: 1040, 2400 and 3760 elements. Once the mesh has a reasonable size the results converge to a unique solution, consequently, a higher mesh refinement does not improve the computational solution but it does increase the computational cost. As depicted, the crack band model seems to alleviate the mesh-dependency of the solution for a reasonable mesh size when strain-softening and strain location occurs. Hence, the energy dissipated does not decrease upon mesh refinement and it is maintained constant. In order to improve

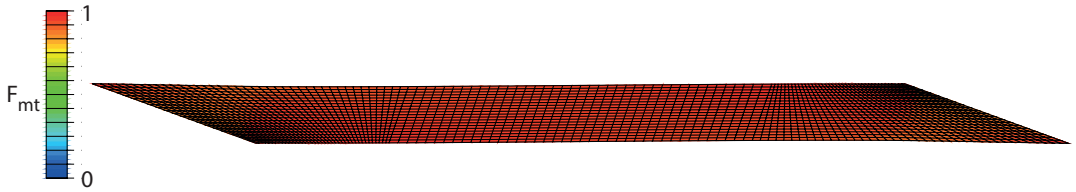

Figure 2.12: Hashin matrix tensile map for the specimen considering a mesh with 2400 elements.

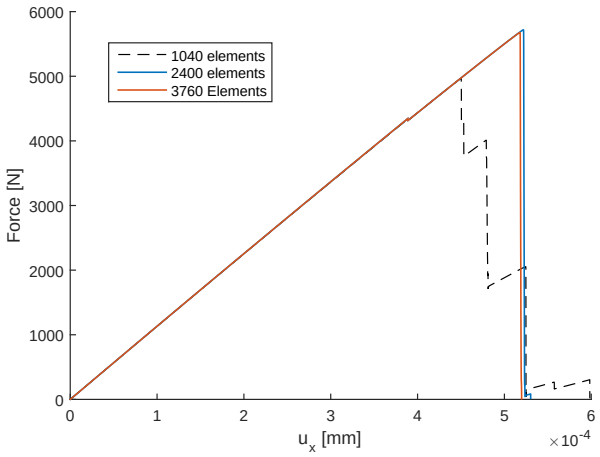

Figure 2.13: Force versus displacement in the right end-side of the specimen for a mesh of 1040,2400 and 3760 elements.

the convergence of the numerical approach, a constant value of viscosity parameter is considered $\eta = 1 \cdot 10^{-6} s$ for all damage modes.

In Figure 2.15 (b) (c) and (d), a detailed view of the specimen in the zone where the crack is initiated i.e. weak zone, is depicted. In this graph, the maps of initiation for matrix cracking according to the Hashin criteria are depicted in three different stages of the damage propagation. Those maps are equivalent to the ones obtained by means of the plot of the damage variable for matrix cracking d_{mt}. In Figure 2.15 it is observed that the failure pattern of the specimen it does not correspond with the experimental tests where the crack path follows the fibre direction. In fact, in Figure 2.15 it is observed that, after the computational crack is initiated in the weak zone, the crack path follows a wrong path. This mechanics of failure is also observed in the deformed mesh (see Figure 2.14) of the specimen. The reason for this behaviour relies on the fact

that the direction of propagation is governed by the stress concentration instead of the fibre direction. Thus, this behaviour is a consequence of the homogenisation present in continuous models [146].

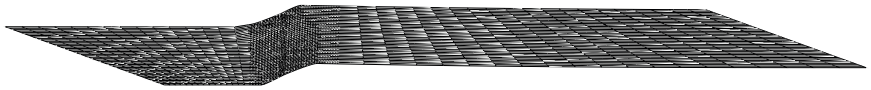

Figure 2.14: Deformed mesh of the specimen after failure for a mesh of 3740 elements.

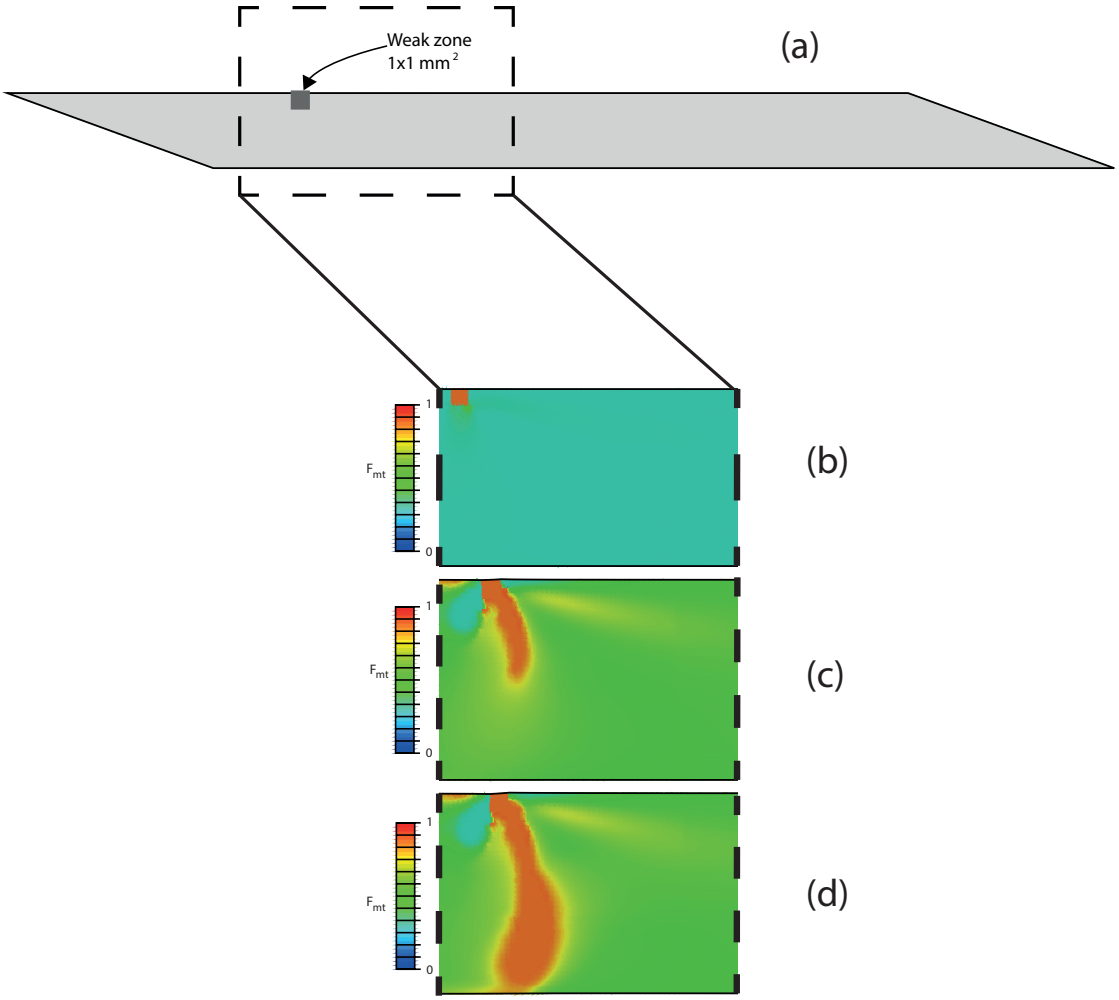

Figure 2.15: Map of damage due to matrix cracking in the specimen. A weak zone of 1 by 1 mm has been defined to localise the crack.

2.4 Conclusions

In this chapter, a 10° off-axis laminate has been design, manufactured and computationally analysed. A PDM has been considered for addressing the crack path in the 10° off-axis laminate. The predicted crack path obtained by means of simulations using PDM is different from the crack path observed experimentally. During experimental testing, the matrix cracking is observed along the fibre direction. Hence, the fail of the PDM in addressing the crack path correctly relies on the fact that the direction of crack propagation is induced by the stress concentration rather than by fibre direction. The failure of the PDM in addressing the crack mechanist observed serves to justify the work carried out in the following chapters.

3

Static and dynamic analysis of a cruciform structure subjected to biaxial loading: A discontinuous approach

3.1 Introduction

In this chapter, a structural integrity analysis using XFEM is considered for simulating the crack behaviour of a chopped fibre-glass-reinforced polyester (CGRP) cruciform specimen subjected to a quasi-static tensile biaxial loading [99]. This is the first time this problem is accomplished for computing the stress intensity factors (SIFs) produced in the biaxially loaded area of the cruciform specimen. A static crack analysis for the calculation of the mixed-mode SIFs is carried out. SIFs are calculated for infinite plates under biaxial loading as well as for the CGRP cruciform specimens in order to review the possible edge effects. A ratio relating the side of the central zone of the cruciform and the crack length is proposed. Additionally, the initiation and evolution of a three-dimensional crack are successfully simulated. Specific challenges such as the 3D crack initiation, based on a principal stress criterion, and its front propagation, in perpendicular to the principal stress direction, are conveniently addressed. No initial crack location is pre-defined and an unique crack is developed. Finally, computational outputs are compared with theoretical and experimental results validating the analysis.

3. STATIC AND DYNAMIC ANALYSIS OF A CRUCIFORM STRUCTURE SUBJECTED TO BIAXIAL LOADING: A DISCONTINUOUS APPROACH

In this chapter, the author presents a structural integrity analysis using XFEM for simulating the crack behaviour of a chopped fibre-glass-reinforced polyester (CGRP) cruciform specimen subjected to a quasi-static tensile biaxial loading [99]. This is the first time this problem is accomplished for computing the stress intensity factors (SIFs) produced in the biaxially loaded area of the cruciform specimen.

In addition, due to the collaboration with Dr. Serna Moreno from the University of Castilla-la Mancha (Spain), the 2D crack initiation and propagation in the cruciform specimen subjected to quasi-static biaxial loading were analysed numerically [125]. This work was the first attempt to investigate with XFEM the crack initiation and propagation on a randomly oriented fibre composite under biaxial loading. This collaboration has not been included in this thesis since Dr. Serna Moreno was the corresponding author of the manuscript [125].

3.2 Cruciform structure

In industrial applications using ACM, different complex loading cases are observed. For instance, in the fuselage of an aircraft, multi-axial loadings perform during working conditions. Then, it is required a better understanding of these materials under multiple loading in different directions [132]. For this reason, in this thesis, the computational behaviour of a cruciform structure is studied (see Figure 3.1). This structure was initially designed by Serna et al. [126] and it is formed by CGRP composite that behaves experimentally in a quasi-isotropic manner [126],[127]. This fact is justified because of the uniformly random distribution of the fibres throughout the matrix. The ACM tested owns a polymer matrix with 20% volume of glass fibre reinforcement.

The design of this structure is intended to localize a biaxial loading stress state in its central zone i.e. the intersection of both arms. In order to aim that, a tensile load in the longitudinal direction of each arm is applied. As depicted in the detail view of Figure 3.1, a milled zone in the central part is observed. The objective of that is to aim higher stresses in the central zone compared with the rest of the specimen [126]. Three different cruciform geometries A, B and C (Figure 3.1) are studied. The material properties are depicted in Table 3.1. In that table, E represents the modulus

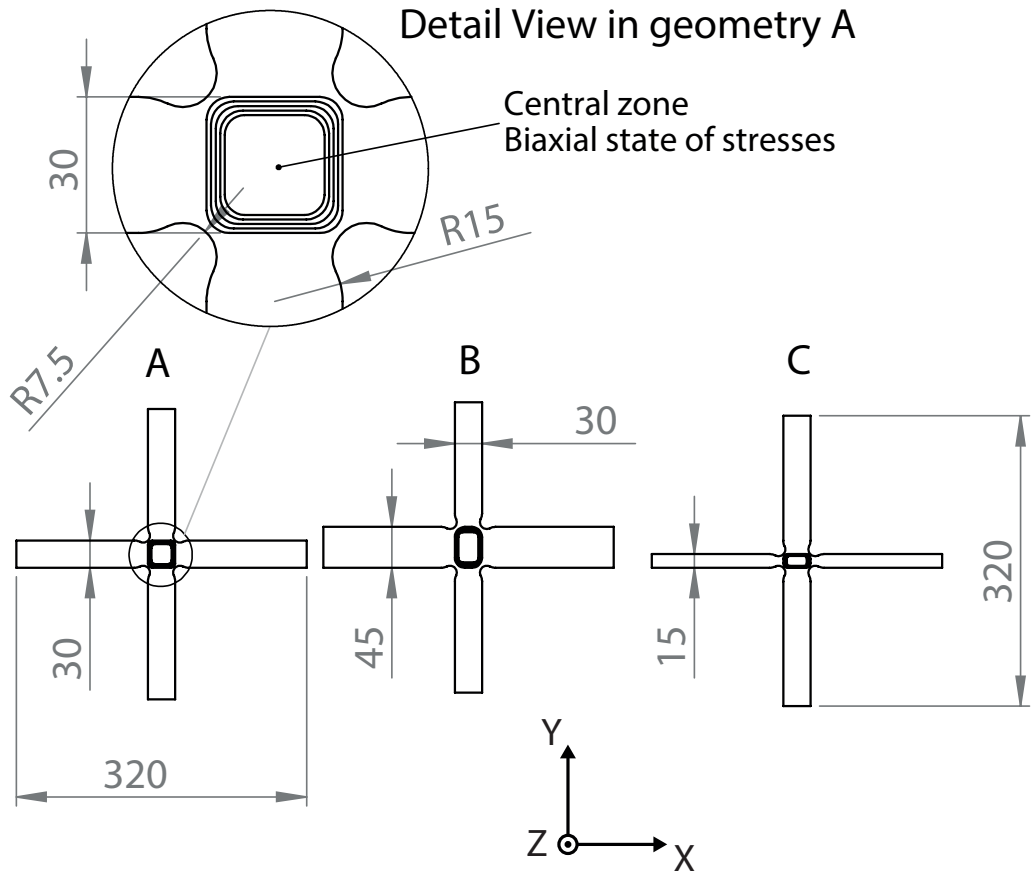

Figure 3.1: The three different cruciform structures studied. Additionally, a detail view of the geometry A is given for localizing the zone where a biaxial state of stresses occur. Dimensions are in millimeters.

of elasticity, υ the Poisson ratio, ϵ_{yield} the yield strain and σ_{yield} the yield strength which are obtained in [127].

$Density[Kg/m^3]$	$E[MPa]$	υ	$G[MPa]$	$\sigma_{yield}[MPa]$	ϵ_{yield}	$G_I^C[N/m]$
1440	6500	0.37	2370	90	0.0138	6210

Table 3.1: Material parameters

Geometry A has the same width in both arms while in geometries B and C the width of the arm in the direction x changes respect to the arm in the y direction that remain constant (see Figure 3.1). In geometry B, the width of the arm in x direction

is 1.5 times the width of the arm in the y direction and geometry C has an arm in x direction that it is half of the width of the y arm. The CGRP presented in this work is used in internal coating and the frontal parts used in trains (see Figure 3.2). This composite substitutes the traditional materials used in trains due to its lower weight and its high resistant to corrosion.

Figure 3.2: Aplication of the CGRP composite under analysis. Image provided by UCLM.

3.3 A 3D discontinuous approach/model based on the eXtended Finite Element Method

Experimentally different biaxial loading cases are applied in each cruciform. These loading cases cause failure through the diagonal of the central zone. 1/8 of the model for each geometry is simulated due to the symmetry. The boundary conditions applied to the three different geometries are depicted in Figure 3.3. Also, the cruciform specimen is fixed in the out-of-plane direction.

For the finite element discretization, eight node hexahedral elements with reduced integration and three degrees of freedom per node are chosen (C3D8R). Reduced integration may provoke spurious zero-energy modes that provides an unreal solution. Therefore, hourglassing control is considered. A mesh convergence analysis was carried out for obtaining an adequate size mesh in this cruciform specimen under analysis [126] . Two different average size meshes are defined: 1.5 mm in the arms of the cruciform specimen and 0.5 mm in the central zone. In previous work, it was presented a two-dimensional crack initiation and propagation analysis [125]. The computational results

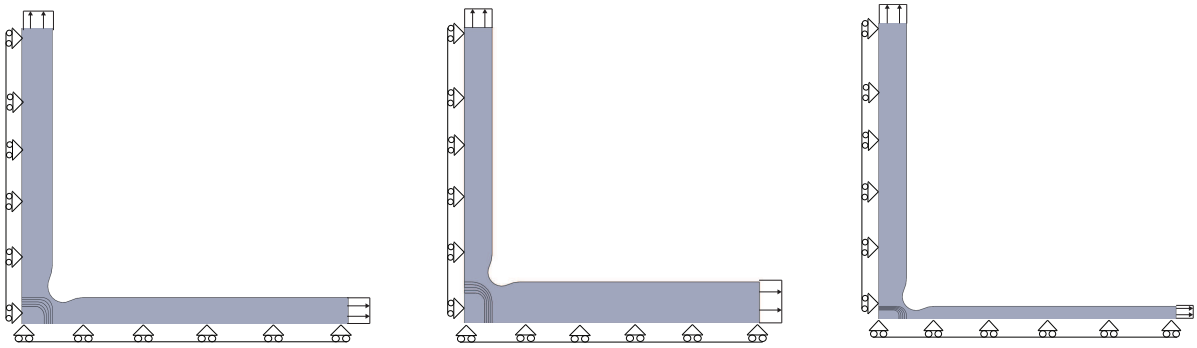

Figure 3.3: Boundary conditions considered in the simulations for the three different cruciform geometries under biaxial loading: A,B and C.

were validated by means of comparison with experimental results. In this chapter, the main objective is focused in the calculation of SIFs for the real cruciforms submitted to biaxial loading as well as quantify the edge effects into each geometry. For making that possible, previous computational tests are needed. It is important to notice that in this Chapter a 3D model is simulated. This model has not been validated before and higher numerical complexity is expected compare with the 2D case. Therefore, in Section 3.3.1 crack initiation and propagation is simulated within the 3D cruciform and compared with experimental outcomes. By means of this first computational analysis the three-dimensional abilities of XFEM are demonstrated. With the confidence of this analysis, the author is able to go further when dealing with a 3D model. In Section 3.3.2, a 3D static crack analysis is carried out. This section can be divided into two main parts. The first part, Section 3.3.2.1, considers a quasi-infinite plate subjected to biaxial loading. Those plates are equivalent to the central zone of the cruciforms and SIFs are obtained using XFEM and afterwards compared with the theoretical solution. This analysis serves to show that XFEM is capable of accurately obtain SIFs in a bi-axial loading context. The second part, Section 3.3.2.2, it is focused in the calculation of SIFs within cruciform specimens once the capabilities of XFEM has been validated in previous sections.

3.3.1 Crack initiation and propagation

3.3.1.1 Constitutive Model

The constitutive model for modelling crack initiation and propagation into the cruciform is defined by means of three characteristic steps (see Figure 3.4) and it needs to represent the fragile fracture process of the CGRP cruciform:

- Linear elastic traction-separation behaviour (point 1 to 2 in Figure 3.4). The elastic behaviour is defined in terms of elastic constitutive matrix that relates normal and shear stresses with nominal strains.

- Damage initiation (point 2 in Figure 3.4). It is connected with the beginning of the degradation of the cohesive response in an enriched element. The criterion of initiation selected is based on maximum principal stresses $\sigma_{max} = \sigma_{yield} \pm \sigma_{tol}$. Therefore, when the maximum principal stresses σ_{max} achieve a value that it is the sum of yield stress σ_{yield} and a certain value of tolerance σ_{tol} (define by the user) the damage process starts.

- Damage evolution (point 2 to 3 in Figure 3.4). Once the initiation criterion is satisfied, damage evolution defines the degradation of the stiffness (softening). The constitutive relation is written as follows $\sigma = (1-\omega)D\delta$, where ω is a scalar variable that is responsible for the degradation of the stiffness. Initially this variable is zero (full load-carrying capability) and at the end of the degradation process this variable takes value 1 (no load-carrying capability). For a proper definition of that variable, it is requested a critical fracture energy G^C for each pure failure mode. Based on experimental observations, the dominant mode of fracture in the cruciform specimen is mode I. Then, it is assumed that the mode I of failure defines the fracture process and consequently it is defined the critical energy for pure mode I of failure G_I^C. This energy G_I^C refers to the energy dissipated during the damage process per unit area and its value in this work is estimated by means of uniaxial testing. Therefore, the energy dissipated per unit volume during damage evolution is $G_I^C = \frac{\sigma_{yield} 0.01 \epsilon_{yield}}{2}$ (Table 3.1). In this case, G_I^C is equal to the critical fracture energy per unit area because the traction-separation model considered a unitary cohesive thickness. Due to the brittle material behaviour of the composite, it is assumed that the fracture strain ϵ_u is 1% higher than the yield strain ϵ_{yield}.

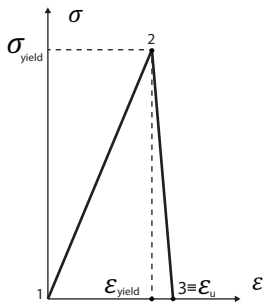

Figure 3.4: Segment form by point 1 to 2: Undamaged liner elastic behaviour, point 2: damage initiation and segment form by point 2 to 3: softening.

Difficulties of convergence using implicit solver are detected when strain-softening behaviour is modelled. For solving this issue, a viscous regularization of the constitutive equations defining the cohesive behaviour is adopted. In the regularization scheme, a viscous damage variable is defined $\omega_v = (\omega - \omega_v)/\eta$, where η is the viscosity coefficient that represent the relaxation of time of the viscous system and ω the damage variable in the inviscid model. The viscous coefficient η increments the rate of convergence of the model when it is dealing with strain-softening material behaviour. Then, using a small coefficient (small compared with a characteristic time t_c of the system) convergence can be improved. The value of the characteristic time t_c of the system is calculated using the expression $t_c = \frac{L_e}{c_d}$ where L_e is the smallest element size and $c_d = \sqrt{\frac{E}{\rho}}$ is the stress wave velocity of propagation for a material with density ρ=1147.5 $\frac{kg}{m^3}$ and modulus of elasticity E= 6.5 GPa. For this application, the characteristic time 2.1 μs. It is noticed that one of the viscous coefficient considered during crack propagation is higher than the characteristic time of the system. However, the viscous energy involved during simulations is a 0.16 % of the total internal energy stored in the system, then, the viscous regularization does not compromise the solution and realistic results are consequently provided. It is noticed that during this research the damage tolerance σ_{tol} and viscous parameter η have a considerable influence on the progression of the crack and the convergence of the solution. It is assumed that the specimen is in elastic equilibrium during the loading process so quasi-static simulations are developed employing an implicit solver for solving the momentum equation. An automatic time stepping is chosen. Maximum and minimum values of the time step are 10^{-2} and 10^{-20}

Figure	*Geometry*	Loading case	$\sigma_{tol}[Pa]$	$\eta[s]$	Initial crack
*Figure*3.5(c)	A	1/2	1	10^{-7}	No
*Figure*3.5(a)	A	1/1	1	10^{-7}	No
*Figure*3.6(a)	B	1.5/1	1	10^{-3}	No
*Figure*3.7(a)	C	0.5/1	1	10^{-3}	No

Table 3.2: Simulation parameters

respectively. 10000 increments per time step are used.

3.3.1.2 Validation of the 3D model by comparison with experimental tests

Experiments showed two main outcomes: the first is that the correct failure within the cruciform is when the crack transverse the central region submitted to biaxial loading in geometries A, B and C [126] and the second one is that each geometry owns a certain biaxial loading case where a crack is localized in the central zone. Considering that, simulations were carried out and the simulation parameters to aim a crack path crossing the central zone are presented in Table 3.2. In the current work, non a-priori crack location is defined for all geometries, thus, the crack is initiated and propagated as a solution-dependent.

Damage initiation is properly predicted by XFEM and all geometries initiated a crack at 90 MPa in the rounded zone. Geometry A is submitted to a loading case 1/1, which means that the same load is applied in both arms. As a result of this loading condition, simulation results show a crack throughout the central zone of the geometry (figure 3.5 (a)) and the crack-path followed is similar to the experimental case (see Figure 3.5 (b)). In geometry A, when the loading case is different to 1/1, an incorrect failure is detected (failure in the arm with bigger load). This fact is also predicted by XFEM. In Figure 3.5 (c), geometry A is submitted to a loading case 1/2 (double load in the vertical arm). Thus, the crack is developed in the arm suffering a higher load which is in good agreement with experiments (see Figure 3.5 (d)).

In the case of geometry B, the in-plane biaxial loading case applied is 1.5/1. As the previous example for geometry A, no pre-definition of the crack location is necessary, so as a natural outcome crack is initiated and propagated throughout the central zone. In figure 3.6 (a), it is depicted a translucent view where the surface of the crack is

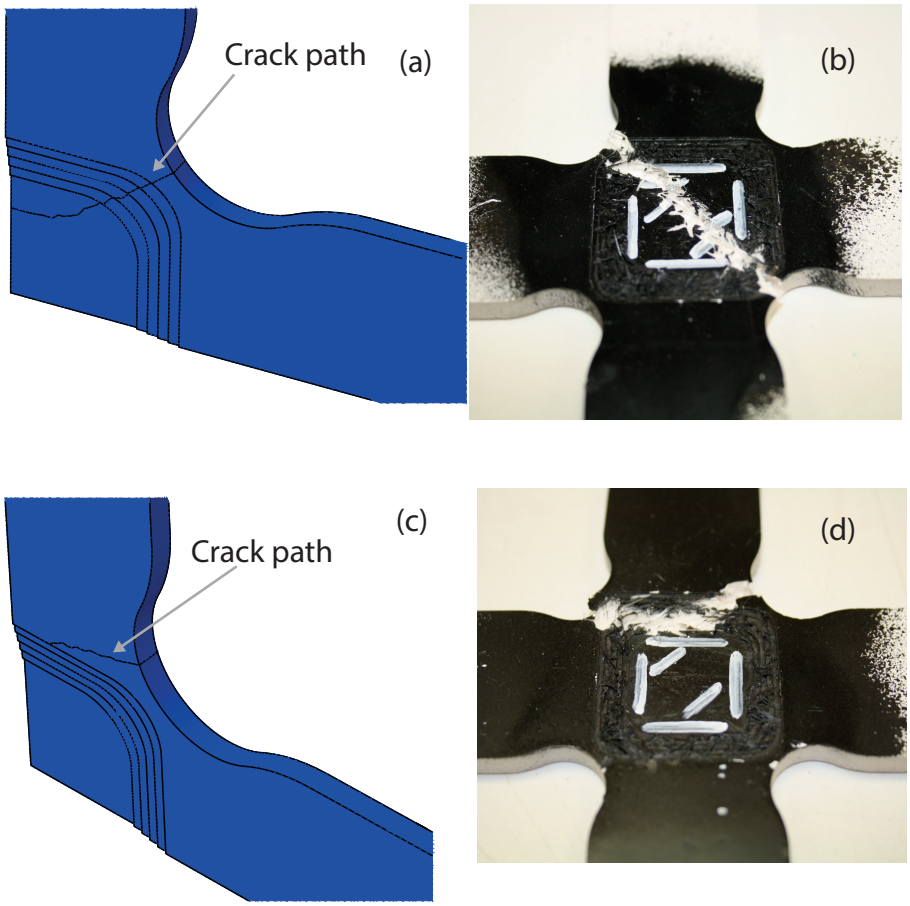

Figure 3.5: (a) Computational and (b) experimental crack propagation in geometry A under loading 1/1 without definition of a priori crack. Computational (c) and experimental (d) crack propagation in geometry A under loading 1/2 without definition of a priori crack.

appreciated in the 3D geometry. In Figure 3.6 (b) it is illustrated the experimental results for geometry B under biaxial loading 1.5/1. That figure serves to illustrate the pattern of failure to achieve the correct collapse of the cruciform i.e. across the central zone. Geometry C is under a biaxial loading 0.5/1. Experimental results (Figure 3.7 (b)) are accurately predicted by the simulations (Figure 3.7 (a)), therefore the computational crack is developed crossing the central zone.

3.3.2 Biaxial static crack analysis

In this section, a static crack analysis is carried out into the CGRP composite. Firstly, three different quasi-infinite plates are simulated with the objective of validating XFEM

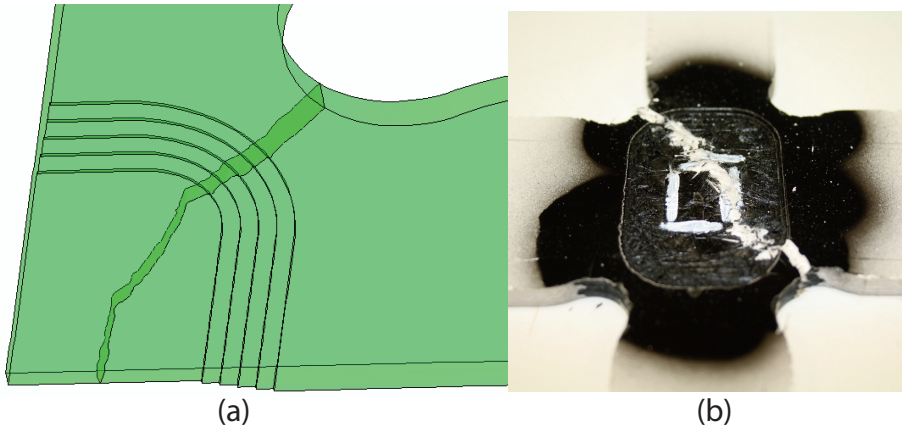

Figure 3.6: (a) Computational crack propagation in geometry B under loading case 1.5/1 without definition of a priori crack location (b) Experimental path failure in geometry B for a biaxial loading 1.5/1 [126].

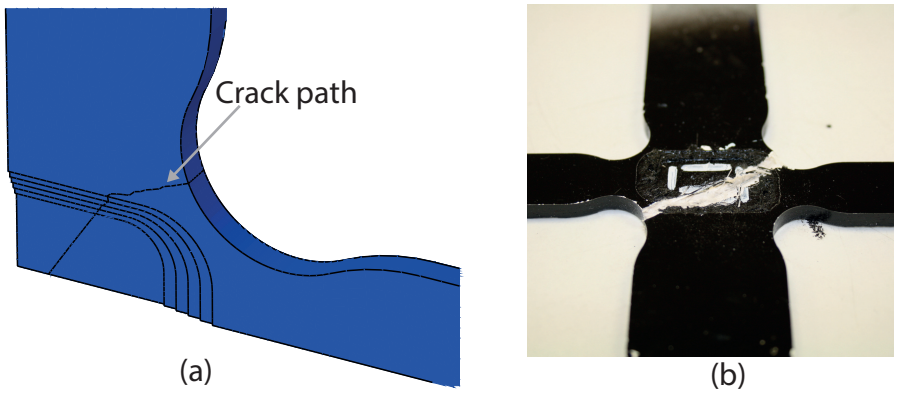

Figure 3.7: (a) Computational and (b) experimental crack propagation in geometry C under loading 0.5/1 without definition of a priori crack.

for the calculation of SIFs in a biaxial contest. The size of these quasi-infinite plates is proportional to the central zone of the cruciform specimens. Secondly, SIFs are also obtain for the real cruciforms and compared with the analytical solution for infinite plates. A 3D model is needed for studying static crack analysis [60] within the quasi-infinite plates and the cruciform specimens. The edge effects into the SIFs calculation are studied.

3.3.2.1 Inclined crack in a biaxial stress field

SIFs are calculated for infinite plates and CGRP cruciforms. SIFs are extracted from the J-integral calculation [7]. This integral is a contour integral for bi-dimensional geometries and its definition in this application is extended to three-dimensional geometries. The relation between the J-integral J and SIFs for linear elastic material [60] is given by the following equation:

$$J = \frac{1}{8\pi} K^T P^{-1} K \tag{3.1}$$

where $K = [K_I, K_{II}, K_{III}]^T$ and P the pre-logarithmic energy factor tensor. Interested readers for a better understanding of fracture mechanics concepts can consult fracture mechanics references such as [7].

In this section, the objective is to validate XFEM for calculating the mixed-mode SIFs in a 3D biaxial scenario. Therefore, the part of the structure with interest is the central zone of geometry A,B and C because it is where a biaxial loading is located. To study independently these regions, rectangular plates are considered for simulations (see Figure 3.8). The dimensions of the plates (Table 3.3) are one order of magnitude higher that the original central zone on the cruciforms to consider the study of an ideal quasi-infinite plate respect to the real critical area. Thus, the solution of the SIFs in mode-I and mode-II is admissible and its expression is [121]:

$$K_I^{Theo} = \sigma\sqrt{\pi a}(sin^2\beta + \alpha cos^2\beta) \tag{3.2}$$

$$K_{II}^{Theo} = \sigma\sqrt{\pi a}(1-\alpha)cos\beta sin\beta \tag{3.3}$$

where β is the angle form by the crack and the vertical direction, σ is the stress, a is half-crack length, K_I^{Theo} and K_{II}^{Theo} are the first and second theoretical mode SIF, respectively. α is defined as the ratio between the major and minor stress into the plate.

As it is illustrated in Figure 3.8, a centre crack is defined in each plate under analysis. This crack is 2 mm long for all geometries. The crack size chosen for this analysis is relatively small compared with the dimensions of the quasi-infinite plates considered. Therefore, the quasi-infinite plate can be considered as a infinite respect to the crack size and edge effects are then minimized. The crack under analysis is inclined with an angle β. This angle is the angle form between the crack and the vertical direction. This

angle is subtracted from experiments and corresponds with the failure angle observed in the rounded zone for each geometry. The crack path is almost constant throughout the cruciform so the crack angle observed in the rounded zone is approximately the same as the central zone. Thus, for geometry A this angle is 45°, for B 33.69° and C 63.43°. The values of the load applied to the plates in each direction are depicted on Table 3.3. These values of stress correspond with the stress failure in the central region observed during experiments. Boundary conditions and loading directions in the plate are depicted in Figure 3.8. Note that plates are also constrained in the out-of-plane direction. In Figure 3.8, W represent the width and H the hight of the plates. Thus, different values of W and H are considered for simulations as shows Table 3.3.

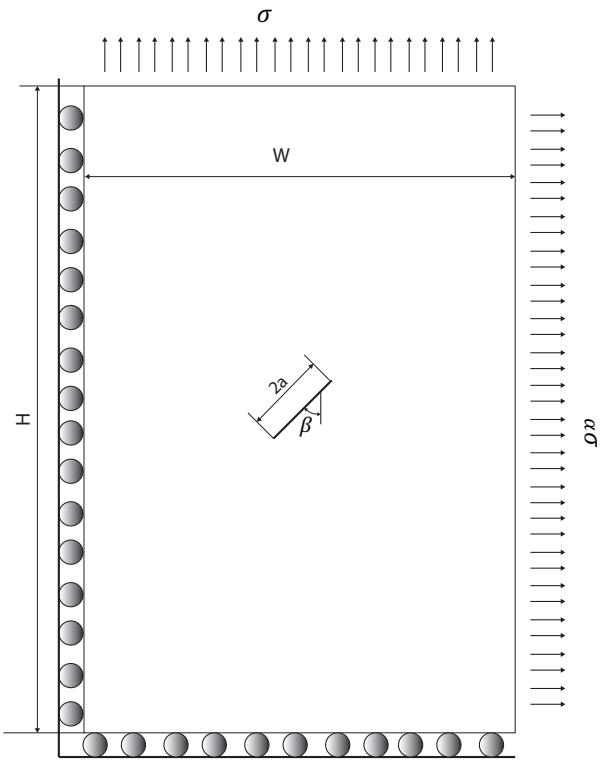

Figure 3.8: Boundary conditions of the centre crack under biaxial loading.

In the neighbourhood of the crack location, it is considered a square area of 4x4 mm around a centre crack where 2500 elements are stacked in order to capture the crack-tip stress field. The major edges of the plate are partitioned into 80 equal subdivisions for each plate. The thickness of the plate is 2 mm and two mesh subdivision are considered

Geometry	A	B	C
Dimensions plate(W|H)[mm]	220x220	220x330	220x110
Loading (σ_x-σ_y)[MPa]	84-84	81.8-49.9	48-103.5

Table 3.3: Dimensions and loading in the infinite plates considered

Geometry	β	K_I^{Theo}	K_{II}^{Theo}	K_I^{Num}	K_{II}^{Num}	$\|errorK_I\|(\%)$	$\|errorK_{II}\|(\%)$
A	45	4.70	0	4.56	0	3.06	0
B	33.69	3.34	0.82	3.36	0.85	5.68	3.01
C	63.43	5.17	1.24	5.13	1.29	0.9	3.74

Table 3.4: SIFs for a 2 mm crack in the central zone of the plate

throughout the thickness. SIFs obtain by simulations are presented in Table 3.4. The analytical solution is compared with the results obtained with XFEM.

Computationally, the J-integral is considered for the SIFs calculation. It is well-known that in theory the J-integral is path independent. However, computationally this is not true. Therefore, different contours give different solutions of SIFs. In this study five contours are taken into account. Because of numerical singularities, the first contour is not considered as it is suggested in [60]. Then, the SIFs depicted on Table 3.4 have been obtained as the mean of the five consecutive values starting from the second value of K_I and K_{II} calculated.

The theoretical values of SIFs are compared with the numerical ones obtained by means of XFEM. The small relative error appreciated between theoretical and numerical solutions confirms that XFEM is able to predict the mixed-mode fracture process here considered and validates its use for SIFs calculation considering a biaxial loading.

3.3.2.2 SIFs into the real cruciforms

In this section, SIFs are calculated for the real cruciform specimens and then compared with the theoretical solution. 1/8 of each cruciform is simulated with inclined cracks in the central zone. Different values of a i.e. half-size of the crack length, are considered, $a = 0.5, 1, 1.5, 2mm$. The angle of inclination β considered is the same as for the quasi-infinite plate analysed in previous section. Three different mesh regions can be

distinguished with different element size in the structure. The first one defined is in the central zone with a 0.5 mm size, the second one defined in the arms with 1.5 mm size and the third one in the proximity of the static crack as depicted in Figure 3.9. For the third mesh refinement, a 4x4mm square is defined surrounding the crack with 1600 elements. The loading applied in this case is on the arms of the cruciform. Then, for geometry A, $54MPa$ are applied in each arm, in geometry B, $61MPa$ and in geometry C, $44.25MPa$. These values of load in each arm are responsible for the final fracture of the structure. The values of SIFs obtain with the quasi-infinite plates presented on Table 3.4 show that the values of K_I obtained by XFEM are higher than the ones K_{II}. This fact is also observed on Figure 3.10 for the cruciform structures. These results allow us to demonstrate numerically that the dominant mode of fracture is mode I. Comparing Table 3.4 and Figure 3.10 for $a = 1mm$ (2 mm of crack length), it is observed that the values of SIF calculated for quasi-infinite plates are closer than the SIF obtained for the cruciform specimen to the theoretical solution for an infinite plate. This fact it is explained because the quasi-infinite plates represent a similar configuration than the theoretical solution for an infinite plate. As mentioned previously, a pure biaxial loading is located on the central zone of the cruciform structure. The magnitude of the horizontal and vertical stresses in this zone is the same as the ones applied in X and Y direction to the quasi-infinite plate depicted on Figure 3.8. Hence, in Figure 3.8 it is considered a quasi-infinite plate with loading conditions, angle of the crack and material properties identical as the central zone of the cruciform. Therefore, when considering these plates, the theoretical solutions for an infinite plate (Equations 3.2 and 3.3) provide SIF values close to values of SIF obtained numerically using XFEM (see Table 3.4). However, in the cruciform structure, when calculating SIF the theoretical solution for an infinite plate is not able to provide results close to the ones computed numerically (see Figure 3.12 and 3.13). This is justified because the length of the area loaded biaxially is not infinite if it is compared with the size of the crack.

In Figure 3.10 and 3.11 it is depicted the values of K_I and K_{II} obtained. These values calculated by means of XFEM are represented against the half-crack size considered for each cruciform. In theory, under a biaxial loading any increment of the crack length a (maintaining all other parameters constant) will always contribute to increment the values of SIFs. This tendency is observed numerically in Figure 3.10 and 3.11. However, it is noticed a reduction in the accuracy of the SIF calculation when

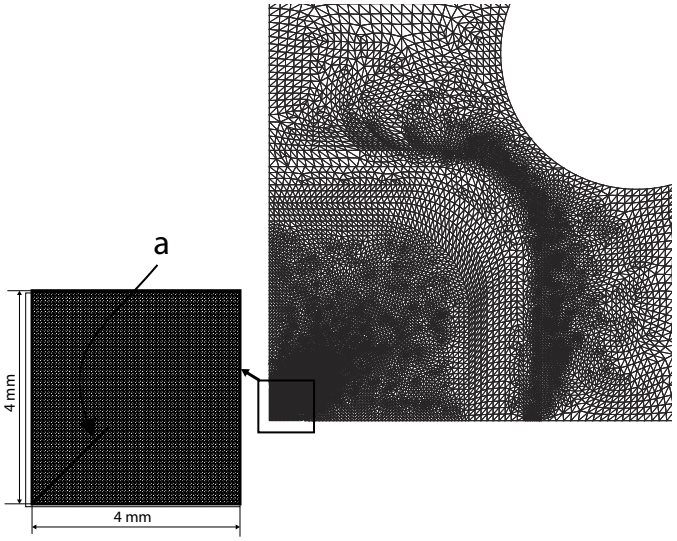

Figure 3.9: Crack location in cruciform A for SIFs calculation. Note a 4x4 quadrilateral area where a special refinement is required to accurately represent the crack-tip behaviour.

the crack size is incremented within each geometry. This is due to the edge effects that influence the SIFs calculation when using XFEM. The influence of the edge effects for the SIFs calculation depends of the size of the central zone of each geometry as shows Figure 3.12 and 3.13. In these figures, the absolute value of the relative error between theoretical and numerical solution is presented. Higher values of error for K_I and K_{II} are found in geometry C while geometry B is noticed a less influence of the edge effects. This fact is explain because geometry B has bigger central zone than geometry C, then the edge effects are mitigated when considering a crack with the same length into both geometries. In other words, the central zone on geometry B is closer to the quasi-infinite plate than the central zone of geometry C.

Considering the last outcome, a possible alternative to minimize the edge effects is to stablish a new ratio α between the crack size a and the dimensions of the central zone that will minimize the edge effects. This ratio α is based on the calculation of SIFs for geometry B. As depicted in Figure 3.12 and 3.13, the relative error of SIFs is minimum when the half-crack size is 0.5 mm. In particular, for geometry B, the absolute relative error for mode I is 1.5 % and for mode-II is 1 %. Hence, if the dimensions of the central of a cruciform structure are similar to geometry B, the edge effects may be considered negligible. Considering the major dimension of the central zone of geometry B which

is 33 mm and a crack size of 0.5 mm, α is defined as follows:

$$\alpha = \frac{L}{a} = 66 \tag{3.4}$$

In Equation 3.4, α considers a cruciform structure with a square central zone of side L. According to Equation 3.4, for a crack size bigger than $\frac{L}{66}$ not negligible edge effects into the SIF calculation are appreciated compared with the theoretical solution. Obviously, considering a specimen with a higher α edge effects are reduced. Additionally, this analysis serves to give us a first idea of the relation between central zone and the crack size and allow future experiment tests to by oriented according to the ratio presented. It is important to notice that the values of K_I are higher than K_{II} in the cruciform specimens. Therefore, taken into account the SIFs calculation with XFEM, for geometry A only mode I is observed and the shear does not exist. However, for geometry B and C it is noticed a mixed mode failure. The values of shear in geometries B and C are small compared with the normal stress. In previous studies, the shear has not been considered nevertheless here it is demonstrated computationally that it has its influence within geometry B and C.

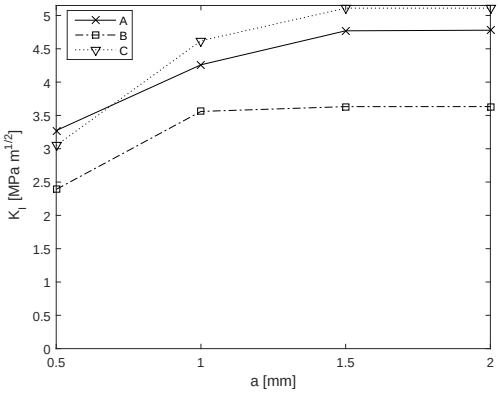

Figure 3.10: K_I obtained by means of XFEM is represented against the half-crack length a defined for geometry A,B and C.

3.4 Conclusions

In this Chapter, an investigation on the utility of the relatively novel numerical method XFEM applied to biaxial loading of composites has been presented. A static crack

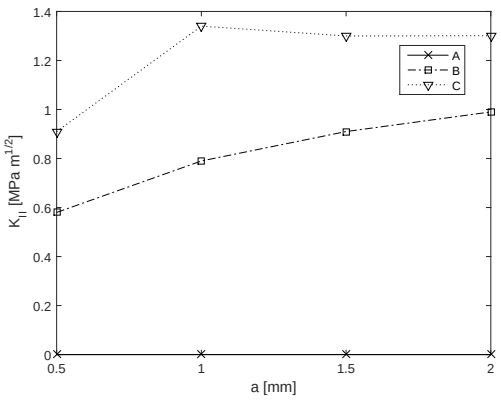

Figure 3.11: K_{II} obtained by means of XFEM is represented against the half-crack length a defined for geometry A,B and C.

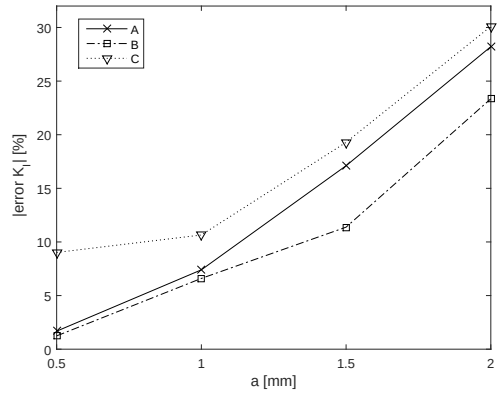

Figure 3.12: The absolute relative error for mode-I $|errorK_I|$ is represented against the half-crack length a for geometries A,B and C.

analysis is completed in order to determine the mixed-mode SIFs into CGRP cruciforms. Initially, SIFs are determined for infinite plates subjected to biaxial loading. Once the 3D XFEM model is validated, SIFs are also calculated for the whole cruciform specimens. By means of this analysis, it has been noticed that the edge effects into the cruciform specimens affects the SIFs values. The variation of SIFs values between the cruciform and the analytical solution are quantified. A ratio between the side of the central zone and the crack length is proposed in order to minimize edge effects and specimen size simultaneously. The dominant fracture mode into the cruciform structure is mode I according to the comparison between the numerical value of K_I

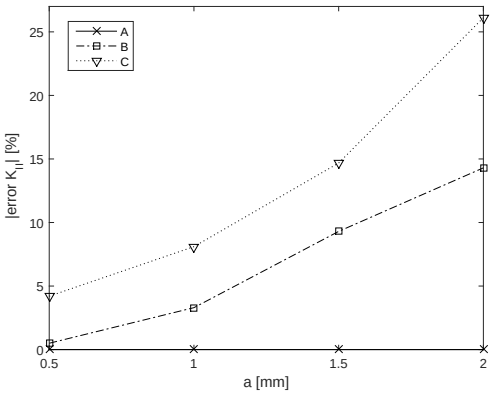

Figure 3.13: The absolute relative error for mode-II $|errorK_{II}|$ is represented against the half-crack length a for geometries A,B and C.

and K_{II}. In other words, the nominal stress is higher than the shear stress during loading in the neighbourhood of the crack tip. In the authors best knowledge, this is the first time that SIFs are calculated for this kind of CGRP cruciform specimens. Modelling initiation and propagation was not straightforward as has been shown above and challenges that are not an issue indeed becomes critical in a 3D context, overall when dealing with fracture. The following points were addressed during this research:
- Propagation of a 3D crack front without pre-notching.
- Criteria for crack initiation.
- Although re-meshing was not carried out, no deterioration of the solution was observed in terms of validation against experimental tests.
Overall, the application of XFEM here presented contributes to emphasizes that using XFEM for modelling crack in biaxial loading cases is adequate. Additionally, dealing with 3D XFEM a more realistic view of cracks is provided.

4

Mixed-mode damage into a CGRP cruciform subjected to biaxial loading

4.1 Introduction

In this Chapter, the author implements a three-dimensional progressive damage model (PDM) is implemented within a CGRP cruciform structure for modelling its damage under loading [100]. The three cruciform specimens presented in previous Chapter are studied. In order to simulate the computational behaviour of the composite, the constitutive model considers an initial elastic behaviour followed by strain-softening. The initiation criterion defined is based on the maximum principal stress of the composite and once this criterion is satisfied, stiffness degradation starts. For the computation of damage, the influence of the fibre and the matrix are taken into account within the damage rule. Realistic values of the energy dissipated during damage are computed. The computational results obtained by means of an explicit time marching solver are compared with experimental outcomes for validation purposes. Finally, it is concluded that the PDM is able to localize the damage effectively as well as predicting its initiation. In the best of authors' knowledge, this is the first time a three-dimensional PDM is implemented into a composite cruciform structure subjected to biaxial loading.

4.2 Background: Three-dimensional progressive damage model for fibre-reinforced materials

The PDM proposed by Curiel-Sosa [39] is modified in order to model damage in a cruciform structure. The main characteristic of the initial model [37] is that the paths for computation of damage offer an effective localization of the several damage modes i.e. fibre rupture, matrix cracking, etc. In addition, comparing this PDM with others from literature it is noticed a notable different. The initial PDM considers interaction between damage modes. Hence, a certain damage mode, for instance fibre rupture, is affected by others and, so that, this characteristic makes the model more realistic. In reality, during the fracture process of composite structures, damage modes are not independent. For the simulation of the CGRP cruciform structure the initial model proposed is changed. The principal adaptations of the PDM to the problem here presented are:

- Due to the quasi-isotropic material behaviour, a single damage variable is considered. This damage variable takes into account the influence of matrix cracking and fibre rupture for computing damage.

The initial model [39] is framed into strain-space damage models according to continuum damage mechanics. The thermodynamic framework of an irreversible process for dissipative materials [25] is considered as well as the idea of effective stress $\hat{\sigma}$ [26] (Eq.[4.1]). The main mathematical formulation of the model is presented in the following equations:

1. Relation between effective stress and nominal stress

$$\hat{\sigma} = D(\eta)\sigma \tag{4.1}$$

2. Diagonal second-order tensor composed by damage variables

$$D = diag[\frac{1}{(1-\eta_{xx})}, \frac{1}{(1-\eta_{yy})}, \frac{1}{(1-\eta_{zz})}, \frac{1}{(1-\eta_{xy})}, \frac{1}{(1-\eta_{yz})}, \frac{1}{(1-\eta_{zx})}] \tag{4.2}$$

3. Effective stress taking into account the strain equivalence principle

$$\hat{\sigma} = C_o \epsilon \tag{4.3}$$

4. Stress-strain relation

$$\sigma = D^{-1}(\eta) C_o \epsilon = C(\eta)\epsilon \tag{4.4}$$

5. Normalized energy release rates

$$\bar{Y}_{ij}(\sigma,\eta) = \begin{cases} \frac{\sigma_{ii}^2}{2E(1-\eta^2)X} & \text{if} \quad i = j \, and \, \sigma_{ii} \geq 0 \\ \\ \frac{\sigma_{ij}^2}{2G(1-\eta^2)S} & \text{if} \quad i \neq j \end{cases} \tag{4.5}$$

6. Stress damage surfaces

$$f^{\xi}(\sigma,\eta) = \sigma^T F^{\xi}(\eta)\sigma - 1 \qquad \xi = 1, 2, \ldots, m \tag{4.6}$$

7. Strain damage surfaces

$$g^{\xi}(\epsilon,\eta) = \epsilon^T G^{\xi}(\eta)\epsilon - 1 \qquad \xi = 1, 2, \ldots, m \tag{4.7}$$

8. Damage rule

$$\dot{\eta} = \sum_{\xi=1}^{m} \Phi^{\xi} v^{\xi} \tag{4.8}$$

9. Damage directors

$$v^{(1)} = [\lambda_{xx}^{(1)} \; 0 \; 0 \; \lambda_{xy}^{(1)} \; 0 \; \lambda_{zx}^{(1)}]^T \tag{4.9}$$

10. Definition of growth functions Φ^{ξ}

$$\Phi^{\xi} = \langle \nabla_{\epsilon} g^{\xi}, \dot{\epsilon} \rangle_{+} \tag{4.10}$$

Firstly, for clarity in the notation, it has to be noted that bold characters denote tensor and vector variables. In Eq.[4.1], $D(\eta)$ is the second-order diagonal tensor formed by the internal damage variables, η_{ij}, and $\sigma = [\sigma_x, \sigma_y, \sigma_z, \sigma_{xy}, \sigma_{yz}, \sigma_{zx}]^T$ is the nominal stress. These variables, η_{ij}, are responsible of the stiffness degradation due to the different damage modes in the composite material: fibre rupture, fibre buckling or kinking, matrix cracking and matrix crushing.

The damage tensor D is built as a diagonal tensor and contains all the damage variables associated with each damage mode, Eq.[4.2]. The effective stress tensor $\hat{\sigma}$, which takes into account the strain equivalence principle [79], can be expressed as in Eq.[4.3]. C_0 is the second-order constitutive tensor containing all stiffness components of the undamaged material and ϵ is the strain tensor. The stress-strain relation is given in Eq.[4.4] where $C(\eta)$ is the non-symmetric damaged stiffness tensor.

In terms of stress, according to the plasticity theory, the first question that must be answered is how the stress state in the material is. For this purpose, stress damage surfaces associated with each damage mode ξ are defined. Then, the undamaged domain is delimited by the stress damage surfaces. These stress damage surfaces are built taking into account the so-called normalized energy release rates (NERR) given by Eq.[4.5]. Every damage mode is characterized by a certain combination of these NERRs where E is the Young modulus, G is the in-plane shear modulus, X is the tensile strength and S the shear strength. In the composite here considered, i and j directions correspond with the x and y axis. The form of the stress damage surfaces is presented in Eq.[4.6]. In this equation, $F^{\xi}(\eta)$ is a second-order tensor associated to the damage mode ξ and m is the total number of damage modes modelled.

Once f^{ξ} is obtained, the strain damage surfaces g^{ξ} can be calculated by mapping into the strain space given by Eq.[4.7]. For computing the damage, the damage variables give a value of the damage that is occurring in the structure due to the different damage modes. The time variation of damage variables is given by the damage rule expressed by Eq.[4.8]. In that equation, Φ^{ξ} are growth functions and v^{ξ} are the unitary damage directors. The modelling of the damage directors is made according to the degradation of stiffness due to a damage mode. For instance, fiber rupture $v^{(1)}$ affects to the

degradation in direction xx, xy and zx (see Eq[4.9]). Thus, following the references [38] and [37] the weights λ_{ij} represent the influence of the damage modes in the computation of a certain damage mode. In previous research, these weights λ_{ij} were defined in a qualitative manner. In this work, it is proposed a new relation based on the volume fraction and the properties of both components of the material (fibre and matrix). By means of this new relation, a realistic amount of energy is dissipated during damage.

The mathematical definition of the growth functions Φ^{ξ} for each damage mode ξ can be made according to Eq.[4.10]. In this equation the growth functions Φ^{ξ} are defined as the non-negative inner product between the strain gradient of the damage surface in the strain space, $\nabla_{\epsilon} \cdot g^{\xi}$, and the strain rate $\dot{\epsilon}$. Note that if the strain increment vector is pointing to the interior of the damage surface, for a determined damage mode, then no progression of such damage mode occurs. A flowchart of the explicit time integration [20] is presented in Figure 4.1 and the constitutive law subroutine in which the progressive damage model is implemented.

4.3 Mixed-mode damage analysis

4.3.1 Numerical model

In this Section, the CGRP cruciform structure presented in Section (see Figure 3.1) is considered for the current analysis. It is important to notice that the cruciform geometries under analysis are subjected to different biaxial loadings. Those loadings provoked the appearance of a macro-crack throughout the central zone of the cruciform specimen. Then, for geometry A the loading which will lead to failure through the diagonal of its central zone is 1/1, which means that the same load is applied in horizontal and vertical arms. In geometry B, the loading condition is 1.5/1, the first term means that more load is applied in horizontal arm (50% more) compared to the vertical one. Geometry C has a loading case 0.5/1, so that, half of the vertical load is applied in the horizontal arm.

The composite under analysis presents a quasi-isotropic behaviour and homogeneity through the thickness as has been demonstrated experimentally in [126][127]. Based on this fact, computationally, the composite is treated as an isotropic and homogeneous material.

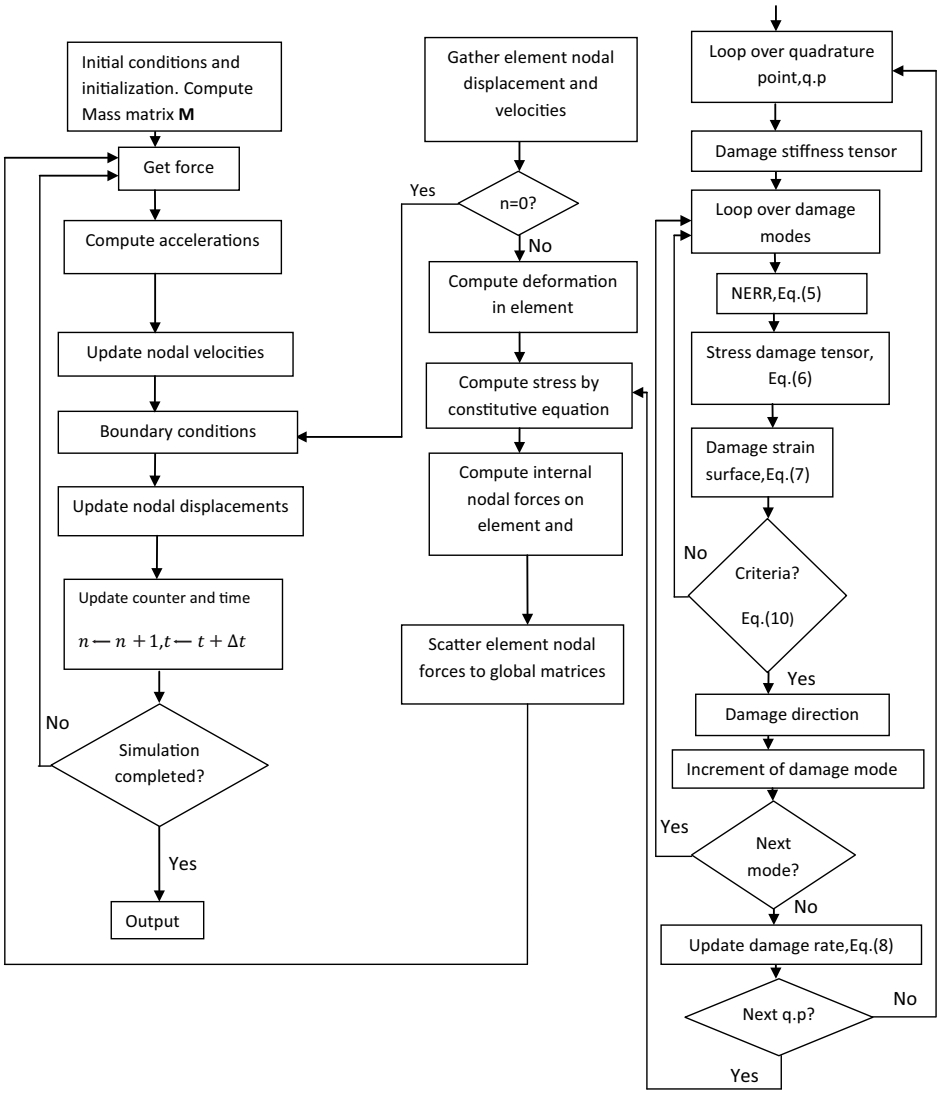

Figure 4.1: Flowchart of the explicit time integration of a Lagrangian mesh that is used for solving the momentum equation (left side). The constitutive damage law subroutine (right part) for calculating in each quadratic point the damage progression.

In this analysis, an explicit central-difference time integration rule is considered with an automatic time increment. The numerical simulations have been performed by means of the finite element (FE) software ABAQUS [60]. For provoking failure in the structures, a displacement in the tip of the arms is defined. This displacement is applied incrementally and quasi-statically. For the FE discretization, two different mesh regions are distinguished with different element size in the structure (see Figure

4.2). The first one, it is in the central zone with a 0.4 mm size (zone of interest) and the second one defined in the arms with 1.4 mm size. The finite element used is an eight noded hexaedra element with reduced integration. Hourglassing control has been considered in order to avoid spurious deformation in the FE mesh. A nonlinear explicit dynamic analysis has been performed. A 3D model is studied, considering a 1/8 of the structure due to the symmetry of the problem and also in order to save computational costs considering symmetry boundary conditions.

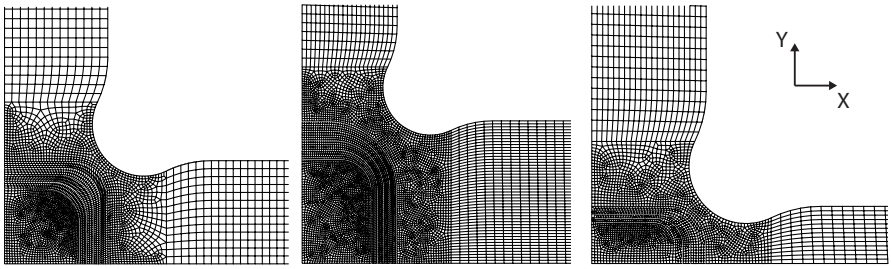

Figure 4.2: FE mesh of 1/8 of the geometries A, B and C respectively. Notice a finer mesh in the central zone (0.4 mm) than in the arms (1.4 mm)

A damage variable η is defined in order to model damage in the cruciform structure. This damage variable degrades equally the x and y components of the stress tensor i.e. σ_x and σ_y, due to the quasi-isotropic behaviour of the composite under analysis. The damage rate considers the influence of fibre rupture and matrix cracking as presented in Eq.[4.11]:

$$\dot{\eta} = \sum \Phi^{\xi} v^{\xi} = \lambda_f \Phi^f + \lambda_m \Phi^m \tag{4.11}$$

Where $\dot{\eta}$ represents the damage variable rate. Note that, this variable is defined as a linear combination of damage growth for fibre rupture Φ^f and matrix cracking Φ^m. So, the increment of damage is a contribution of the fibre and matrix breakage. λ_f and λ_m quantify the influence of fibre rupture and matrix cracking respectively into the damage growth.

The definition of λ_f and λ_m is based on the rule of mixtures within the two components of the CGRP composite: fibre and matrix. The percentage in volume of the fibre is $v_{fibre} = 20$ % , and its elastic modulus is $E_{fibre} = 70\,GPa$. The remaining percentage of volume corresponds to the matrix ($v_{matrix} = 80\%$) and its elastic modulus is $E_{matrix} = 2\,GPa$. Tacking into account those material properties, the stiffness and the

percentage of volume of the fibres is described as a function of the matrix properties in Eq.[4.12] and Eq.[4.13].

$$v_{fibre} = \frac{1}{4}\, v_{matrix} \tag{4.12}$$

$$E_{fibre} = 35\, E_{matrix} \tag{4.13}$$

Based on the above equations and considering the stiffness and the percentage of volume of each component separately it is possible to define two ratios denoted as α and β for fibre and matrix respectively. Those ratios are defined as:

$$\alpha = \frac{3}{8}\, E_{fibre}\, v_{fibre} \tag{4.14}$$

$$\beta = E_{matrix}\, v_{matrix} \tag{4.15}$$

Notice that the term $\frac{3}{8}$ in equation 4.14 has been considered to address the randomness of fibres throughout the CGRP composite [75]. Finally, the values of λ_f and λ_m are described as follows:

$$\lambda_f = \frac{\alpha}{\sqrt{\alpha^2 + \beta^2}} = 0.96 \tag{4.16}$$

$$\lambda_m = \frac{\beta}{\sqrt{\alpha^2 + \beta^2}} = 0.29 \tag{4.17}$$

By means of Eq.[4.16] and Eq.[4.17], a more physical definition has been considered for λ_f and λ_m. As shown in Eq.[4.11], those scalar variables affect the computation of damage. In particular, λ_f and λ_m control the amount of energy dissipated during strain-softening i.e. the area under the curve stress-strain. The goodness of the proposed definition is verified in the next Section where a realistic value of energy is dissipated during simulations.

The PDM here adopted is a local damage model in which damage variables depend on the strain state of the element under consideration and the numerical simulations exhibit mesh dependency. Therefore, it has been noticed that during mesh refinement the energy dissipated tends to zero when damage occurs. To overcome this limitation, some authors had considered different approaches to deal with mesh dependency. For example, regularisation techniques [40], nonlocal damage models (the damage variables

depend on the strain state of the neighbourhood giving a characteristic length [120]) or the crack band model [12]. Using this last approach particularly, the strength limit is not kept constant in order to preserve the fracture energy constant. In this work, this strategy is not considered in order to preserve the material strength during simulations and therefore give a more realistic model. Hence, for this application, the strategy followed is based on preserve the energy dissipated during the fracture process in order to provide realistic results without changes in the material strength.

The energy released during an uniaxial test has been compared with the computational energy released in the rounded zone of the cruciform where the macro-crack is initiated. The value of energy estimated for the uniaxial test is $G_I^C = 6210Pa$ [125], being mode I the dominant fracture mode. A fragile fracture process has been produced, considering that the strain at the moment of failure ϵ_f is considered 1% higher that the yield strain $\epsilon_Y = 0.0138$. In the other hand, the expected strain-softening provided by simulations reached ultimate failure when the failure strain is 8% higher than yield strain ϵ_Y. This deviation of energy released compared with mode I (uniaxial test) is attributed to the fact that in the rounded zone of the specimen a notable shear stress component is observed during loading [128] that consequently induces mode II of failure.

During simulations, an initiation criterion based on the maximum principal stress σ_{max} into CGRP cruciform is defined. Consequently, damage is initiated once the maximum principal stress σ_{max} within the model reached the material strength i.e. 90 MPa. For the post-pick behaviour in the constitutive model, a damage variable is defined considering the influence of matrix cracking and fibre rupture. This consideration is realistic because the fibres are randomly embedded into the matrix so both damage processes occurred at the same time and aim failure.

$$F^{damage} = \begin{bmatrix} \frac{1}{(1-\eta_x^2)X^2} & 0 & 0 & 0 & 0 & 0 \\ 0 & \frac{1}{(1-\eta_y^2)X^2} & 0 & 0 & 0 & 0 \\ 0 & 0 & 0 & 0 & 0 & 0 \\ 0 & 0 & 0 & 0 & 0 & 0 \\ 0 & 0 & 0 & 0 & 0 & 0 \\ 0 & 0 & 0 & 0 & 0 & 0 \end{bmatrix} \tag{4.18}$$

A second-order tensor is defined into the PDM. The components of this second-order tensor are in-plane components. F^{damage} corresponds to the damage tensor associated to the material degradation of the composite. By mapping those tensors into the stress space it is possible to define the stress damage curve, $f^{damage}(\sigma, \eta) = \sigma^T F^1(\eta)\sigma - 1$. This stress curve defines the undamaged domain of the CGRP composite. Once damage grows this curve is degraded reducing the undamaged domain because of the material degradation. This behaviour is illustrated in Figure 4.3. Looking at that figure, when the material is undamaged i.e. $\eta = 0$, the undamaged domain is defined by the solid line and once the damage is developed (dashed line in Figure 4.3), for instance $\eta = 0.6$, the undamaged domain is reduced.

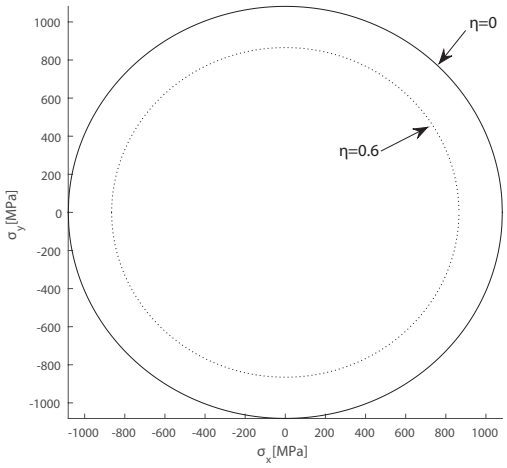

Figure 4.3: In-plane stress space curves for the undamaged CGRP material, η=0, and the damaged material, η=0.6.

4.4 Results and validation

In this section, the results from simulations are compared with the experimental tests in order to validate the proposed numerical approach for a biaxial loading context. Several simulations (Table 4.1) have been performed with three different geometries and loading conditions. Experimental results for geometry A are presented in Figure 4.4. In that figure, the macro-crack is initiated in the rounded zone and propagated throughout the central zone. The same pattern of failure is observed during experiments for geometries

B and C under its corresponding biaxial loading cases shown on Table 4.1. The CGRP composite owns random fibre distribution within the matrix so any crack observed will consequently provoke matrix cracking and fibre rupture. Due to the manufacture process, the composite is statistically homogeneous through the thickness as depicted on Figure 4.4. Hence, there is not an interface macroscopically between layers. The case under analysis serves to emphasise the fact that degradation in a certain direction is influenced by multi mixed-mode damage. In the cruciform specimen, the fact that matrix cracking is developed makes fibre rupture developed as well, and viceversa. Thus, the application of the current model it is well fundamented because the PDM implemented considers the influence between different damage modes.

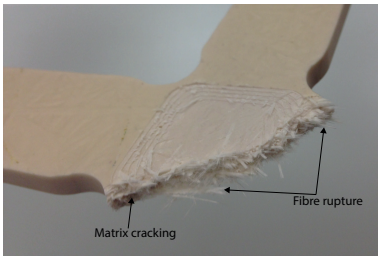

Figure 4.4: Experimental modes of failure observed into the cruciform when the macro-crack is fully developed.

Experimentally, for the cruciform specimen A, a loading case 1/1 yields to an adequate failure across the central zone and the crack is initiated in the rounded zone. Considering the last fact, the PDM was embedded in geometry A. Hence, in Figure 4.5 (b), it is illustrated the map of damage predicted by the numerical approach. In that Figure, a damage variable called SDV1 is defined. It is important to notice that this variable is ranged between 0 (undamaged material) and 1 (total failure) and represents the percentage of damage as a contribution of fibre and matrix breakage. The localization of damage in geometry A is properly addressed by the PDM and higher values of damage are found in the rounded zone as depicted. In Figure 4.5 (a), the map of principal stresses is presented. This map of stresses corresponds with the initiation of degradation in the area of stress concentration.

It has to be highlighted that experimentally for a loading case different to 1/1 in geometry A failure appears in the arm with bigger load applied so non-adequate failure is achieved. This fact is predicted by the proposed technique and it is shown in Figure

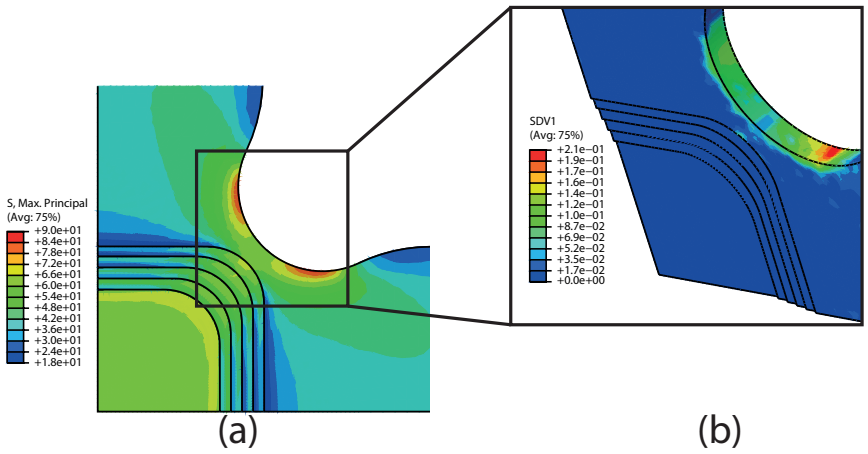

Figure 4.5: (a) Maximum principal stresses map for geometry A under loading case 1/1 (units are in MPa) and (b) Map of damage in geometry A under loading 1/1.

4.6 (b). In that figure, higher values of damage are located in the vertical arm where double load is applied compared to the load applied in the horizontal arm.

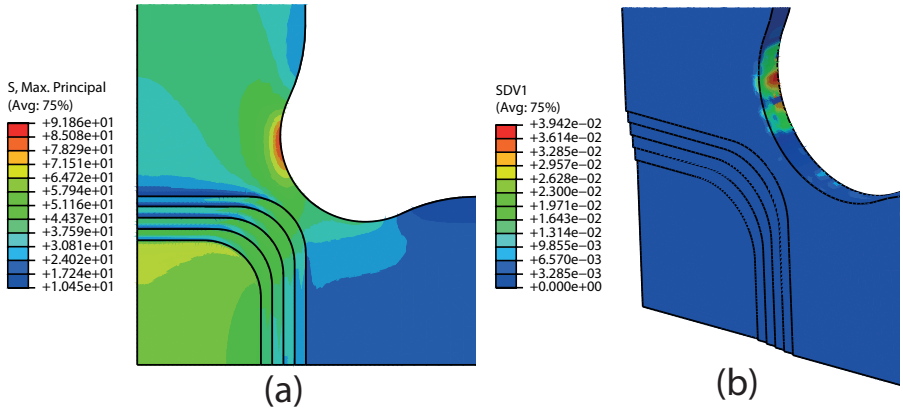

Figure 4.6: (a) Maximum principal stress map for geometry A under a loading cases 1/2 (units are in MPa) and (b) Map of damage in geometry A under 1/2 loading.

The PDM was also implemented in geometries B and C. In these geometries the biaxial loading case considered are 1.5/1 and 0.5/1 respectively. In Figure 4.7 (b) and Figure 4.8 (b), the corresponding map of damage for geometries B and C are addressed. For both geometries, the localization of the damage is properly localized when comparing with experimental tests. Hence, the crack is initiated in the rounded zone where the PDM predicts higher damage for all geometries.

Figures	Figure 4.6	Figure 4.5	Figure 4.7	Figure 4.8
Geometry	A	A	B	C
Loading case	1/2	1/1	1.5/1	0.5/1

Table 4.1: Simulations parameters

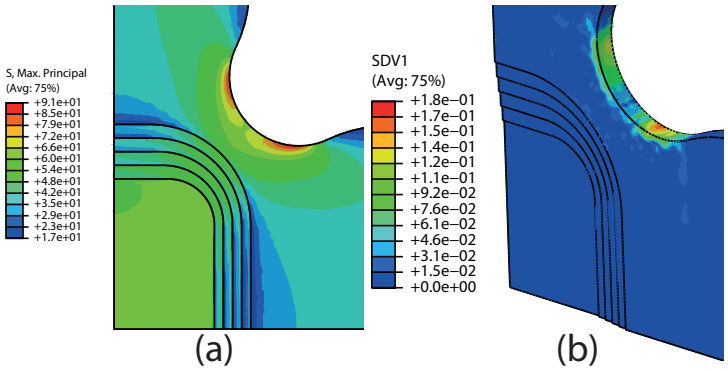

Figure 4.7: (a) Maximum principal stress map for geometry B under a loading cases 1.5/1 (units are in MPa) and (b) Map of damage in geometry B under loading 1.5/1.

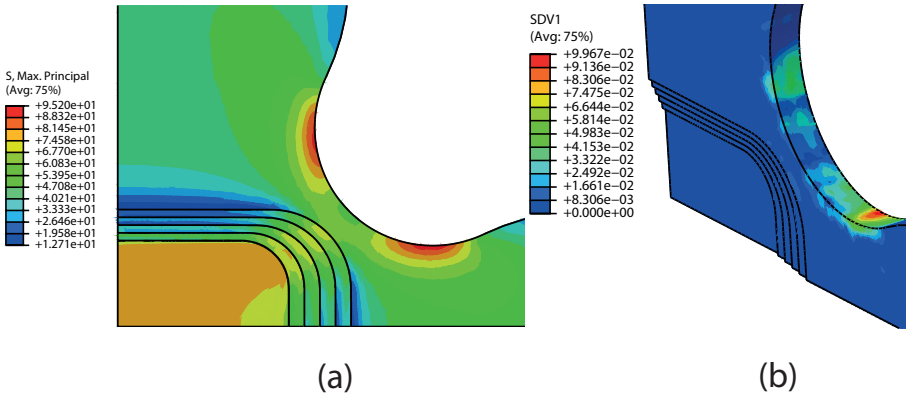

Figure 4.8: (a) Maximum principal stress map for geometry C under a loading cases 0.5/1 (units are in MPa) and (b) Map of damage in geometry C under 0.5/1 loading.

4.5 Conclusions

The implementation of a PDM within a cruciform structure has been addressed. Mixed damage modes have been considered being matrix cracking and fibre rupture the agents that provoke the macro-crack initiation in the rounded zone of the cruciform. Special

care has been taken into account in order to solve the mesh dependency issue and provide realistic results during simulations. Thus, the PDM has been able to:

- Accurate localise the damage compared with experimental tests. This localization depends on the two damage modes (fibre rupture and matrix cracking) that are involved on the failure.

- Address the initiation of damage based on a maximum principal stress criterion. Then, when the value of maximum principal stresses in the rounded zone was 90 MPa the damage process started. This fact was observed in experimental observations.

Based on the computational results obtained and the comparison with experimental tests, it is possible to conclude that the PDM successfully predicts damage initiation in complex loading cases such as biaxial. Additionally, during the damage process, a realistic amount of energy is dissipated. The strategy adopted takes material properties of the composite such as the stiffness/volume ratio.

5

An XFEM approach for simulating cracks in ACM

5.1 Introduction

In previous chapters, two different formulations for representing damage and fracture were adopted: a discontinuous approach i.e. 2D/3D XFEM (Chapter 3) and a continuous approach (Chapter 4) i.e. 3D PDM. For the implementation of these numerical tools, an implicit (Newton method) and explicit (central difference method) FE solver were used for obtaining the main unknowns i.e. the nodal displacements. Those algorithms were embedded into the commercial FE code ABAQUS and new capabilities were added by means of the implementation of user-subroutines.
The objective of this chapter is to propose a solution for the limitation found in chapter 2 with PDM. The idea is to develop an approach based on XFEM for solving the limitation inherent in PDM. In the author knowledge, there is not a commercial code that is capable of simulating cracks in ACM using XFEM. Hence, there is a need to develop an *in-house* code that allows the full control of the formulation and therefore the possibility of simulate cracks with XFEM in ACM.

Initially, the FE code needs to be validated. Hence, in Section 5.2, the main formulation written in MATLAB environment, so-called Main Updated Lagrangian Explicit ($MULE$), is explained for a better understanding of the code. Initially, MULE was coded by Dr. Curiel-Sosa and it was formulated for solving static and dynamic two-

dimensional problems. In Section 5.3, MULE has been improved by the author, adding capabilities such as the simulation of damage in advanced composite materials. Taking into account several functions of MULE and adding new ones, in Section 5.4, the author presents an approach for simulating cracks in the framework of XFEM is developed. This explicit XFEM code, so called explicit eXtended Finite Element Method (X^2FEM), is capable of solving static and dynamic problems. Initially, the proposed approach has been validated by using tests which theoretical solutions were known. Once the code was validated, the proposed approach has been used for solving the limitation found in chapter 2.

5.2 Main explicit Finite element program

5.2.1 Spatially FE approximation and time-discretisation by central difference method

The CDM is the solution procedure considered for the construction of MULE. This method is characterised for its robustness and accuracy. However, it is conditionally stable. This stability condition is called the Courant condition [32] and it is presented in Equation 5.1. Then, during simulations, if the time increment is bigger than the critical time step, instabilities are present and divergence of the numerical technique is possible.

$$\Delta t_c \leq \frac{2}{\omega_{max}} \tag{5.1}$$

In Equation 5.1, ω_{max} denotes the maximum frequency of the mesh i.e. $\omega_{max} = max_{\forall(e)}\{\omega^e_{max}\}$ obtained form the eigenvalue problem given by:

$$det(\mathbb{K} - \omega^2\mathbb{M}) = 0 \tag{5.2}$$

where $\mathbb{K}$ and $\mathbb{M}$ are the stiffness matrix and the mass matrix of the whole mesh, respectively. The CDM is developed from the central difference formulas of velocity and acceleration. Therefore, the time increments are defined as follows:

$$\Delta t^{n+\frac{1}{2}} = t^{n+1} - t^n, \quad t^{n+\frac{1}{2}} = \frac{1}{2}(t^{n+1} - t^n), \quad \Delta t^n = t^{n+\frac{1}{2}} - t^{n-\frac{1}{2}} \tag{5.3}$$

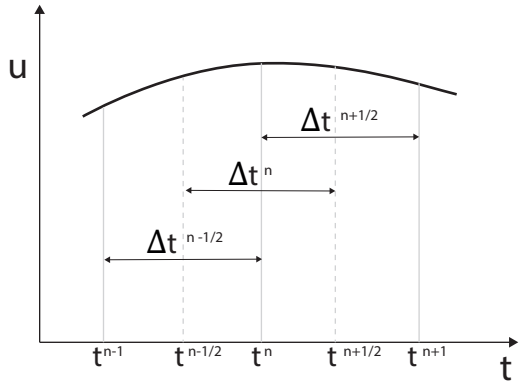

Figure 5.1: Discretisation used in central difference scheme.

The definition of those time increments is better understood referring to Figure 5.1. According to this graph, the central difference formula for velocity at the mid-step, $\dot{u}^{n+\frac{1}{2}}$ given by Eq.(5.4) and acceleration for time step n, $\ddot{u}^n$ given by Eq.(5.5) are defined as,

$$\dot{u}^{n+\frac{1}{2}} = \frac{u^{n+1} - u^n}{t^{n+1} - t^n} = \frac{1}{\Delta t^{n+\frac{1}{2}}}(u^{n+1} - u^n) \rightarrow u^{n+1} = u^n + \Delta t^{n+\frac{1}{2}} \dot{u}^{n+\frac{1}{2}} \tag{5.4}$$

$$\ddot{u}^n = a^n = \frac{v^{n+\frac{1}{2}} - v^{n-\frac{1}{2}}}{t^{n+\frac{1}{2}} - t^{n-\frac{1}{2}}}) \rightarrow v^{n+\frac{1}{2}} = v^{n-\frac{1}{2}} + \Delta t^n a^n \tag{5.5}$$

Taking into account the time integration in the equation of motion for a given time step n, it is derived from the following equation:

$$Ma^n = f_{ext}^n - f_{int}^n \tag{5.6}$$

where f_{ext}^n and f_{int}^n are the external and internal nodal forces respectively for a time step n. The external and internal forces are functions of the time and the displacement.

The main steps considered for the implementation of the central difference method [16] are provided in Box I. These steps point out the flow followed by the algorithm coded in MATLAB in order to obtain the main unknowns i.e. the nodal displacements u. The nodal displacements and nodal forces of an element e are denoted by u_e and f_e, respectively. The element type considered is a four-node element with a linear displacement field and nodes are numbered counterclockwise. For an element e, the nodal displacements are written as $u_e = [u_{x1}\, u_{y1}\, u_{x2}\, u_{y2}\, u_{x3}\, u_{y3}\, u_{x4}\, u_{y4}]^T$ and nodal

forces as $f_e = [f_{x1}\, f_{y1}\, f_{x2}\, f_{y2}\, f_{x3}\, f_{y3}\, f_{x4}\, f_{y4}]^T$ being two the number of DOF per node. The current explicit FE code is formulated mainly for solving linear and non-linear static and dynamic problems. The static solution requires an additional term included in the total force vector $f^n = f^n_{ext} - f^n_{int}$, this term is a linear viscous force defined as $f^n_{damp} = C_{damp} v^n$ where C^{damp} is the diagonal damping matrix considered in this case proportional to the mass matrix $C^{damp} = \alpha M$ and v^n is the nodal velocity. The total force is re-defined as $f^n = f^n_{ext} - f^n_{int} - C_{damp} v^n$. In Box I the velocity update is broken into two substeps for enabling the energy balance at integer time steps [16]. Thus, the discretised equation of motion is defined as:

$$Ma^n + f^n_{damp} + f^n_{int} = f^n_{ext} \tag{5.7}$$

As shown in Box I, the main part of the algorithm is the calculation of the nodal internal forces. For a more detailed understanding of the central difference method the author recommends consulting Belytschko et al. [16].

(a) Defined initial conditions such as:

Initial velocity $\dot{u_o}$ and displacement u_o

Set counter $n = 0$ and the initial time $t_o = 0$

Input: nodal coordinates X_o, topology matrix, material properties, constraints, load, damping parameter.
(b) Compute the diagonal mass matrix M.
(c) Loop over time steps:
(c.1) Internal force f_{int}^n at t_n for all DOF:
(c.1.1) Loop over elements e
(c.1.2) Loop over quadrature points
(c.1.2.1) Compute strain : $\epsilon^n = B \cdot u^n$
(c.1.2.2) Compute stress σ using the constitutive law: $\sigma^n = D \cdot \epsilon^n$
(c.1.2.3) Compute internal forces: $f_{int,e}^n = \int_\Omega B^T \sigma d\Omega$
END quadrature point loop
(c.1.3) Compute the global internal force vector for an element (e), $f_{int,(e)}^n$
END loop over elements
(c.2) Compute the global external force vector: f_{ext}^n
(c.3) Compute the global force vector: $f^n = f_{ext}^n - f_{int}^n$
(c.4) Compute accelerations from considering the time integration in the equation of motion: $a^n = M^{-1}(f^n - C^{damp} v^{n-\frac{1}{2}})$
(c.5) Time update: t^{n+1}, $t^{n+\frac{1}{2}}$
(c.6) 1^{st} partial update of nodal velocities: $v^{n+\frac{1}{2}}$
(c.7) Boundary conditions
(c.8) Update nodal displacement: $u^{n+1} = u^n + \Delta t^{n+\frac{1}{2}} v^{n+\frac{1}{2}}$
(c.9) Get internal force $f^{int,n+1}$ following (c.1)
(c.10) Compute a^{n+1}
(c.11) 2^{nd} partial update of nodel velocities: v^{n+1}
Update counter: n ← n+1
END loop of time steps

5.3 Improvements in the initial *in-house* code

The previous section introduced the main scheme of MULE. In this section, several improvements in this code are presented, for instance, the possibility of elastic analysis of composite laminates as well as 2D damage analysis of composite. Apart from that, the simulation of material non-linearities is addressed considering a PDM that predicts the different damage modes. The PDM considered is the PDM proposed by Curiel-Sosa et al. reduced to a 2D context.

5.3.1 Numerical implementation of a 2D Progressive damage model for fibre-reinforced composites

The objective of this section is the implementation of the PDM initially proposed by Curiel-Sosa et al. in the *in-house* code developed in MATLAB. By means of this implementation, the *in-house* code will allow the analysis of damage in problems where a composite is subjected to a certain load scenario. For the numerical implementation, the formulation of the PDM is reduced from a 3D to a 2D context. Therefore, two different damage variables ω_1 and ω_2 are included in the constitutive relation. The purpose of the internal damage variables is to degrade gradually the stiffness matrix. Their values are ranged between zero (undamaged material) and one (total failure). Particularly, ω_1 takes into account the degradation in the direction of the fibres for tensile loading (fibre rupture) and compressive loading (fibre buckling) and ω_2 takes into account the first transverse direction damage for tensile loading (matrix cracking) and compressive loading (matrix crushing). In this model, the relation between effective stress, $\hat{\sigma}$, and the nominal stress, σ is defined as $\hat{\sigma} = L\sigma$ where L is the diagonal damage operator:

$$L = \begin{bmatrix} \frac{1}{1-\omega_1} & 0 & 0 \\ 0 & \frac{1}{1-\omega_2} & 0 \\ 0 & 0 & 0 \end{bmatrix} \tag{5.8}$$

The 3D formulation of the initial PDM is presented in Chapter 4 and its reduction to 2D is needed to enable it to be coupled with the 2D *in-house* code. Hence, plane stress conditions are assumed. The simplified stress tensor is defined as $\sigma = [\sigma_1 \sigma_2 \sigma_{12}]^T$ according to the local coordinate system $\{123\}$ defined in Figure 5.2.

For the implementation of the PDM within the explicit FE code, the stiffness of the material must be degraded in order to address the lost load carrying capability of the composite. In this code, the subroutine responsible for the implementation of the PDM is described in Appendix B. This subroutine, so-called *PDM*, takes as an input arguments the element strain *epse*, the damage tensor *w*, the time increment *dt*, the angle of the fibres *teta* and the iteration number *it*. The element strain *epse* is rotated into the local coordinate system at an angle *teta* by means of the function *rotate_ strain*. Since it is a material non-linearity, it requires an update of stress and stiffness along the procedure such as: $\epsilon \longrightarrow \hat{\epsilon} \longrightarrow \hat{\sigma}\ \hat{D} \longrightarrow \sigma\ D$

Along the subroutine, once the initiation criteria is satisfied, the values of the damage variables w are different than zero and then the damaged tensor Dw (output of the subroutine) degrades the element stiffness according to the evolution of the damage variable tensor w.

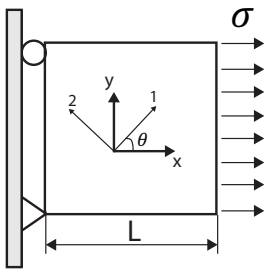

Figure 5.2: Single element test.

The PDM within the *in-house* code is tested for a single element test (see Figure 5.2). The material chosen for the test is a carbon fibre reinforced AS4/3501 and its properties are presented in Table 5.1. The element type considered is a four node element with two DOF per node, full integration and assuming plane stress. A non-linear static analysis is carried out. The load σ is applied incrementally in the x-direction in order to keep inertia and damping forces small from the beginning. Hence, the non-linear problem is converted in a succession of small linear analysis. To validate this example, the computational stress and strain at failure are compared with the corresponding experimental values for a single lamina extracted from Soden et al. [134]. Two different fibre orientations are considered with respect to the x-axis (0 and 90 degrees). For $\theta = 0$ (see Figure 5.2), the fibres are aligned with the x-axis, then, when loading in the fibre direction, the damage mode expected experimentally is fibre rupture. The results obtained from the model are presented on Figure 5.3. In Figure 5.3 (a), the stress in x-direction σ_x is plotted against the strain ϵ_x. In this figure, the constitutive relation of the model for fibre rupture is observed. Thus, initially a linear elastic behaviour is observed and once the initiation criteria based on the longitudinal strength is satisfied, the degradation process begins. In Figure 5.3 (b), it is observed that the only damage mode that appears is fibre rupture once the initiation criteria is reached. The experimental failure strength in fibre direction is 1950 MPa which is equal to the computational value obtained from the model. The experimental yielding strain is 1.38 % and its corresponding computational value is 1.54 %.

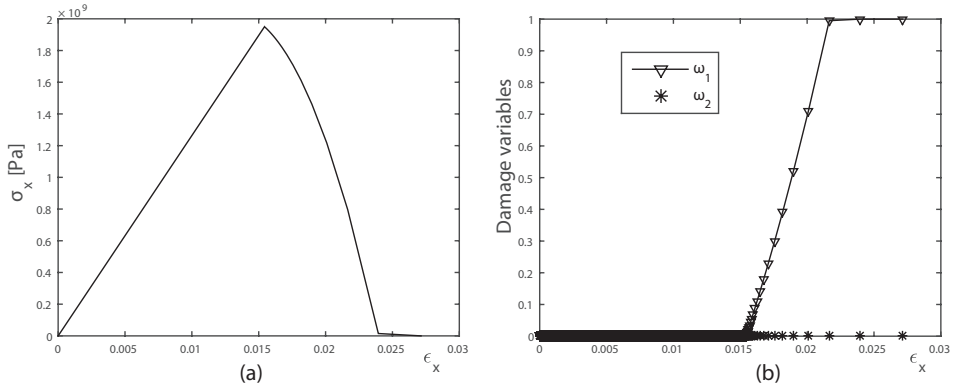

Figure 5.3: (a) Stess σ_x versus strain ϵ_x in x-direction and (b) damage variables versus ϵ_x for a single element when fibres form zero degrees with the x-axis.

In order to check the predictability of the code when loading perpendicular to the fibres, the fibres are rotated 90 degrees with respect to the x-axis i.e. $\theta = 90$. Therefore, the experimental damage mode expected is matrix cracking. This fact is addressed by the 2D PDM. In Figure 5.4 (a), the stress and strain in x-direction is plotted being the experimental and computational stress at yielding equal to 48 MPa. The experimental yield strain was 0.436 % and the computational value was 0.435 %, hence, the relative error for both strains is 0.2 %, which shows a good agreement. In Figure 5.4 (b), the value of the damage variables during simulation are depicted. It is observed that the only damage mode is matrix cracking, which corresponds with the experimental observations.

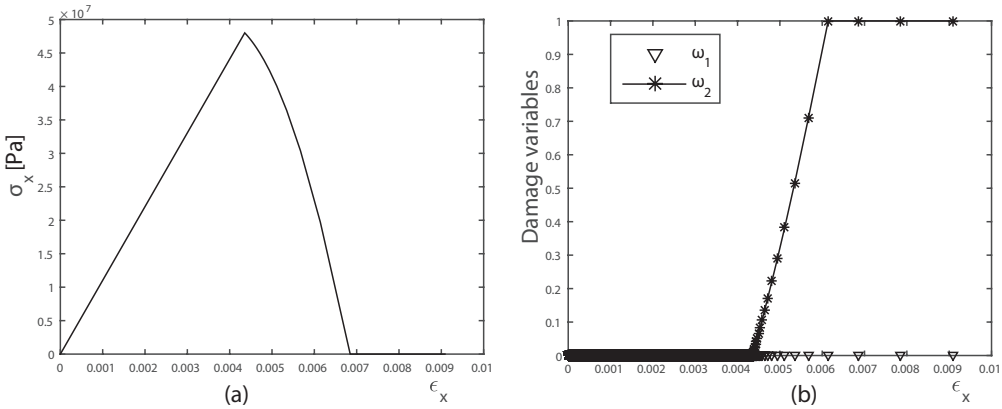

Figure 5.4: (a) Stress σ_x versus strain ϵ_x in x-direction and (b) damage variables versus ϵ_x for a single element when fibres form 90 degrees with the x-axis.

Elasticity	Ply strength
E_1 126 GPa	X_t 1950 MPa
E_2 11 GPa	X_c 1480 MPa
ν_{12} 0.28	Y_t 48 MPa
G_{12} 6.6 GPa	Y_c 200 MPa

Table 5.1: Mechanical properties of AS4/3501 lamina [134].

It is important to note that the numerical oscillations associated with the explicit FE code are avoided using an artificial damping so-called dynamics relaxation. Therefore, after an initial transient the solution converges to the quasi-static solution. It is concluded, that the values obtained for the ultimate tensile stress and failure strain are in reasonable agreement with the experimental results. During tensile loading in the fibre direction, the damage mode observed was fibre rupture whereas, for instance, matrix cracking was not computed. This shows the capacity of the PDM to properly address the corresponding damage modes depending on the stress state. On the other hand, when the angle between the fibres and the x-direction forms 90 degrees, the damage mode expected is matrix cracking and the ultimate tensile stress and failure strain agree with the experimental results for matrix failure i.e. first transverse direction.

5.4 New dynamic explicit XFEM approach for fixed cracks

5.4.1 Introduction

In the previous section, several improvements in the main FE code were added, for instance, the implementation of a 2D PDM embedded in the main platform. It is well known that the FEM is a useful technique for modelling many interesting phenomena [103]. For instance, a linear stress analysis on a component under a certain load state may be simulated with few complications. However, when dealing with simulation of moving cracks throughout a structure a limitation is noticed using FEM. Basically, the FE mesh has to adapt to the topology of the moving discontinuity. Therefore, the mesh needs to be updated at each time step, which is computationally expensive. Thus, with the motivation of adapting the FEM to fracture mechanics, a numerical method

for modelling cracks independently of the mesh was introduced in 1999, the so-called XFEM [17] [95]. This method is inspired by the partition of unity concept initially proposed by Babuska and Melenk [10]. The development of numerical techniques for modelling fracture and its implementation in numerical codes is a topic in ongoing research. This interest is attributed to the desire to address the behaviour of structures whilst a loading is acting. The motivation of this section is to present an approach for modelling fracture dealing with static and dynamic problems in the framework of XFEM.

A numerical approach to analyse stationary cracks in the framework of XFEM is presented. The approach proposed considers an explicit time integration scheme. In this case, the well-known CDM [101] is adopted for time discretisation. A diagonal mass matrix is used to solve the discrete momentum equation. The part of the mass matrix corresponding with the standard DOF u_I are lumped by direct mass lumping. However, lumping of the enriched DOF (a_I and b_I) is not straightforward and a limitation exists. The limitation was found by Belytschko et al. [15]. Basically, they found out that the critical time step of the explicit XFEM decreases notably as a discontinuity gets closer to nodes. To overcome this, Belytschko et al. [15] used an implicit integrator for the enriched element and explicit integrator for standard elements. Recently, other possible solutions for solving this limitation are based on using mass lumping strategies. In this work, using specific lumping techniques for enriched elements (see Section 5.4.2 for details) the diagonalised mass matrix is obtained avoiding the possibility of having a null critical time step.

5.4.2 Proposed damping strategy

Dynamic relaxation (DR) has been used in dynamic structural analysis for making static analysis possible. Therefore, the solution of the static problem is obtained as an ultimate state of the associated transient dynamic problem [117] i.e. the steady state response. Using an artificial damping technique, the static solution can be obtained by attenuation of the transient response [36].

In the context of FEM, the mass matrix can be calculated by means of different methods such as, for instance, direct mass lumping where the mass of an element is distributed over its nodes. After that, a diagonally lumped mass matrix is constructed.

However, when dealing with XFEM where extra DOF are considered in the displacement field, the mass matrix calculation is not trivial. In fact, it has been demonstrated that when a crack approaches a node, the critical time increment tends to zero what is crucial while working with an explicit solver such as the CDM. To overcome this limitation, some authors have considered different mass lumping strategies for the enriched part of the displacement approximation, e.g. Heaviside and crack tip enrichment functions.

In order to understand the influence of the position of the crack in the stable time increment calculation, the following example is considered; the geometry is depicted in Figure 5.5. In that figure, a 1D element is presented fractured by a crack. The length of the element is L, the distance between the discontinuity and the left node of the element is d. The 1D element presents a section A, young modulus E and density ρ. Initially, the standard finite elements (without discontinuity) are considered for the calculation of the stable time increment. In order to obtain its value, the stiffness and mass matrix of the 1D element with 2 DOF are needed . Hence, for the one-dimensional case [89], the stiffness matrix is defined as;

$$\mathbb{K}_{FE} = \frac{EA}{L}\begin{bmatrix} 1 & -1 \\ -1 & 1 \end{bmatrix} \tag{5.9}$$

By means of a mass lumping technique, the mass matrix for this element considering standard shape functions is;

$$\mathbb{M}_{FE} = \rho AL\begin{bmatrix} \frac{1}{2} & 0 \\ 0 & \frac{1}{2} \end{bmatrix} \tag{5.10}$$

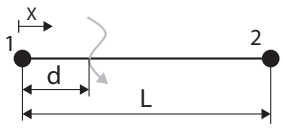

Figure 5.5: Cracked 1D element with a crack at distance d with respect to the left node.

Finally, solving the eigenvalue problem $det(\mathbb{K}^e - \omega^2\mathbb{M}^e) = 0$, the stable time increment for the 1D FE element is defined as:

$$\Delta t_c^{lumped} = \frac{2}{\omega_{max}} = L\sqrt{\frac{\rho}{E}} \tag{5.11}$$

Now, it is considered the discontinuity in the 1D element by using the XFEM displacement field defined as;

$$u = N_1 u_1 + N_2 u_2 + N_1 H b_1 + N_2 H b_2 \tag{5.12}$$

The first two terms represent the classical FE approximation and the last two are the enriched terms. The matrix form of the equation presented above is written as $u = Nu$ being $N = [N_1 \;\; N_2 \;\; N_1 H \;\; N_2 H]$ and $u = [u_1 \;\; u_2 \;\; b_1 \;\; b_2]$. The stiffness matrix can be calculated as $K = \int_{V_T} C B^T C dV$ where B is the matrix with the derivatives of the shape functions, C is the constitutive matrix and V_T is the total volume. Due to the discontinuity that includes the enriched shape functions H, the integration of the stiffness matrix must be subdivided into two sub domains. Then, in the left subdomain $0 \leq x \leq s$, $N_- = [N_1 \;\; N_2 \;\; -N_1 \;\; -N_2]$ and for the right subdomain $s \leq x \leq L$, $N_+ = [N_1 \;\; N_2 \;\; N_1 \;\; N_2]$. The stiffness matrix is calculated as $K = \int_0^s B_-^T E A B_- dx + \int_s^L B_+^T E A B_+ dx$. Finally, the stiffness matrix is obtained as a function of the distance between the left edge and the crack located at the element;

$$\mathbb{K}_{XFEM} = \frac{EA}{L} \begin{bmatrix} 1 & -1 & 1-2d & 2d-1 \\ -1 & 1 & 2d-1 & 1-2d \\ 1-2d & 2d-1 & 1 & -1 \\ 2d-1 & 1-2d & -1 & 1 \end{bmatrix} \tag{5.13}$$

In order to build the mass matrix for the elements fractured by the crack, the lumping technique proposed by Menouillard et al. [89] is adopted and it is defined as follows;

$$m_{diag}^{(e)} = \frac{\rho}{n_{nodes}} \int_{\Omega_{(e)}} H^2(x) d\Omega \quad \rightarrow \quad \mathbb{M}_{XFEM} = \frac{\rho A L}{2} \begin{bmatrix} 1 & 0 & 0 & 0 \\ 0 & 1 & 0 & 0 \\ 0 & 0 & 1 & 0 \\ 0 & 0 & 0 & 1 \end{bmatrix} \tag{5.14}$$

where $\Omega_{(e)}$ is the element being considered, $m^{(e)}$ corresponds to its mass, $mes(\Omega_{(e)})$ its area, n_{nodes} the number of nodes in the cut element and $H(x)$ is the Heaviside function.

By using the lumping technique proposed in Eq. (5.14), the critical time step does not tend to be zero when the crack approaches a node. For a better understanding of this fact, in Figure 5.6 the critical time increment derived for the XFEM case (once the

eigenvalue problem is solved) is normalised with the critical time increment obtained for the lumped matrix in the FE problem Δt_c^{lumped} (see Eq. (5.11)). This normalised stable time increment is plotted against the ratio $\frac{d}{L}$ that defines the position of the crack along the element. Although, in Figure 5.6 there is a variation of the stable time increment for the lumped mass matrix with the discontinuity, its minimum is $\Delta t_c = \frac{1}{\sqrt{2}} \Delta t_c^{lumped-XFEM}$ which is different than zero. However, in the case of the consistent mass matrix for the XFEM case (see dashed line in Figure 5.6), the stable time increment is zero when $\frac{d}{L} = 0$ or $\frac{d}{L} = 1$. Therefore, for arbitrary cracks, the stability of the CDM using the presented lumping mass strategy is guaranteed.

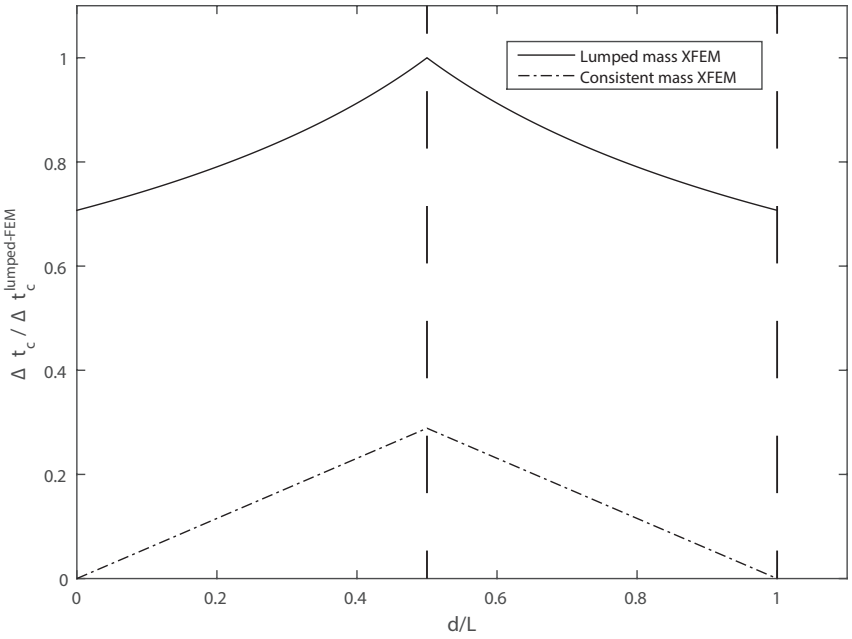

Figure 5.6: Normalised stable time increment against the ratio $\frac{d}{L}$.

The mass lumping technique proposed by Menouillard et al. is valid for cracked elements i.e. presents Heaviside enrichment. However, this lumping technique cannot be applied to elements that contain the crack tip. Following the idea of Menouillard et al. [89], Elguedj et al. [45] derived a mass lumping strategy for crack tip enrichment functions. Therefore, considering the enrichment function present in Eq. (1.19) and the displacement on every point inside an element (see Eq. 1.21), the corresponding

exact and discrete kinetic energy are defined as;

$$T = \frac{1}{2}\int_{\Omega_e} \rho\Phi^2 d\Omega_e \tag{5.15}$$

$$T^h = \frac{1}{2}\dot{U}^T_{x-fem} M \dot{U}_{x-fem} \tag{5.16}$$

If the consistent matrix M is replaced by a diagonal form M_L, the discrete kinetic energy becomes;

$$T^h = \frac{1}{2}\sum_{i=1}^{nnode} m_{L_i}\Phi^2(x_i) \tag{5.17}$$

where m_{L_i} are the terms that form the diagonal of M_L,x_i is the position of the ith node and $nnodes$ is the total number of nodes in an element. Supposing that all diagonal terms in the matrix M_L are identical and tacking into account the conservation of the kinetic energy, the mass lumping matrix for crack tip enrichment function is defined as [45];

$$m^{(e)}_{diag} = \frac{1}{\sum_{i=1}^{nnodes}\Phi^2(x_i)}\int_{\Omega_{el}} \rho\Phi^2(x) d\Omega \tag{5.18}$$

The calculation of the global mass matrix permits the simulation of dynamic problems in the context of explicit XFEM. However, if the static solution is wanted by attenuation of the transient response, an artificial damping is needed. Therefore, in order to obtain the static solution, a new damping strategy is presented in the context of XFEM defined as;

$$C^{damp} = \alpha M_L \tag{5.19}$$

where α is the mass proportional damping coefficient. The damping presented C on Eq. (5.19) is based on the classical damping or proportional damping proposed by Rayleigh [116]. The novelty of the proposed damping relies on the fact that the damping is applied to elements that are enriched with the discontinuous function, i.e. Heaviside function, and elements that are enriched with the crack tip enrichment. Therefore, the local enrichment inherent in XFEM is damped and consequently an artificial damping can be obtained for attenuating the transient response, hence, it is possible to obtain the static solution of the dynamic problem.

It is important to notice that another parameter that affects the stable time increment Δt_n is the damping. Hence, the stable time increment is bounded by the damping ratio and the natural frequencies [35] as follows:

$$\Delta t \leq min \frac{2}{\omega_i} \left(-\xi_i + \sqrt{1+\xi_i^2} \right) \tag{5.20}$$

where ξ_i is the damping ratio at node i.

5.4.3 SIFs calculation

The dynamic stress intensity factors K_I and K_{II} defines the asymptotic stress behaviour next to the crack tip (see Reference [48] for details) :

$$K_I = \lim_{r \to 0} \sqrt{2\pi r}\sigma_{yy} \tag{5.21}$$

$$K_{II} = \lim_{r \to 0} \sqrt{2\pi r}\sigma_{xy} \tag{5.22}$$

For the calculation of K_I and K_{II} using the proposed numerical implementation, the domain integral method [97] together with the interaction energy integral are considered. Taking the interaction energy integral, auxiliary fields are implemented onto the actual fields and therefore a link between mixed-mode SIF and interaction energy integrals is possible. In general, the relation between the J-integral and the SIF is defined as follows:

$$J = \frac{1}{E'}[K_I^2 + K_{II}^2] \tag{5.23}$$

where E' for plane strain conditions is defined as $E' = \frac{E}{1-\nu^2}$. The definition of the J-integral [119] for a homogeneous body, subjected to a two-dimensional deformation field is defined as:

$$J = \int_\Gamma [W dx_2 - T_i \frac{\partial u_i}{\partial x_1} d\Gamma] \tag{5.24}$$

where W defines the strain-energy density, Γ is a curve that surrounds the notch tip (see Figure 5.7), $T_i = \sigma_{ij} n_j$ is the traction vector on the contour Γ, n the unit normal vector to the contour and u is the displacement vector. Note that a Cartesian crack-tip

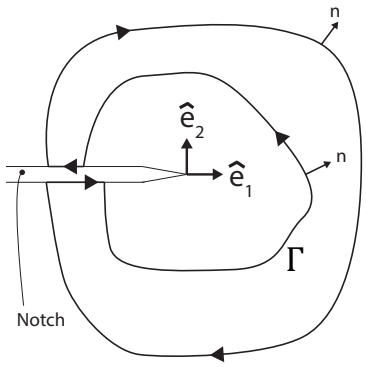

Figure 5.7: Two dimensional space domain for the computation of mixed mode SIF.

coordinate system $(\hat{e}_1, \hat{e}_2)$ is built ahead of the crack tip (see Figure 5.7). Two different stages are considered in the cracked body, the first stage is the present stage ($\sigma_{ij}^{(1)}$, $\epsilon_{ij}^{(1)}$, $u_i^{(1)}$) and the second stage corresponds with an auxiliary stage ($\sigma_{ij}^{(2)}$, $\epsilon_{ij}^{(2)}$, $u_i^{(2)}$). In this implementation, the auxiliary stress and displacements fields near the crack tip are given by Westergaard [153] and Williams [154]. Once terms are rearranged the J-integral for the sum of the two stages is written as:

$$J^{(1+2)} = J^{(1)} + J^{(2)} + I^{(1,2)} \tag{5.25}$$

where $I^{(1+2)}$ is the interaction integral for stages one and two. Finally, it is possible to derive the following for the interaction integral:

$$I^{(1,2)} = \frac{2}{E'}(K_1^{(1)}K_1^{(2)} + K_{II}^{(2)}K_{II}^{(1)}) \tag{5.26}$$

The interaction integral $I^{(1,2)}$ is defined as a function of the auxiliary SIF i.e. $K_1^{(2)}$,$K_{II}^{(2)}$. Thus, for the determination of $K_I^{(1)}$, it is considered $K_I^{(2)} = 1$ and $K_{II}^{(2)} = 0$, and for obtaining $K_{II}^{(1)}$, it is considered $K_I^{(2)} = 0$ and $K_{II}^{(2)} = 1$. Hence, mode I and II are defined in terms of the interaction integral as:

$$K_I^{(1)} = \frac{E'}{2} I^{(1,ModeI)} \tag{5.27}$$

$$K_{II}^{(1)} = \frac{E'}{2} I^{(1,ModeII)} \tag{5.28}$$

The contour definition $I^{(1,2)}$ is converted to an area integral by using a smoothing function q in order to address its numerical evaluation. This function takes a value 1 on innermost contour and a value of zero on the outermost contour.

5.4.4 Numerical implementation

The *in-house* implementation of XFEM is named X^2FEM. The proposed code considers three MATLAB functions extracted from Pais [107]: a function called JIntegral.m, responsible for the calculation of the mixed-mode SIFs, a function called subDomain.m, responsible for subdividing the enriched elements and determining the gauss points and weights and a function called levelSet.m for representing the crack. The author has built the rest of the code i.e. global mass matrix, global stiffness matrix, connectivity matrix, nodal labeling, etc. A schematic representation of the code is depicted on the flowchart presented in Figure 5.10. The code is formed by about 2000 lines in Matlab environment

5.4.4.1 Crack representation

In order to keep track of the evolution of cracks, the level set method (LSM) proposed by Osher and Sethian [104] is considered. This method was originally applied to track the evolution of closed boundaries. Afterwards, it was extended to track evolution of open segments such as crack growth by Stolarska et al.[80]. The level set representation of the crack helps the computation of the enrichment. The crack is represented as the zero level set Φ and all values above or below are either positive or negative (see Eq. (5.29)). In order to define the coordinates of the enrichment function ahead of the crack tip, a local co-ordinate system is considered. These coordinates can be defined using the level set function Ψ where its zero level set is orthogonal to the zero level set Φ at the crack tip. Thus, the orthogonality of the two level sets makes a natural coordinate system as depicted in Figure 5.8. This coordinate system allows to re-define the Heaviside function as:

$$H(f) = \begin{cases} 1 & \text{if} \quad \Phi \geq 0 \\ \\ -1 & \text{if} \quad \Phi < 0 \end{cases} \tag{5.29}$$

The assignment of enrichment in the nodes is addressed from the nodal values of Φ and Ψ. For a certain element, being Φ_{min} and Φ_{max} the minimum and the maximum nodal values of Φ respectively, if $\Psi < 0$ and $\Phi_{max} \cdot \Phi_{min} \leq 0$, then the element is cut by the crack and the enrichment considered is given in Eq.(5.29). On the other hand, being Ψ_{min} and Ψ_{max} the minimum and maximum nodal values of Ψ respectively, in a certain element, if in the element it is satisfied that $\Phi_{min} \cdot \Phi_{max} \leq 0$ and $\Psi_{min} \cdot \Psi_{max} \leq 0$,

then the tip of the crack is located within that element and therefore the element is enriched using Eq.(1.19).

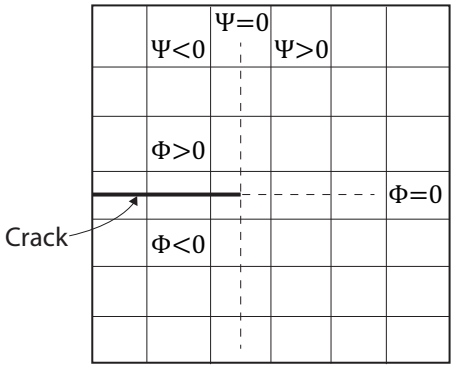

Figure 5.8: Level set co-ordinate system.

In the proposed approach, the mesh contains classical and enriched nodes. The number of enriched nodes for each element, defined in the in-house code with the variable $EN^{(e)}$, will allow to define whether the element does not have enriched nodes i.e. $EN^{(e)} = 0$, or if the element is enriched with Heaviside or crack tip enrichment function i.e. $EN^{(e)} \neq 0$.

The numerical implementation of XFEM has been done for a 4-node quadrilateral element. Each node for a standard element presents two DOF. The nodes of full cracked elements have two classical DOF and two additional DOF addressing the strong displacement jump. On other hand, the nodes of the elements containing the crack tip have two classical DOF and four extra DOF. In order to build the matrices in the code, the strategy adopted by Sukumar et al. [98] is used. Basically, all enriched DOF are allocated in the second part of the vector after the classical DOF.

5.4.4.2 Stiffness matrix and mass lumped matrix

The construction of the global mass matrix is not a trivial task. As mention in Section 5.4.2, the mass lumping strategy adopted for the enriched part is critical for the stability of the CDM. Therefore, different mass lumping strategies are adopted depending on the type of enrichment. The implementation of the global mass matrix in the in-house code is better understood by referring to the flowchart presented in Figure 5.10. As depicted in that flowchart, the variable that takes into account the number of enriched nodes per element (e), $EN^{(e)}$, determines the mass lumping strategy depending on

whether the element presents a enriched node i.e. $EN^{(e)} \neq 0$ or not i.e. $EN^{(e)} = 0$. Hence, if the node is enriched with the Heaviside function, the mass lumping adopted is according to Eq. (5.14) and if the node is enriched with the crack tip enriched function, the strategy adopted is according to Eq. (5.18). For standard elements, direct mass lumping is considered, therefore the total mass of the element is distributed to the nodes. Once the loop over elements is completed, the resultant global mass matrix is assembled considering standard and enriched elements. The main function for the construction of the mass matrix in MATLAB is presented in Appendix C. This function is formed by some sub-functions that helps the calculation of the global mass matrix. The inputs in this function are the global Degree of freedoms called *DOF*, enriched elements called *EE* and the angle of the crack with respect to the horizontal called *anglecrack*. Three different sub-functions are considered along the loop over the elements. The first function, called *mass_element_FEM_XFEM*, is responsible for the calculation of the mass matrix for the FE DOF. The second function *mass_heaviside_XFEM* addresses the nodes enriched with Heaviside enrichment and *mass_tip_XFEM* address the nodes enriched with the crack tip enrichment function.

In the flowchart presented in Figure 5.10, a schematic representation of the main steps for the construction of the stiffness matrix is depicted. In this flowchart, according to the value of the variable $EN^{(e)}$ for a certain element (e), the element is considered as a standard, i.e. $EN^{(e)} = 0$ or enriched, i.e. $EN^{(e)} \neq 0$. For standard elements, the calculation of the stiffness matrix considers four integration points. On the other hand, for elements containing the tip of the crack or cut by the crack, the integrals for the calculation of internal forces cannot be derived by standard quadrature methods since the integrand is defined as discontinuous. Therefore, the standard Gauss quadrature does not adequately consider the discontinuity. The discrete weak form is constructed by a loop over all elements, as the domain Ω is defined as:

$$\Omega = \sum_{e} \Omega_e \tag{5.30}$$

where Ω_e is the element domain. For elements that are cut by the crack or contain the crack tip, the element domain is defined as the sum of a set of subtriangles whose boundaries are aligned with the crack definition, hence:

$$\Omega_e = \sum_{s} \Omega_s \tag{5.31}$$

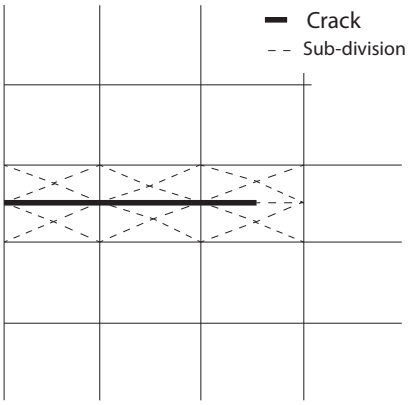

Figure 5.9: Sub-triangles for the quadrature of the weak form .

The subdivision of the elements into sub-triangles [29, 95] just has integration purposes, hence, no additional DOF are added to the system. It is important to note that to get accurate results in the sub-triangles, high order Gauss quadrature rule is used. For a better understanding of the sub-division Figure 5.9 presents a crack where the elements cut or containing the crack are sub-divided in the integration process.

The main function for the construction of the stiffness matrix in MATLAB for a linear isotropic material is presented in Appendix D. This function is formed by some sub-functions that help the calculation of the global stiffness matrix. The input arguments for this function are the angle of the crack in respect to the horizontal *anglecrack*, the global DOF, *DOF* and the enriched elements *EE*. The stiffness function for the elements with no enriched nodes is calculated initially in the function *initia*. For those elements, the stiffness is constant during the simulation since in Appendix D a linear isotropic material is considered. For the fully or partially enriched elements, stiffness cannot be derived by standard quadrature methods since the integrand is defined as discontinuous. By means of the function *gauss_jaco_weight*, the elements are subdivided and additionally the Gauss points and weight considered in the integration and assembly of the stiffness are obtained. In this function, a loop is described over the Gauss points and the derivative matrix for the shape functions, Heaviside function and crack tip function is obtained. At the end of the loop over Gauss points, the whole stiffness matrix of the system is assembled.

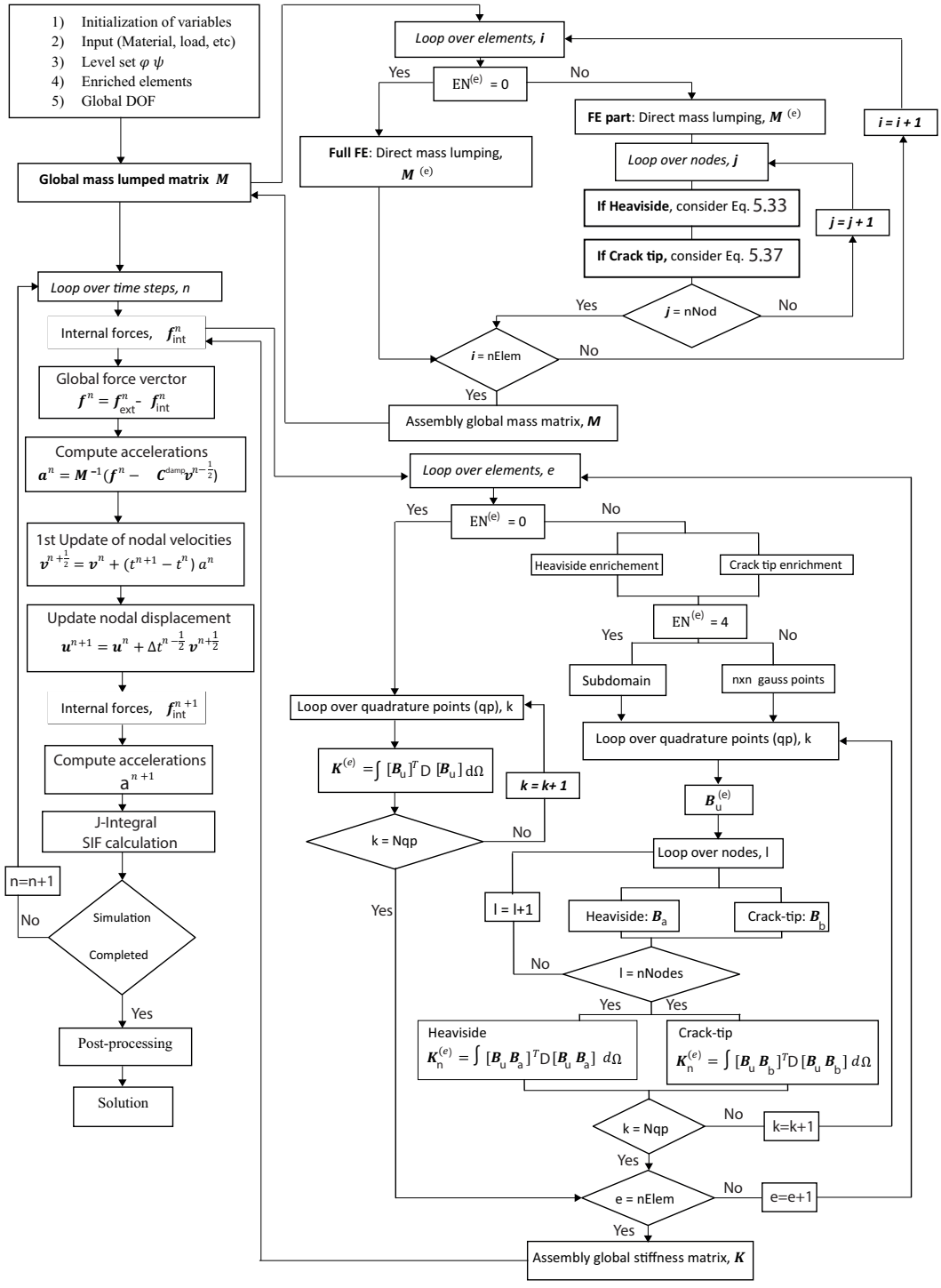

Figure 5.10: Flowchart of the main steps for the construction of the in-house code

5.4.5 Numerical Results

This section tests the performance of the presented approach by analysing several examples. Initially, a semi-infinite stationary crack within an infinite plate is simulated. The plate is loaded in its vertical edge as depicted in Figure 5.11. The influence of the external loading on the SIF calculation is addressed. Hence, the load applied is introduced in three different manners: as a jump, a ramp and a sinusoidal wave. The dynamic SIFs obtained from the code are compared with the analytical solution. The second example is presented in Section 5.4.5.2 where a finite plate with an edge crack is analysed (see Figure 5.16). The material considered in this example is a CGRP composite. The load is applied vertically and the crack is defined as stationary. The static solution is obtained by adding an additional term in the equation of motion i.e. a viscous damping. Finally, Section 5.4.5.3 addresses the simulation of fracture in the 10° off-laminate studied in Chapter 2. By means of this example, it is possible to see how, with the proposed approach, a correct crack path is achieved if it is compared with the experimental outcomes presented in Chapter 2.

5.4.5.1 Analysis of a stationary mode I crack

A schematic representation of the problem under consideration is depicted in Figure 5.11 where a tensile stress is applied perpendicular to the crack. The analytical solution of the SIF in mode I (denoted as K_I) for a linear elastic material was first proposed by Freund [48]. The analytical solution was obtained under the assumptions of an infinite plate with a semi-infinite crack. This solution is valid until the tensile wave stress is reflected in the bottom of the plate and reaches again the crack tip. The time needed by the wave stress to reach the crack tip is calculated as $t_c = \frac{h}{c_d} = 3.36 \cdot 10^{-4} s$, where $c_d = c_1\sqrt{\frac{k+1}{k-1}} = 5944.5\, m/s$ is the dilatational wave speed being $c_1 = \sqrt{\frac{\mu}{\rho}}$. Note that μ is the second Lamé constant, ρ the density and k the Kolosov constant in plane strain (see Table 5.2). The duration of the simulation is $t \leq 3t_c = 1.009 \times 10^{-3} s$ and beyond this value the analytical solution is not longer valid. Plane strain conditions are considered.

The dimensions of the plate are L=10 m, h=2 m and the crack length is a=5 m. The material properties are presented in Table 5.2 where E is the elasticity modulus, ν the Poisson ratio and ρ the density. As Freund [48] proposed, when the crack reaches

the crack tip, the analytical solution for mode I dynamic stress intensity factor for the stationary crack is written as:

$$K_1^{dyn}(0,t) = \frac{2\sigma_o(t)}{1-\mu}\sqrt{\frac{c_d t(1-2\mu)}{\pi}} \tag{5.32}$$

where $\sigma_o(t)$ is the stress applied and t represents the time.

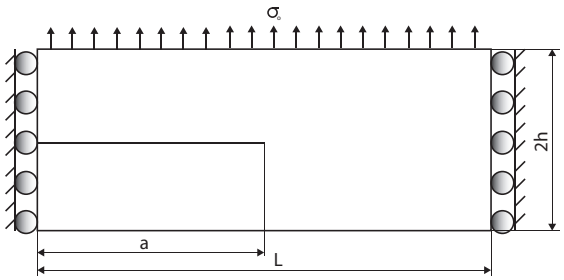

Figure 5.11: Geometry and loading for an infinite plate with a semi-infinite crack.

$E[GPa]$	ν	$\rho[kg/m^3]$	$\mu[GPa]$	k
210	0.3	8000	80.76	1.8

Table 5.2: Mechanical properties

In Figure 5.12, the normalised mode I dynamic SIF $\frac{K_I}{\sigma_o\sqrt{h}}$ is depicted against the normalised time $\frac{t}{t_c}$. This graph serves to point out the mesh independence of the solution using two different discretisations with 92x39 and 140x59 elements. These discretisations were considered in order to have an aspect ratio of approximately one in the mesh. Note that the time step considered is $\Delta t_c^{XFEM} = 5\mu s$ (a simulation of 200 time steps). The tensile load applied $\sigma_0(t)$ is defined as $\sigma_0(t) = \sigma g^n(t)$, where $\sigma = 500MPa$ and $g^n(t)$ defines the way that the load is provided. Initially, a step load $g^1(t)$ is applied to the plate as follows:

$$g^1(t) = \begin{cases} 0 & \text{if} \quad t \leq 0 \\ \\ 1 & \text{otherwise} \end{cases} \tag{5.33}$$

The results depicted in Figure 5.12 for this loading condition show a reasonable agreement between the analytical and the computational solution for the coarse and

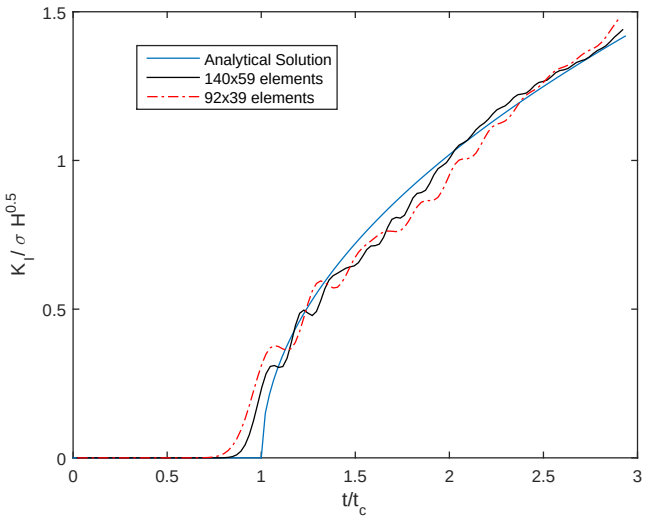

Figure 5.12: Normalised mode I stress intensity factor against normalised time for a stationary semi-infinite crack. The analytical solution is plotted as well as the computational solution considering two different discretisations: 92 by 39 and 140 by 59 elements .

fine mesh, which consequently proves the ability of the proposed code for the calculation of SIF considering different discretisations.

For a better understanding of the spreading process of the stress wave along the plate, in Figure 5.13, the vertical component of the stress (σ_y) is depicted for different times during the simulation. By means of this sequence, the wave stress is localised before it reaches the crack tip (t= 200μs), while it is reaching the crack tip (t=500μs) and after bouncing off the bottom edge (t=800μs).

Some oscillations in the SIF calculation are found when the load is applied as an step wave, $g^1(t)$ (see Figure 5.12). This observation was also noticed by other authors, [45, 89]. Therefore, in order to address the sensibility of the proposed approach to different loading scenarios, a ramp loading $g^2(t)$ (see Eq. (5.34)) and sinusoidal loading $g^3(t)$ (see Eq.(5.35)) are considered. Those definitions are applied from the beginning of the simulation until $T = 0.2t_c$. Afterwards ($t > T$), the whole magnitude of stress is applied. Results from those loading cases (see Figure 5.14), considering a mesh of 140 by 59 elements, present a smoother solution than the jump loading as well as reasonable agreement with the analytical solution.

$$g^2(t) = \begin{cases} 0 & \text{if} \quad t \leq 0 \\ \frac{t}{T} & \text{if} \quad 0 \leq t \leq T \\ 1 & \text{otherwise} \end{cases} \tag{5.34}$$

$$g^3(t) = \begin{cases} 0 & \text{if} \quad t \leq 0 \\ \frac{1}{2}(1 - cos(\frac{\pi t}{T})) & \text{if} \quad 0 \leq t \leq T \\ 1 & \text{otherwise} \end{cases} \tag{5.35}$$

It is observed that the main source of error in the calculation of dynamic SIF is when the wave stress reaches the crack tip i.e. $t = t_c$. This discrepancy is justified due to the fact that the tensile stress wave affects the contour of the interaction integral for the SIF computation before it reaches the crack tip. This source of error has also been addressed by another author e.g. [89]. As it is illustrated in Figure 5.12, a finer mesh provides better results because a small contour is used. It is also worth saying that for a smoother loading i.e. $g^2(t)$ and $g^3(t)$, the error near $t = t_c$ is decreased as depicted in Figure 5.14.

Additionally, point out the discrepancy between the analytical and the computational outcome once the wave stress has passed the crack, the relative error of K_I with respect to the normalised time from $t = 1.4t_c$ till the end of the simulation is depicted in Figure 5.15. It is noticed that the relative error trend to 2 % when loading is applied following equations (5.34) and (5.35) and to 4 % considering Eq. (5.33).

5.4.5.2 Static analysis of a plate with an edge crack

In this section, a plate with an edge crack is analysed as depicted in Figure 5.16. The major dimensions of the plate are $2L$= 20 mm, W=10 mm and the crack length is defined as a. The material considered is a CGRP composite that experimentally behaves as a quasi-isotropic [126]. Thus, it is assumed to be computationally isotropic. The properties of the material are presented in Table 5.3 where E is the young modulus, ν the Poisson ratio, ρ the density of the composite.

The exact value of K_I for a plate with an edge crack is given as [122]

$$K_I = C\sigma\sqrt{a\pi} \tag{5.36}$$

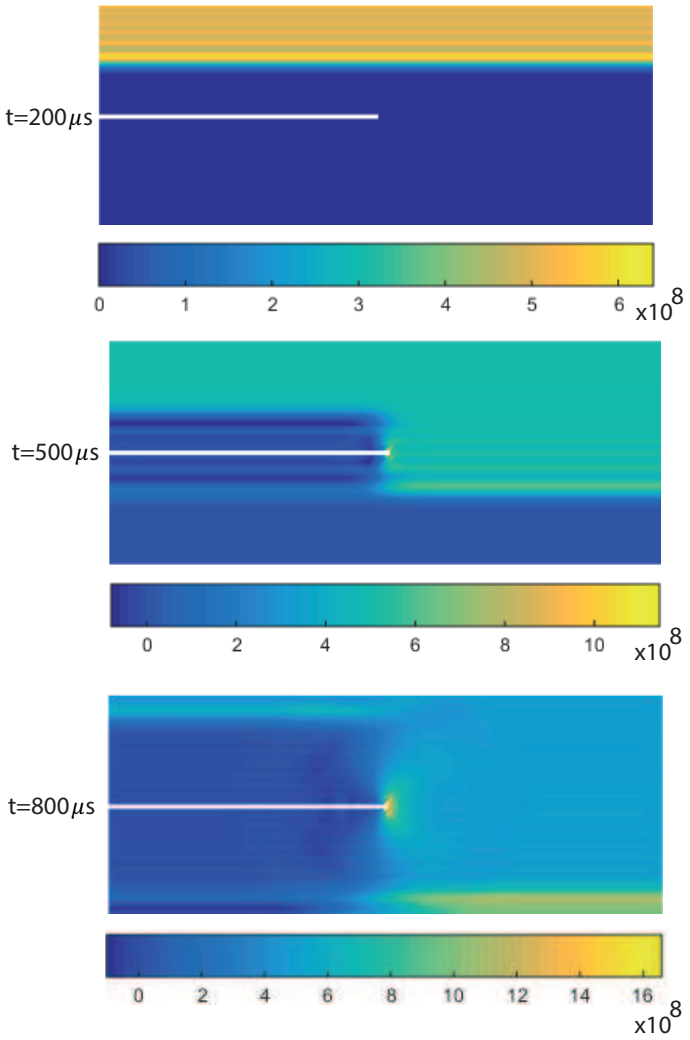

Figure 5.13: σ_y[Pa] throughout the plate for different times during the simulation $t = 200, 500$ and $800\mu s$. The load is applied by means of a step. The mesh considered is 140x59 elements.

where C is the finite-geometry correction factor defined as:

$$C = 1.12 - 0.231\left(\frac{a}{w}\right) + 10.55\left(\frac{a}{w}\right)^2 - 21.72\left(\frac{a}{w}\right)^3 + 30.39\left(\frac{a}{w}\right)^4 \tag{5.37}$$

In this example, the load is applied as a step with a magnitude of 30 MPa and different crack lengths are considered. Three different meshes of 31x61, 41x81 and 51x10 elements were considered during simulations for each of the crack lengths studied. Those meshes are intended to present an aspect ratio of approximately one. The

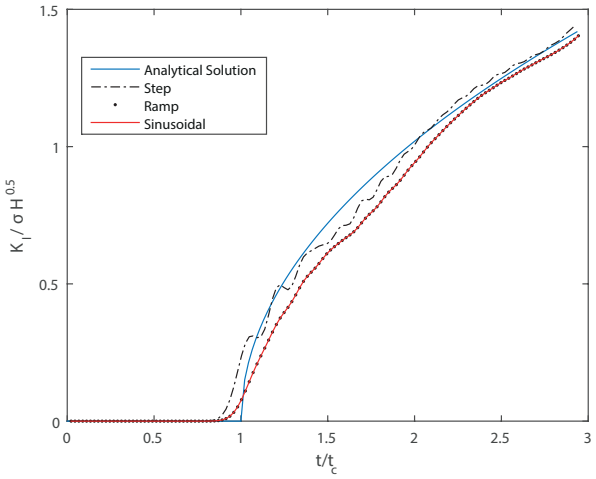

Figure 5.14: Normalised K_I against normalised time considering different loadings: step, ramp and sinusoidal wave. A mesh of 150x59 elements is considered.

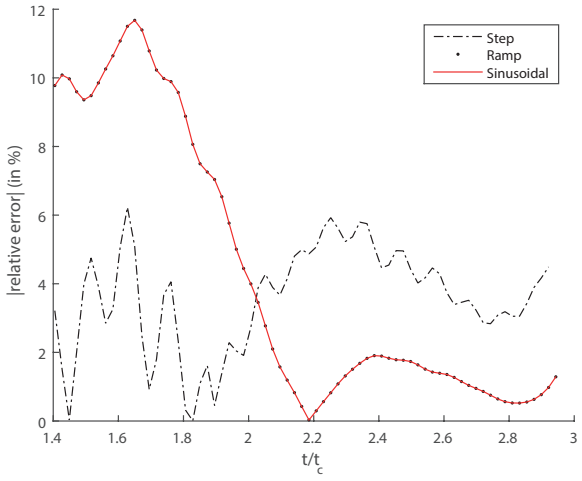

Figure 5.15: Absolute relative error of K_I for loading inputs considered.

loading stresses considered for analysis are lower than the critical load $\sigma^C = \frac{K_I^C}{C\sqrt{a\pi}}$ for the different lengths of the crack studied where K_I^C is the fracture toughness of the composite. The experimental value of K_c^I is unknown. However, the fracture energy G_{Ic} is known. Irwin showed [8] that for an isotropic material and assuming plane strain,

$E[GPa]$	ν	$\rho[kg/m^3]$	$K_c^I[Pa \cdot m^{\frac{1}{2}}]$	$G_{Ic}[\frac{N}{m^2}]$
6.5	0.37	1440	$6.83 \cdot 10e^6$	6210

Table 5.3: Mechanical properties CGRP composite

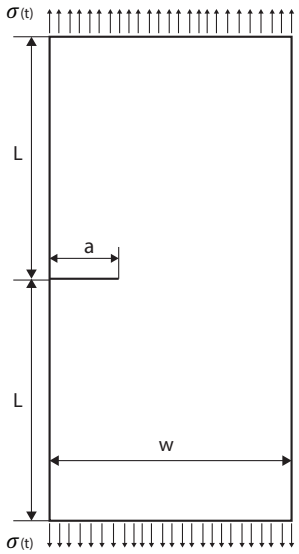

Figure 5.16: Geometry and loading for the infinite plate.

the critical energy and the critical SIF are related by means of the following equation:

$$K_c^I = \sqrt{\frac{E}{(1-\nu^2)} G_{Ic}} \tag{5.38}$$

where G_{Ic} is the fracture energy derived from [125] [99]

On Table 5.4, the computational and analytical values of mode I of fracture K_I are presented for different crack lengths. The relative error between those values ranges between 16.92 and 12 %. Therefore, an approximation of the theoretical values is obtained using the new damping strategy proposed in the current approach. The results presented in Figure 5.17 clearly show how the dynamic solution oscillates around the static solution for different discretisations until there are no oscillations.

a[mm]	$K_I^{Theo}[Pa \cdot m^{\frac{1}{2}}]$	$K_I^{Comp.}[Pa \cdot m^{\frac{1}{2}}]$	Relative error (%)
3	$4.83 \cdot 10^6$	$5.49 \cdot 10^6$	13.66
4	$7.07 \cdot 10^6$	$8.10 \cdot 10^6$	14.56
5	$10.62 \cdot 10^6$	$12.01 \cdot 10^6$	13.08
6	$16.58 \cdot 10^6$	$18.59 \cdot 10^6$	12.12

Table 5.4: Mode I SIF calculation considering different crack sizes

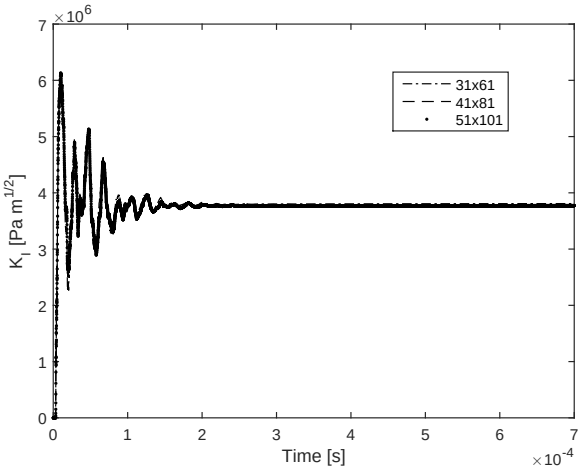

Figure 5.17: SIF in mode I K_I versus time t for a crack 2 mm long.

5.4.5.3 A possible solution for the limitation of PDMs

In Chapter 2, a numerical and experimental analysis was carried out in order to address the behaviour of a 10° off-axis laminate. Through this example, a limitation in PDM to correctly address its crack behaviour was pointed out (See Section 2.3). The main conclusion for this analysis was that the micromechanical effects for cracks to grow are not considered in PDM because the material is homogenised [146]. Therefore, since the matrix crack is an event observed at the microscale, the transition between microlevel to mesolevel disappears and consequently, in this case, the PDM is not capable of addressing its crack path correctly. A possible alternative to overcome this was proposed by van der Meer and Sluys [147]. They proposed a phantom node formulation with mixed mode cohesive law. This section proposes a different solution to solve the limitation encountered in PDM. The explicit XFEM approach formulated

in this section is adopted. Therefore, the 10° laminate studied in Section 2 is considered as an example for simulations. Experimentally, it was observed that the crack runs at 10° (see Figure 2.7) and propagates throughout the matrix, which is locally isotropic. Hence, it is assumed that the asymptotic displacement field ahead of the crack tip can be defined by means of the enrichment function presented by Eq. (1.19) for the enriched nodes at the crack tip. As discussed in this chapter, Eq. (1.19) guarantees the stability of the CDM.

The objective of this section is to demonstrate that the proposed approach is capable of addressing the crack path for the 10° off-axis laminate. However, before that, it is necessary to prove that the in-house code is capable of addressing the elastic displacement field for the $[10°]_6$ laminate. The specimen chosen for this analysis is the specimen with oblique end-tab studied in Chapter 2 and its properties were presented in table 2.2. The linear behaviour of the specimen was studied by means of FE simulations using ABAQUS where a displacement was applied until the force was 4.5 KN in the right edge. Additionally, the maps of strain were validated though experimental testing using the DIC.

The boundary conditions and mesh (1400 elements) for the analysis of the specimen with oblique end-tab is shown in Figure 2.4. The horizontal u_x displacement field obtained at 4.5 KN by FE simulations using ABAQUS is presented in Figure 5.18. The same boundary conditions and material were adopted for the simulation with the in-house code but considering a discretisation of 600 elements. The horizontal displacements obtained (see Figure 5.19) are the same as the ones obtained using ABAQUS. Consequently, the elastic behaviour of the composite is validated.

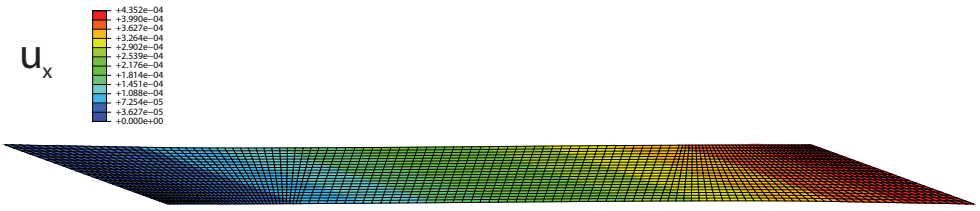

Figure 5.18: Horizontal displacement u_x for the oblique specimen using ABAQUS. The load applied is 4.5 KN.

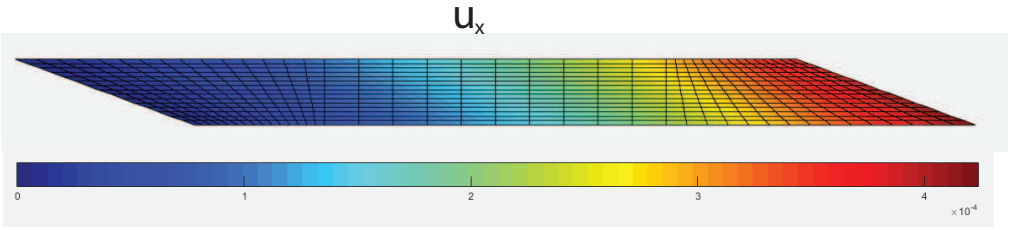

Figure 5.19: Horizontal displacement u_x for the oblique specimen using the MATLAB code. The load applied is 4.5 KN.

The specimen with oblique end-tab under analysis presents a homogeneous state of strain. Therefore, using an initiation criteria based on stresses, initiation is satisfied in the whole specimen at once due to its homogeneity (see Figure 2.12). Based on this fact, it is assumed that the crack is initiated in the middle of the specimen as it was observed during experimental loading. This assumption is logical since it is what actually happens in experiments.

In order to check that the current approach is capable of addressing the crack path of the laminate, four different stationary cracks are considered for simulations with lengths of 10, 20, 30 and 40 mm. The load is applied incrementally on the right edge of the specimen and on the left edge the specimen is fixed horizontally and vertically. In this case, 2400 elements are used.

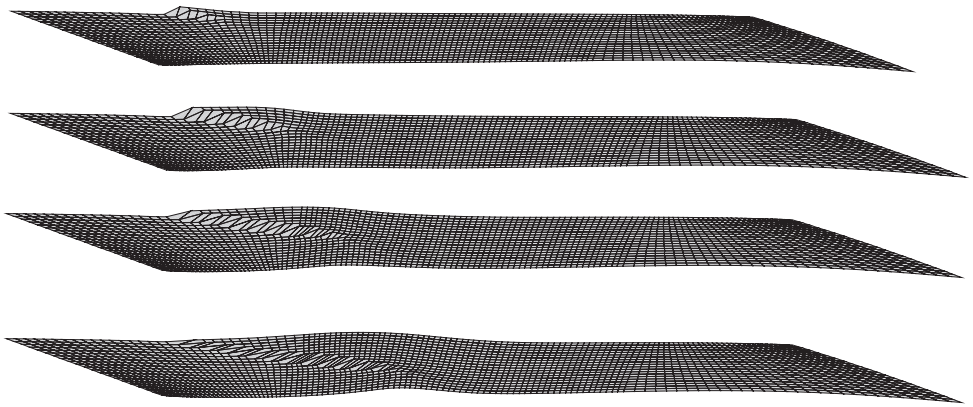

Figure 5.20: Deformed meshes for four different crack sizes. It is considered a deformation factor of 100. The meshes have 2400 elements.

In Figure 5.20, the results obtained from the in-house code are depicted. It is observed that the crack path follows the experimental crack direction at 10°. This

is not a big deal since the crack direction is pre-defined. However, this is the great advantage compared with PDM since, by means of XFEM, the crack direction can be controlled and therefore the micromechanics nature is addressed at the mesoscale level.

5.5 Conclucions

In this chapter, a new approach for modelling stationary cracks in the framework of XFEM has been proposed. Initially, the proposed approach has been considered for the simulation of a stationary mode I crack and the static analysis of a plate with an edge crack. Afterwards, the computational results obtained were compared with theoretical outcomes. Once the approach was validated, the main objective was to solve the limitation encountered in PDM for correctly address the crack path in a 10° off-axis laminate. The results obtained for this test show that the computational crack path follows the experimental crack direction. Therefore, using the proposed approach, the micromechanics nature of the ACM is addressed at the mesoscale level solving the limitation presented in chapter 2 with PDM.

6

Conclusions and discussion

6.1 New improvements

In this work, the main contributions for the simulation of damage and fracture in advanced composite structures are:

1. The XFEM has been used in some applications, however, it is important to underline that there are very few dealing with biaxial stress states e.g. [67]. In this thesis, the author presents the first endeavour to research with XFEM the 2D and 3D crack initiation and propagation of cracks on a randomly oriented fibre composite under biaxial loading without defining the initial position of the crack.

2. In this thesis, the first endeavour to investigate the SIFs into a CGRP cruciform structure submitted to biaxial loading by means of XFEM has been accomplished. The calculation of SIFs in the cruciform specimen are altered by the edge effects of the specimen. Based on the analysis of the edge effects, a novel ratio relating the crack size and the dimensions of the cruciform is suggested. This ratio allows edge effects to be mitigated with the smallest cruciform design possible.

3. A 3D damage modelling analysis has been considered for a CGRP cruciform structure. The structure is tensile loaded in two different in-plane directions and the presented study represents the first attempt to research the 3D damage response within a composite cruciform structure subjected to biaxial loading. For the computation of damage, the damage rate considers material properties of the composite such as the stiffness/volume ratio.

4. A new approach for dynamic analysis of stationary cracks using XFEM is derived.

Different mass lumping strategies are adopted for standard and enriched elements. This approach is capable of addressing dynamic and static fracture mechanics problems. Additionally, by means of this relatively simple approach, it is possible to address correctly the crack pattern of a ten off-axis laminate contrary to progressive damage modelling where a wrong crack path was observed.

5. Tacking into account the global mass matrix derived for standard and enriched elements (Heaviside and crack tip enrichment), a damping strategy for solving static problems is determined.

6. An experimental analysis has been carried out within a 10° off-axis laminate using DIC. Therefore, the whole experimental maps of strains have been addressed for the proposed geometries using straight and oblique end-tabs. This experimental analysis serves well for validating the numerical framework proposed.

6.2 Conclusions

The numerical tools proposed have been tested by means of numerical tests and validated with analytical and experimental outcomes. An investigation of the applicability of XFEM applied to biaxial loading of composites has been given. The XFEM is used to study the complex crack propagation problems which appear on cruciform specimens subjected to a biaxial loading scenario. The convergence of the solution in agreement to the experimental results is an issue that has been solved. The simulations have been able to reproduce the experimental results such as: crack initiation, its evolution path, velocity and the value of applied stress which produces the failure of the specimen. The constitutive model considers a linear elastic behaviour followed by a linear softening law evolution. This constitutive model is enough to predict the response of the composite due to the brittle and quasi-isotropic behaviour of the CGRP under consideration.

SIFs have been calculated for infinite plates subjected to biaxial loading. Tacking that into account, the 3D model is validated. Hence, SIFs are also calculated for the whole cruciform specimens. In order to minimise the edge effects and specimen size simultaneously, a new ratio relating the side of the central zone and the crack length is proposed. As has been shown, 3D modelling initiation and propagation was not

straightforward. The main points addressed were: 3D propagation of a crack front without pre-notching and initiation criteria. It is important to underline that no deterioration of the solution was noticed in terms of validation against experimental tests. In addition, a more realistic view of the crack is provided.

The simulation of damage in a cruciform structure has been carried out. For doing that, a 3D PDM has been implemented within the numerical method addressing the material non-linearity. Two damage modes have been considered: matrix cracking and fibre rupture. These two damage modes are responsible for provoking the macro-crack initiation in the rounded zone of the cruciform. Therefore, the PDM has been able to:
- Properly localise the damage compared with experimental tests. Two damage agents are taken into account (fibre rupture and matrix cracking) for the computation of damage.
- Correctly compute the initiation of damage based on a maximum principal stress criterion. Hence, when the value of maximum principal stresses in the rounded zone reached 90 MPa the damage process started. This behaviour was also observed in experimental tests.

Considering the computational results obtained and the experimental outcomes, it is possible to stablish that the PDM successfully predicts damage initiation in a complex loading scenario such as the biaxial. In addtion, a realistic amount of energy is dissipated. The strategy adopted takes material properties of the composite such as the stiffness/volume ratio.

Another important conclusion is extracted from Chapter 1. It is established that the use of progressive damage modelling i.e a continuous approach, should not be trusted for matrix cracks in laminates. Basically, the micromechanical influence for cracks to grow is not taken into account in the continuous models because the material is homogenised. Thus, since matrix cracking is a typical microscale event, the transition between microlevel to mesolevel disappears, and then, the continuous model is not suitable for addressing its crack adequately. In order to overcome this issue, the XFEM approach presented in Chapter 5 is capable of addressing matrix cracks in the laminate

analysed. Considering this approach, it is observed that the crack path follows the experimental crack direction. This is not unusual since the crack direction is pre-defined. However, this is a great advantage compared with PDM since, by means of XFEM, the crack direction is controlled and therefore the micromechanics nature is addressed at the mesoscale level.

6.3 Future developments

The work in this thesis is limited and some improvements for the future may be considered:

- Uniaxial and biaxial tests are carried out in the thesis. However, a more complex loading scenario such as out-of-plane loading may be simulated in order to replicate the behaviour of some advanced composite structures while working conditions. Additionally, the tests carried out consider tensile loading, this work may be extended, for instance, to shear and compression.

- The results obtained are mesh independent. For instance, for the 3D PDM it was intended to provide a meaningful value of energy dissipated during the stiffness degradation. Nevertheless, a more robust approach such as regularisation technique can improve the numerical approach.

- The 3D progressive damage model considered addresses the majority of the damage modes i.e. fibre rupture and kicking, matrix cracking and crushing in the first transverse direction and matrix cracking and crushing in the second transverse direction. However, in computational terms, delamination between plies is not addressed. Its implementation could address in future developments in order to reproduce this interface failure.

- It is well known that the cohesive XFEM approach i.e. remove the stress singularity and propose a traction-separation behaviour, serves the macro-crack behaviour well. However, for describing the fracture process zone, in particular, the initial distributed microcracks, the use of XFEM is not convenient. On the other hand, PDM is capable of describing the first phase of microcracks properly. Hence, a hybrid approach (PDM and XFEM) may be a powerful solution to describe the whole fracture process observed

in ACM.

References

[1] **www.boeing.com**. v, 3

[2] Hamouine Abdelaziz, Y. **A survey of the extended finite element**. *Computers & structures*, **86**(11):1141–1151, 2008. 13

[3] Olivier Allix and Pierre Ladevèze. **Interlaminar interface modelling for the prediction of delamination**. *Composite structures*, **22**(4):235–242, 1992. 14

[4] Marreddy Ambati, Tymofiy Gerasimov, and Laura De Lorenzis. **Phase-field modeling of ductile fracture**. *Computational Mechanics*, **55**(5):1017–1040, 2015. 15

[5] Marreddy Ambati, Tymofiy Gerasimov, and Laura De Lorenzis. **A review on phase-field models of brittle fracture and a new fast hybrid formulation**. *Computational Mechanics*, **55**(2):383–405, 2015. 15, 16

[6] Hanen Amor, Jean-Jacques Marigo, and Corrado Maurini. **Regularized formulation of the variational brittle fracture with unilateral contact: numerical experiments**. *Journal of the Mechanics and Physics of Solids*, **57**(8):1209–1229, 2009. 15

[7] Ted L Anderson. *Fracture mechanics: fundamentals and applications*. CRC press, 2005. 51

[8] Ted L Anderson and TL Anderson. *Fracture mechanics: fundamentals and applications*. CRC press, 2005. 99

[9] Pedro MA Areias, JH Song, and Ted Belytschko. **Analysis of fracture in thin shells by overlapping paired elements**. *Computer Methods in Applied Mechanics and Engineering*, **195**(41):5343–5360, 2006. 15

[10] I. Babuka and J.M. Melenk. **The partition of unity method**. *International Journal for Numerical Methods in Engineering*, **40**(4):727–758, 1997. 82

[11] I Babuska and Jens M Melenk. **The partition of unity finite element method**. Technical report, DTIC Document, 1995. 9

[12] Zdeněk P Bažant and Byung H Oh. **Crack band theory for fracture of concrete**. *Matériaux et construction*, **16**(3):155–177, 1983. 8, 35, 67

[13] Zdenek P Bazant and Gilles Pijaudier-Cabot. **Nonlocal continuum damage, localization instability and convergence**. *Journal of applied mechanics*, **55**(2):287–293, 1988. 16

[14] T Belytschko and T Black. **ELASTIC CRACK GROWTH IN FINITE ELEMENTS**. **620**(July 1998):601–620, 1999. 9

[15] T. Belytschko, H. Chen, J. Xu, and G. Zi. **Dynamic crack propagation based on loss of hyperbolicity and a new discontinuous enrichment**. *International Journal for Numerical Methods in Engineering*, **58**(12):1873–1905, 2003. 82

[16] Ted Belytschko. *Nonlinear finite elements for continua and structures*. Chichester : John Wiley, c2000, Chichester, 2000. 12, 75, 76

[17] Ted Belytschko and Tom Black. **Elastic crack growth in finite elements with minimal remeshing**. *International journal for numerical methods in engineering*, **45**(5):601–620, 1999. 82

[18] Ted Belytschko and Robert Gracie. **On XFEM applications to dislocations and interfaces**. *International Journal of Plasticity*, **23**(10):1721–1738, 2007. 13

[19] Ted Belytschko, Robert Gracie, and Giulio Ventura. **A review of extended/generalized finite element methods for material modeling**. *Modelling and Simulation in Materials Science and Engineering*, **17**(4):043001, 2009. 13

[20] Ted Belytschko, Wing Kam Liu, Brian Moran, and Khalil Elkhodary. *Nonlinear finite elements for continua and structures*. John Wiley & Sons, 2013. 63, 117, 118

[21] Michael J Borden, Thomas JR Hughes, Chad M Landis, and Clemens V Verhoosel. **A higher-order phase-field model for brittle fracture: Formulation and analysis within the isogeometric analysis framework**. *Computer Methods in Applied Mechanics and Engineering*, **273**:100–118, 2014. 15

[22] Blaise Bourdin, Gilles A Francfort, and Jean-Jacques Marigo. **Numerical experiments in revisited brittle fracture**. *Journal of the Mechanics and Physics of Solids*, **48**(4):797–826, 2000. 15

[23] Pedro Ponces Camanho and FL Matthews. **Stress analysis and strength prediction of mechanically fastened joints in FRP: a review**. *Composites Part A: Applied Science and Manufacturing*, **28**(6):529–547, 1997. 8

[24] PP Camanho and FL Matthews. **A progressive damage model for mechanically fastened joints in composite laminates**. *Journal of Composite Materials*, **33**(24):2248–2280, 1999. 8

[25] J. L. Chaboche. **Damage induced anisotropy: on the difficulties associated with the active/passive unilateral condition**. *International Journal of Damage Mechanics*, **1**(2):148–171, 1992. 60

REFERENCES

[26] Jean-Louis Chaboche. **Continuous damage mechanicsa tool to describe phenomena before crack initiation**. *Nuclear Engineering and Design*, **64**(2):233–247, 1981. 6, 8, 60

[27] C. C Chamis and J. H Sinclair. **Ten-deg off-axis test for shear properties in fiber composites**. *Experimental mechanics.*, **Vol.17(9)**(3):339–346, 1977. 20

[28] Fu-Kuo Chang and Kuo-Yen Chang. **A progressive damage model for laminated composites containing stress concentrations**. *Journal of composite materials*, **21**(9):834–855, 1987. 8

[29] J. Chessa, H. Wang, and T. Belytschko. **On the construction of blending elements for local partition of unity enriched finite elements**. *International Journal for Numerical Methods in Engineering*, **57**(7):1015–1038, 2003. 92

[30] T.C. Chu, W.F. Ranson, and M.A. Sutton. **Applications of digital-image-correlation techniques to experimental mechanics**. *Experimental Mechanics*, **25**(3):232–244, 1985. 29

[31] A. Corigliano. **Formulation, identification and use of interface models in the numerical analysis of composite delamination**. *International Journal of Solids and Structures*, **30**(20):2779–2811, 1993. 14

[32] R. Courant, K. Friedrichs, and H. Lewy. **ber die partiellen Differenzengleichungen der mathematischen Physik**. *Mathematische Annalen*, **100**(1):32–74, 1928. 74, 119

[33] Brian Cox and Qingda Yang. **In Quest of Virtual Tests for Structural Composites**. *Science*, **314**(5802):1102–1107, November 2006. 2

[34] W. Cui and M.R. Wisnom. **A combined stress-based and fracture-mechanics-based model for predicting delamination in composites**. *Composites*, **24**(6):467–474, 1993. 14

[35] J. L. Curiel Sosa, E. de Souza Neto, and D .R. J. Owen. **A combined implicit-explicit algorithm in time for non-linear finite element analysis**. *Communications in Numerical Methods in Engineering*, **22**(1):63–75, 2006. 87

[36] J. L. Curiel Sosa and A. J. Gil. **Analysis of a continuum-based beam element in the framework of explicit-FEM**. *Finite Elements in Analysis and Design*, **45**(8-9):583–591, 2009. 82

[37] J. L. Curiel-Sosa and N. Karapurath. **Delamination modelling of GLARE using the extended finite element method**. *Composites Science and Technology*, **72**(7):788–791, 2012. 13, 60, 63

[38] J. L. Curiel-Sosa, N. Petrinic, and J. Wiegand. **A three-dimensional progressive damage model for fibre-composite materials**. *Mechanics Research Communications*, **35**(4):219–221, 2008. 63

[39] J. L. Curiel-Sosa, S. Phaneendra, and J. J. Munoz. **Modelling of mixed damage on fibre reinforced composite laminates subjected to low velocity impact**. *International Journal of Damage Mechanics*, page 1056789512446820, 2012. 60

[40] R De Borst, L J Sluys, H-B Muhlhaus, and Jerzy Pamin. **Fundamental issues in finite element analyses of localization of deformation**. *Engineering computations*, **10**(2):99–121, 1993. 8, 66

[41] S Demmerle and JP Boehler. **Optimal design of biaxial tensile cruciform specimens**. *Journal of the Mechanics and Physics of Solids*, **41**(1):143–181, 1993. 16

[42] J. Dolbow, N. Mos, and T. Belytschko. **An extended finite element method for modeling crack growth with frictional contact**. *Computer Methods in Applied Mechanics and Engineering*, **190**(51-52):6825–6846, 2001. 13

[43] Qinglin Duan, Jeong-Hoon Song, Thomas Menouillard, and Ted Belytschko. **Element-local level set method for three-dimensional dynamic crack growth**. *International Journal for Numerical Methods in Engineering*, **80**(12):1520–1543, 2009. 15

[44] Ulf Edlund and Pieter Volgers. **A composite ply failure model based on continuum damage mechanics**. *Composite Structures*, **65**(3-4):347–355, September 2004. 8

[45] T. Elguedj, A. Gravouil, and H. Maigre. **An explicit dynamics extended finite element method. Part 1: Mass lumping for arbitrary enrichment functions**. *Computer Methods in Applied Mechanics and Engineering*, **198**(30-32):2297–2317, 2009. 12, 85, 86, 96

[46] M. Fleming, Y.A. Chu, B. Moran, and T. Belytschko. **Enriched element-free galerkin methods for crack tip fields**. *International Journal for Numerical Methods in Engineering*, **40**(8):1483–1504, 1997. 12

[47] Gilles A Francfort and J-J Marigo. **Revisiting brittle fracture as an energy minimization problem**. *Journal of the Mechanics and Physics of Solids*, **46**(8):1319–1342, 1998. 15

[48] L Benjamin Freund. *Dynamic fracture mechanics*. Cambridge university press, 1998. 87, 94

[49] ThomasPeter Fries and Ted Belytschko. **The extended/generalized finite element method: an overview of the method and its applications**. *International Journal for Numerical Methods in Engineering*, **84**(3):253–304, 2010. 9

[50] A. Giachetti. **Matching techniques to compute image motion**. *Image and Vision Computing*, **18**(3):247–260, 2000. 29

[51] Robert Gracie, Jay Oswald, and Ted Belytschko. **On a new extended finite element method for dislocations: core enrichment and nonlinear formulation**. *Journal of the Mechanics and Physics of Solids*, **56**(1):200–214, 2008. 13

[52] Michael Griebel and Marc Alexander Schweitzer. **A particle-partition of unity method for the solution of elliptic, parabolic, and hyperbolic PDEs**. *SIAM Journal on Scientific Computing*, **22**(3):853–890, 2000. 9

[53] S. Guinard, O. Allix, D. Gudra-Degeorges, and A. Vinet. **A 3D damage analysis of low-velocity impacts on laminated composites**. *Composites Science and Technology*, **62**(4):585–589, 2002. 14

[54] J Halpin, N Pagano, J Whitney, and E Wu. **Characterization of anisotropic composite materials**. In *Composite Materials: Testing and Design*. ASTM International, 1969. 16

[55] Anita Hansbo and Peter Hansbo. **A finite element method for the simulation of strong and weak discontinuities in solid mechanics**. *Computer Methods in Applied Mechanics and Engineering*, **193**(33-35):3523–3540, August 2004. 14

[56] Z. Hashin. **FAILURE CRITERIA FOR UNIDIRECTIONAL FIBER COMPOSITES.** *Journal of Applied Mechanics, Transactions ASME*, **47**(2):329–334, 1980. 33

[57] Z. Hashin and a. Rotem. **A Fatigue Failure Criterion for Fiber Reinforced Materials**. *Journal of Composite Materials*, **7**(4):448–464, October 1973. 7

[58] Z. Hashin and A. Rotem. **FATIGUE FAILURE CRITERION FOR FIBER REINFORCED MATERIALS.** *Journal of Composite Materials*, **7**:448–464, 1973. 33

[59] Sorensen Hibbett, Karlsson. *ABAQUS/standard: User's Manual*, **1**. Hibbitt, Karlsson & Sorensen, 1998. 23

[60] Hibbitt, Karlsson, and Sorensen. *ABAQUS/Standard user's manual*, **1**. Hibbitt, Karlsson & Sorensen, 2001. 50, 51, 53, 64

[61] Rodney Hill. *The mathematical theory of plasticity*. Oxford: Clarendon Press, 1983. 6

[62] M. J Hinton, A.S Kaddour, and P.D Soden. *Failure criteria in fibre reinforced polymer composites: the world-wide failure exercise*. Elsevier, 2004. 15

[63] M.J. Hinton, A.S. Kaddour, and P.D. Soden. **A comparison of the predictive capabilities of current failure theories for composite laminates, judged against experimental evidence**. *Composites Science and Technology*, **62**(12-13 SPECIAL ISSUE):1725–1797, 2002. 7

[64] M.J. Hinton, A.S. Kaddour, and P.D. Soden. **A further assessment of the predictive capabilities of current failure theories for composite laminates: Comparison with experimental evidence**. *Composites Science and Technology*, **64**(3-4):549–588, 2004. 7

[65] M.J. Hinton and P.D. Soden. **Predicting failure in composite laminates: the background to the exercise**. *Composites Science and Technology*, **58**(7):1001–1010, 1998. 7

[66] Oscar Hoffman. **The brittle strength of orthotropic materials**. *Journal of Composite Materials*, **1**(2):200–206, 1967. 7

[67] R. Huang, N. Sukumar, and J.-H. Prvost. **Modeling quasi-static crack growth with the extended finite element method Part II: Numerical applications**. *International Journal of Solids and Structures*, **40**(26):7539–7552, 2003. 105

[68] Thomas J R Hughes. *The finite element method : linear static and dynamic finite elment analysis*. Mineola, NY : Dover Publications, 2000, Mineola, NY, 2000. 117

[69] N. Iosipescu. **New accurate procedure for single shear testing of metals**. *Journal of Materials*, **2(3)**:537–66, 1967. 20

[70] Milan Jirásek and Thomas Zimmermann. **Analysis of rotating crack model**. *Journal of engineering mechanics*, **124**(8):842–851, 1998. 16

[71] A.F. Johnson, A.K. Pickett, and P. Rozycki. **Computational methods for predicting impact damage in composite structures**. *Composites Science and Technology*, **61**(15):2183–2192, 2001. 14

[72] Robert M Jones. *Mechanics of composite materials*, **1**. McGraw-Hill New York, 1975. 1

[73] L M Kachanov. **On the time to failure under creep conditions, Izv**. *AN SSSR, Otd. Tekhn. Nauk*, **8**:26–31, 1958. 8

[74] László P Kollár and George S Springer. *Mechanics of composite structures*. Cambridge university press, 2003. 4

[75] H. Krenchel. *Fibre Reinforcement*. Copenhagen: Akademisk Forlag, 1964. 66

[76] S. Krenk. *Non-Linear Analysis with Finite Elements*. Aalborg University, Aalborg, 1993. 7

[77] Ireneusz Lapczyk and Juan A Hurtado. **Progressive damage modeling in fiber-reinforced materials**. *Composites Part A: Applied Science and Manufacturing*, **38**(11):2333–2341, 2007. 8, 32, 33

[78] AA Lebedev and NR Muzyka. **Design of cruciform specimens for fracture toughness tests in biaxial tension (Review)**. *Strength of materials*, **30**(3):243–254, 1998. 16

[79] Jean Lemaitre and Jean-Louis Chaboche. *Mechanics of solid materials*. Cambridge university press, 1994. 8, 62

[80] Stolarska M., Chopp D.L., Mos N., and Belytschko T. **Modelling crack growth by level sets in the extended finite element method**. *International Journal for Numerical Methods in Engineering*, **51**(8):943–960, 2001. 89

[81] P. Maimí, P.P. Camanho, J.a. Mayugo, and C.G. Dávila. **A continuum damage model for composite laminates: Part I Constitutive model**. *Mechanics of Materials*, **39**(10):897–908, October 2007. 8

[82] P. Maimí, P.P. Camanho, J.a. Mayugo, and C.G. Dávila. **A continuum damage model for composite laminates: Part II Computational implementation and validation**. *Mechanics of Materials*, **39**(10):909–919, October 2007. 8

REFERENCES

[83] P. Maimi, J.a. Mayugo, and P.P. Camanho. **A Three-dimensional Damage Model for Transversely Isotropic Composite Laminates**. *Journal of Composite Materials*, **42**(25):2717–2745, September 2008. 8

[84] Andreas Makris, Carla Ramault, Danny Van Hemelrijck, Dimitrios Zarouchas, Ebrahim Lamkanfi, and Wim Van Paepegem. **An investigation of the mechanical behavior of carbon epoxy cross ply cruciform specimens under biaxial loading**. *Polymer Composites*, **31**(9):1554–1561, 2010. 16

[85] a. Matzenmiller, J. Lubliner, and R.L. Taylor. **A constitutive model for anisotropic damage in fiber-composites**. *Mechanics of Materials*, **20**(2):125–152, April 1995. 8

[86] ALJTR Matzenmiller, J Lubliner, and RL Taylor. **A constitutive model for anisotropic damage in fiber-composites**. *Mechanics of materials*, **20**(2):125–152, 1995. 32

[87] J Mediavilla, RHJ Peerlings, and MGD Geers. **Discrete crack modelling of ductile fracture driven by non-local softening plasticity**. *International journal for numerical methods in engineering*, **66**(4):661–688, 2006. 16

[88] Jens Markus Melenk and Ivo Babuška. **The partition of unity finite element method: basic theory and applications**. *Computer methods in applied mechanics and engineering*, **139**(1):289–314, 1996. 9

[89] T. Menouillard, J. Rthor, A. Combescure, and H. Bung. **Efficient explicit time stepping for the eXtended Finite Element Method (X-FEM)**. *International Journal for Numerical Methods in Engineering*, **68**(9):911–939, 2006. 83, 84, 85, 96, 97

[90] J Mergheim, E Kuhl, and P Steinmann. **Towards the algorithmic treatment of 3D strong discontinuities**. *International Journal for Numerical Methods in Biomedical Engineering*, **23**(2):97–108, 2007. 15

[91] Julia Mergheim, Ellen Kuhl, and Paul Steinmann. **A finite element method for the computational modelling of cohesive cracks**. *International Journal for Numerical Methods in Engineering*, **63**(2):276–289, 2005. 15

[92] C. Miehe, F. Welschinger, and M. Hofacker. **Thermodynamically consistent phase-field models of fracture: Variational principles and multi-field FE implementations**. *International Journal for Numerical Methods in Engineering*, **83**(10):1273–1311, 2010. 15

[93] Christian Miehe, Martina Hofacker, and Fabian Welschinger. **A phase field model for rate-independent crack propagation: Robust algorithmic implementation based on operator splits**. *Computer Methods in Applied Mechanics and Engineering*, **199**(45):2765–2778, 2010. 15

[94] N. Moës and T. Belytschko. **Extended finite element method for cohesive crack growth**. *Engineering Fracture Mechanics*, **69**(7):813–833, 2002. 13

[95] N. Moës, J. Dolbow, and T. Belytschko. **A finite element method for crack growth without remeshing**. *International Journal for Numerical Methods in Engineering*, **46**(1):131–150, 1999. 10, 82, 92

[96] Nicolas Moës, John Dolbow, and Ted Belytschko. **A finite element method for crack growth without remeshing**. *International Journal for Numerical Methods in Engineering*, **46**(1):131–150, 1999. 9

[97] B. Moran and C.F. Shih. **Crack tip and associated domain integrals from momentum and energy balance**. *Engineering Fracture Mechanics*, **27**(6):615–642, 1987. 87

[98] Sukumar N. and Prvost J.-H. **Modeling quasi-static crack growth with the extended finite element method Part I: Computer implementation**. *International Journal of Solids and Structures*, **40**(26):7513–7537, 2003. 90

[99] J. Navarro-Zafra, J. L. Curiel-Sosa, and M. C. Serna Moreno. **Three-Dimensional Static and Dynamic Analysis of a Composite Cruciform Structure Subjected to Biaxial Loading: A Discontinuum Approach**. *Applied Composite Materials*, **23**:139–154, 2015. iv, 41, 42, 100

[100] J Navarro-Zafra, JL Curiel-Sosa, and MC Serna Moreno. **Mixed-mode damage into a CGRP cruciform subjected to biaxial loading**. *Composite Structures*, **133**:1093–1100, 2015. iv, 59

[101] Nathan M Newmark. **A method of computation for structural dynamics**. *Journal of the Engineering Mechanics Division*, **85**(3):67–94, 1959. 82

[102] G. Odegard and M. Kumosa. **Determination of shear strength of unidirectional composite materials with the Iosipescu and 10off-axis shear tests**. *Composites Science and Technology*, **60**(16):2917–2943, 2000. 20

[103] J.Tinsley Oden, Ted Belytschko, Ivo Babuska, and T.J.R. Hughes. **Research directions in computational mechanics**. *Computer Methods in Applied Mechanics and Engineering*, **192**(7-8):913–922, February 2003. 1, 81

[104] S. Osher and J.A. Sethian. **Fronts propagating with curvature-dependent speed: Algorithms based on Hamilton-Jacobi formulations**. *Journal of Computational Physics*, **79**(1):12–49, 1988. 89

[105] Niels Saabye Ottosen. *Introduction to the finite element method*. Hemel Hempstead : Prentice Hall, 1992, Hemel Hempstead, 1992. 117

[106] NJ Pagano and JC Halpin. **Influence of end constraint in the testing of anisotropic bodies**. *Journal of Composite Materials*, **2**(1):18–31, 1968. 20

[107] M. Pais. **MATLAB Extended Finite Element (MXFEM) code V1.2**. 2011. 89

[108] B. Pan, K. Qian, H. Xie, and A. Asundi. **Two-dimensional digital image correlation for in-plane displacement and strain measurement: A review**. *Measurement Science and Technology*, **20**(6), 2009. 29

[109] RHJ Peerlings, R De Borst, WAM Brekelmans, JHP De Vree, and I Spee. **Some observations on localisation in non-local and gradient damage models**. *EUROPEAN JOURNAL OF MECHANICS SERIES A SOLIDS*, **15**:937–954, 1996. 16

[110] W.H. Peters and W.F. Ranson. **DIGITAL IMAGING TECHNIQUES IN EXPERIMENTAL STRESS ANALYSIS.** *Optical Engineering*, **21**(3):427–431, 1982. 29

[111] F. Pierron and A. Vautrin. **Measurement of the in-plane shear strengths of unidirectional composites with the iosipescu test**. *Composites Science and Technology*, **57**(12):1653–1660, 1998. 20, 21

[112] A Puck and H Schürmann. **FAILURE ANALYSIS OF FRP LAMINATES BY MEANS OF PHYSICALLY BASED PHENOMENOLOGICAL MODELS** . **3538**(96), 1998. 7

[113] Xinlin Qing, Hsien-Tang Sun, Louis Dagba, and Fu-Kuo Chang. **Damage-tolerance-based design of bolted composite joints**. In *Composite Structures: Theory and Practice*. ASTM International, 2001. 8

[114] Timon Rabczuk, Stéphane Bordas, and Goangseup Zi. **On three-dimensional modelling of crack growth using partition of unity methods**. *Computers & structures*, **88**(23):1391–1411, 2010. 13

[115] Timon Rabczuk, Goangseup Zi, Axel Gerstenberger, and Wolfgang A Wall. **A new crack tip element for the phantom-node method with arbitrary cohesive cracks**. 2008. 15

[116] John William Strutt Baron Rayleigh. *The theory of sound*, **2**. Macmillan, 1896. 86

[117] Peter Reřicha. **OPTIMUM LOAD TIME HISTORY FOR NON-LINEAR ANALYSIS USING DYNAMIC RELAXATION.** *International Journal for Numerical Methods in Engineering*, **23**(12):2313–2324, 1986. 82

[118] A Riccio. **Effects of geometrical and material features on damage onset and propagation in single-lap bolted composite joints under tensile load: part II–numerical studies**. *Journal of composite materials*, **39**(23):2091–2112, 2005. 8

[119] James R Rice. **A path independent integral and the approximate analysis of strain concentration by notches and cracks**. *Journal of applied mechanics*, **35**(2):379–386, 1968. 87

[120] Antonio Rodrguez-Ferran and Antonio Huerta. **Error estimation and adaptivity for nonlocal damage models**. *International Journal of Solids and Structures*, **37**(48):7501–7528, 2000. 67

[121] D. Rooke, D.J. Cartwright, and Great Britain Ministry of Defence. *Compendium of stress intensity factors*. London: H.M.S.O., 1976. 51

[122] David Percy Rooke and David John Cartwright. **Compendium of stress intensity factors**. *Procurement Executive, Ministry of Defence. H. M. S. O. 1976, 330 p(Book).*, 1976. 97

[123] Simon-Nicolas Roth, Pierre Léger, and Azzeddine Soulaïmani. **A combined XFEM–damage mechanics approach for concrete crack propagation**. *Computer Methods in Applied Mechanics and Engineering*, **283**:923–955, 2015. 16, 17

[124] J.C.J. Schellekens and R. De Borst. **A non-linear finite element approach for the analysis of mode-I free edge delamination in composites**. *International Journal of Solids and Structures*, **30**(9):1239–1253, 1993. 14

[125] M. C. Serna Moreno, J. L. Curiel-Sosa, J. Navarro-Zafra, J. L. Martínez Vicente, and J. J. López Cela. **Crack propagation in a chopped glass-reinforced composite under biaxial testing by means of XFEM**. *Composite Structures*, 2014. 42, 44, 67, 100

[126] M. C. Serna Moreno and J. J. López Cela. **Failure envelope under biaxial tensile loading for chopped glass-reinforced polyester composites**. *Composites Science and Technology*, **72**(1):91–96, 2011. vii, 42, 44, 48, 50, 63, 97

[127] M. C. Serna Moreno, J. L. Martínez Vicente, and J. J. López Cela. **Failure strain and stress fields of a chopped glass-reinforced polyester under biaxial loading**. *Composite Structures*, **103**:27–33, 2013. 42, 43, 63

[128] M.C. Serna Moreno, José Luis Curiel-Sosa, and Joaquín Navarro-Zafra. **Initiation and evolution of cracks in a chopped glass reinforced composite under biaxial testing by means of XFEM**. In *16th European Conference on Composite Materials. Seville, Spain, 22 June 2014 - 26 June 2014.*, number June, 2014. 67

[129] J C Simo and J W Ju. **Strain-and stress-based continuum damage modelsI. Formulation**. *Mathematical and Computer Modelling*, **12**(3):378, 1989. 8

[130] Juan C Simo and Thomas JR Hughes. *Computational inelasticity*, **7**. Springer Science & Business Media, 2006. 7

[131] A Smits, C Ramault, A Makris, D Van Hemelrijck, A Clarke, and Williamson et al. **A review of biaxial test methods for composites**. In *Experimental Analysis of Nano and Engineering Materials and Structures*, pages 933–934. Springer, 2007. 16

[132] P D Soden, M J Hinton, and A S Kaddour. **Biaxial test results for strength and deformation of a range of E-glass and carbon fibre reinforced composite laminates: failure exercise benchmark data**. *Composites Science and Technology*, **62**(12):1489–1514, 2002. 16, 42

[133] P.D. Soden, M.J. Hinton, and A.S. Kaddour. **A comparison of the predictive capabilities of current failure theories for composite laminates**. *Composites Science and Technology*, **58**(7):1225–1254, 1998. 7

[134] P.D. Soden, M.J. Hinton, and A.S. Kaddour. **Lamina properties, lay-up configurations and loading conditions for a range of fibre-reinforced composite laminates**. *Composites Science and Technology*, **58**(7):1011–1022, 1998. xi, 79, 81

[135] S Mohammadi (Soheil). *Extended finite element method for fracture analysis of structures*. Oxford : Blackwell, c2008, Oxford, 2008. 13

REFERENCES

[136] Jeong-Hoon Song, Pedro Areias, and Ted Belytschko. **A method for dynamic crack and shear band propagation with phantom nodes**. *International Journal for Numerical Methods in Engineering*, **67**(6):868–893, 2006. 15

[137] Jeong-Hoon Song and Ted Belytschko. **Dynamic fracture of shells subjected to impulsive loads**. *Journal of Applied Mechanics*, **76**(5):051301, 2009. 15

[138] JeongHoon Song, Pedro Areias, and Ted Belytschko. **A method for dynamic crack and shear band propagation with phantom nodes**. *International Journal for Numerical Methods in Engineering*, **67**(6):868–893, 2006. 14

[139] N Sukumar, N Moës, B Moran, and T Belytschko. **Extended Finite element method for three-dimensional crack modelling**. (November 1999):1549–1570, 2000. 13

[140] C.T. Sun and I. Chung. **An oblique end-tab design for testing off-axis composite specimens**. *Composites*, **24**(8):619–623, 1993. 20, 21

[141] M. Sutton, C. Mingqi, W. Peters, Y. Chao, and S. McNeill. **Application of an optimized digital correlation method to planar deformation analysis**. *Image and Vision Computing*, **4**(3):143–150, 1986. 29

[142] S.R. Swanson, M. Messick, and G.R. Toombes. **Comparison of torsion tube and Iosipescu in-plane shear test results for a carbon fibre-reinforced epoxy composite**. *Composites*, **16**(3):220–224, 1985. 20

[143] W. Tong. **An evaluation of digital image correlation criteria for strain mapping applications**. *Strain*, **41**(4):167–175, 2005. 30

[144] S. W. Tsai and E. M. Wu. **A General Theory of Strength for Anisotropic Materials**. *Journal of Composite Materials*, **5**(1):58–80, January 1971. 7

[145] KI Tserpes, P Papanikos, and Th Kermanidis. **A three-dimensional progressive damage model for bolted joints in composite laminates subjected to tensile loading**. *Fatigue & Fracture of Engineering Materials & Structures*, **24**(10):663–675, 2001. 8

[146] F.P. Van Der Meer and L.J. Sluys. **Continuum models for the analysis of progressive failure in composite laminates**. *Journal of Composite Materials*, **43**(20):2131–2156, 2009. 38, 101

[147] F.P. van der Meer and L.J. Sluys. **A phantom node formulation with mixed mode cohesive law for splitting in laminates**. *International Journal of Fracture*, **158**(2):107–124, 2009. 101

[148] Danny Van Hemelrijck, Andreas Makris, Carla Ramault, Ebrahim Lamkanfi, Wim Van Paepegem, and D Lecompte. **Biaxial testing of fibre-reinforced composite laminates**. *Proceedings of the Institution of Mechanical Engineers, Part L: Journal of Materials Design and Applications*, **222**(4):231–239, 2008. 16

[149] W. Van Paepegem, I. De Baere, and J. Degrieck. **Modelling the nonlinear shear stress-strain response of glass fibre-reinforced composites. Part I: Experimental results**. *Composites Science and Technology*, **66**(10):1455–1464, 2006. 20

[150] W. Van Paepegem, I. De Baere, and J. Degrieck. **Modelling the nonlinear shear stress-strain response of glass fibre-reinforced composites. Part II: Model development and finite element simulations**. *Composites Science and Technology*, **66**(10):1465–1478, 2006. 20

[151] Jack R Vinson and Robert L Sierakowski. *The behavior of structures composed of composite materials*, **5**. Springer Science & Business Media, 2012. 1

[152] J.S. Welsh and D.F. Adams. **An experimental investigation of the biaxial strength of IM6/3501-6 carbon/epoxy cross-ply laminates using cruciform specimens**. *Composites - Part A: Applied Science and Manufacturing*, **33**(6):829–839, 2002. 16

[153] HM Westergaard. **Bearing Pressures and Cra; c];¡ si**. *Journal of applied mechanics*, 1939. 88

[154] ML Williams. **The bending stress distribution at the base of a stationary crack**. *Journal of applied mechanics*, **28**(1):78–82, 1961. 88

[155] M R Wisnom. **Modelling discrete failures in composites with interface elements**. *Composites Part A: Applied Science and Manufacturing*, **41**(7):795–805, 2010. 14

[156] J.C. Xavier, N.M. Garrido, M. Oliveira, J.L. Morais, P.P. Camanho, and F. Pierron. **A comparison between the Iosipescu and off-axis shear test methods for the characterization of Pinus Pinaster Ait**. *Composites Part A: Applied Science and Manufacturing*, **35**(7-8):827–840, 2004. 20

[157] Yi Xiao and T Ishikawa. **Bearing failure in bolted composite joints: analytical tools development**. *Advanced Composite Materials*, **11**(4):375–391, 2002. 8

[158] Yong Yu, Min Wan, Xiang-Dong Wu, and Xian-Bin Zhou. **Design of a cruciform biaxial tensile specimen for limit strain analysis by FEM**. *Journal of Materials Processing Technology*, **123**(1):67–70, 2002. 16

Publications

Journal publications

- **Navarro-Zafra J**,Curiel-Sosa J.L.,Serna Moreno M.C.(2015). Three-dimensional static and dynamic analysis of a composite cruciform structure subjected to biaxial loading: a discontinuum approach. DOI: 10.1007/s10443-015-9453-4
- **Navarro-Zafra J**,Curiel-Sosa J.L.,Serna Moreno M.C.. Mixed-mode damage into a CGRP cruciform subjected to biaxial loading. Composite Structures, 2015, vol. 133, p. 1093-1100.
- Serna Moreno MC, Curiel-Sosa JL, **Navarro-Zafra J**, Martinez Vicente JL Lopez Cela JJ (2015) "Crack propagation in a chopped glass-reinforced composite under biaxial testing by means of XFEM". Composite Structures, 119, 264-271.

Conference papers

- **Navarro-Zafra J**, Curiel-Sosa JL Serna Moreno MC (2015) "3D Crack analysis of a CGRP cruciform under biaxial loading using two numerical approaches: XFEM and PDM". 23rd UK Conference of the Association for Computational Mechanics in Engineering. Swansea, 8 April 2015 - 10 April 2015.
- **Navarro-Zafra J**, Curiel-Sosa JL Serna Moreno MC (2014) "3D crack analysis of a chopped glass-reinforced polyester cruciform specimen under biaxial loading using two different numerical techniques for modelling cracks: XFEM and a progressive damage model". 18th International Conference on Composite Structures (ICCS18). Lisbon, Portugal, 15 June 2015 - 19 June 2015.

REFERENCES

- **Navarro-Zafra J**, Curiel-Sosa J, Serna Moreno MC, Pinna C, Martinez Vicente JL, Rohaizat N, Tafazzolimoghaddam B (2016) An approach for dynamic analysis of stationary cracks using XFEM. Proceedings of the 24th UK Conference of the Association for Computational Mechanics in Engineering. Cardiff, UK, 31 March 2016 - 1 May 2016.

- Tafazzolimoghaddam B, Curiel-Sosa JL **Navarro-Zafra J** (2015) "On the calculation of energy release rates in composite laminates by Finite Elements, Boundary Elements and Analytical Methods", 23rd UK Conference of the Association for Computational Mechanics in Engineering. Swansea, 8 April 2015 - 10 April 2015.

- Curiel-Sosa JL, Tafazzolimoghadam B, **Navarro-Zafra J** Serna Moreno MC (2014) "Damage and Failure in Composites". 11th World Congress on Computational Mechanics (WCCM XI). Barcelona, Spain, 20 July 2014 - 25 July 2014.

- Serna Moreno MC, Curiel-Sosa JL **Navarro-Zafra J** (2014) "Initiation and evolution of cracks in a chopped glass reinforced composite under biaxial testing by means of XFEM". 16th European Conference on Composite Materials. Seville, Spain, 22 June 2014 - 26 June 2014.

Appendix A. Finite element method

This work can be frame into the Finite Element Method (FEM) [20][68][105]. This well-known numerical method is used for obtaining approximate solutions of differential equations e.g continuum mechanics partial differential equations (PDEs). A large class of engineering problems can be solved by means of FEM e.g. stress analysis, heat transfer, fluid flow, failure in composite, etc. The standard definition of static FEM is based on the equilibrium:

$$f^{int} = f^{ext} \tag{6.1}$$

Where f^{int} represent the internal force vector which is a function of the displacement and f^{ext} is the external force vector. The fundamental unknown is the displacement u. Then, the displacement field $u^T = [u_x, u_y, u_z]$ can be written using a shape function matrix N and the nodal displacement a like;

$$u = Na \tag{6.2}$$

With

$$N = \begin{bmatrix} N_1 & 0 & 0 & N_2 & 0 & 0 & .... & N_n & 0 & 0 \\ 0 & N_1 & 0 & 0 & N_2 & 0 & .... & 0 & N_n & 0 \\ 0 & 0 & N_1 & 0 & 0 & N_2 & .... & 0 & 0 & N_n \end{bmatrix}$$

Where n is the number of nodes of the element. The strain ϵ is defined as a function of the displacement according to the following expression

$$\epsilon = Ba \tag{6.3}$$

where B is the derivative of the shape functions. The stress can be expressed as a function of the strain and the simplest relation between then it is given thought the constitutive law proposed by Hooke;

$$\sigma = D\epsilon \tag{6.4}$$

where D is the constitutive matrix of the material and σ the stresses.

In some cases, the finite element discretizations for the differential equation are nonlinear. Thus, the most common solution procedures for the nonlinear problems are implicit (e.g. Newton-Raphson) and explicit (e.g. central difference method) methods.

Solution procedures

Newton method

This method is the most used and robust for solution of nonlinear algebraic equations. It is known as Newton method and often called Newton-Raphson. For a better understanding of this procedure, it is considered the discrete momentum equation at time step n+1 for static problems:

$$0 = r(u^{n+1}, t^{n+1}) = f^{int}(u^{n+1}, t^{n+1}) - f^{ext}(u^{n+1}, t^{n+1}) \tag{6.5}$$

where $r(u^{n+1}, t^{n+1})$ is named the residual. In this equation, the acceleration is not considered in order to solve the static problem. The main unknown of the equation is the displacement u. This method is an iterative procedure where the iteration number is indicated by the subscript k, therefore, u_k is the displacement in iteration k. For the onset of the iterative process, a starting value u_o for the unknown is chosen. Considering a Taylor expansion of the residual about the value u_k, making the residual equal to zero and dropping the higher order terms than linear, the linearized model of the nonlinear equation is defined as [20]:

$$0 = r(u_k) + \frac{\partial(u_k)}{\partial u}\Delta u \tag{6.6}$$

where $\Delta u = u_{k+1} - u_k$. Finally, the value of the unknown in the iterative process for each iteration rewriting equation 6.6 is defined as;

$$u_{k+1} = u_k - \frac{r(u_k)}{\frac{\partial r(u_k)}{\partial u}} \tag{6.7}$$

In order to better understand the method, an schematic representation of the numerical procedure is presented in Figure 6.1. In this figure, it is observed the linear model which is tangent to the nonlinear residual function. It is important to mention that when it is satisfied a desired level of accuracy, the solution is obtained.

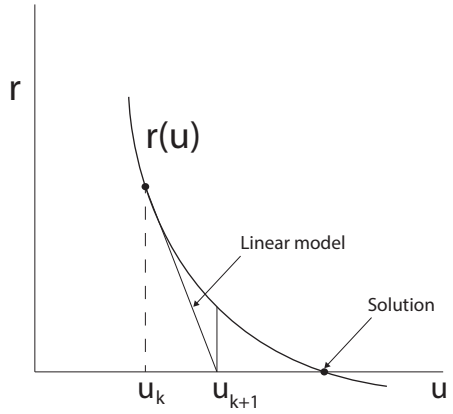

Figure 6.1: Linear model for a nonlinear equation $r(u)$.

Central difference method

The CDM is characterized for its robustness and accuracy. However, it is conditionally stable. This stability condition is called Courant condition [32] and it is presented in Equation 6.8. Then, during simulations, if the time increment Δt is bigger than the critical time step Δt_c, instabilities are present and the possible divergence of the numerical technique.

$$\Delta t_c \leq \frac{2}{\omega_{max}} \tag{6.8}$$

In Equation 6.8, ω_{max} denotes the maximum frequency of the mesh i.e. $\omega_{max} = max_{\forall(e)}\{\omega^e_{max}\}$ obtained form the eigenvalue problem given by:

$$det(\mathbb{K} - \omega^2 \mathbb{M}) = 0 \tag{6.9}$$

where $\mathbb{K}$ and $\mathbb{M}$ are the stiffness matrix and the mass matrix of the whole mesh, respectively. The CDM is developed from the central difference formulas of velocity v and acceleration a. Therefore, the time increments are defined as follows:

$$\Delta t^{n+\frac{1}{2}} = t^{n+1} - t^n, \quad t^{n+\frac{1}{2}} = \frac{1}{2}(t^{n+1} - t^n), \quad \Delta t^n = t^{n+\frac{1}{2}} - t^{n-\frac{1}{2}} \tag{6.10}$$

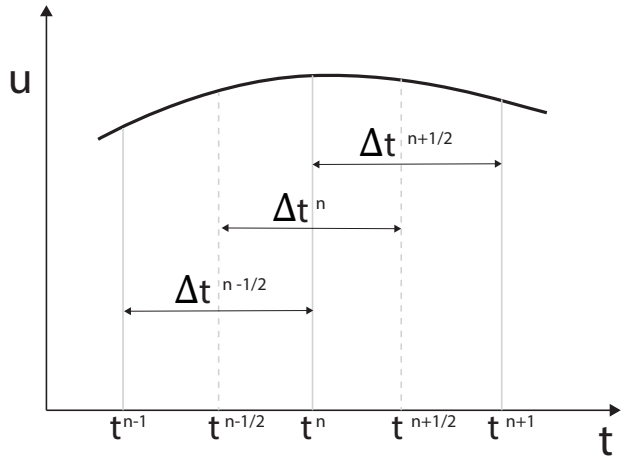

Figure 6.2: Discretization used in central difference scheme.

The definition of those time increments is better understood referring to Figure 6.2. According to this graph, the central difference formula for velocity at the mid-step, $\dot{u}^{n+\frac{1}{2}}$ given by Eq.(6.11) and acceleration for time step n, $\ddot{u}^n$ given by Eq.(6.12) are defined as,

$$\dot{u}^{n+\frac{1}{2}} = \frac{u^{n+1} - u^n}{t^{n+1} - t^n} = \frac{1}{\Delta t^{n+\frac{1}{2}}}(u^{n+1} - u^n) \rightarrow u^{n+1} = u^n + \Delta t^{n+\frac{1}{2}} \dot{u}^{n+\frac{1}{2}} \tag{6.11}$$

$$\ddot{u}^n = a^n = \frac{v^{n+\frac{1}{2}} - v^{n-\frac{1}{2}}}{t^{n+\frac{1}{2}} - t^{n-\frac{1}{2}}}) \rightarrow v^{n+\frac{1}{2}} = v^{n-\frac{1}{2}} + \Delta t^n a^n \tag{6.12}$$

Taking into account the time integration in the equation of motion for a given time step n, it is derived the following equation:

$$Ma^n = f^{ext,n} - f^{int,n} \tag{6.13}$$

where $f^{ext,n}$ and $f^{int,n}$ are the external and internal nodal forces respectively for a time step n. The external and internal forces are functions of the time and the displacement.

Appendix B. Subroutine for the implementation of the PDM within the in-house code

```
function [Dw,w,sig,phi,eps] = PDM(epse,w,dt,it,teta)

global LAMINA

% Declare static variables
persistent epsOld  sigOld

% Rotate strain into the local coordinate
[eps_rot] = rotate_strain(eps,teta);

if it==1
 epsOld(1:3,1)=0;
 sigOld(1:3,1)=0;
end

% Plane stress lamina
E1= LAMINA(1);
E2= LAMINA(2);
G12= LAMINA(3);
v12= LAMINA(4);
v21=(E2/E1)*v12;

C11= E1/(1-v12*v21);
C12= (v12*E2)/(1-v12*v21);
C22= E2/(1-v12*v21);
C33= 2*G12;
```

```
    D = [C11 C12   0;...
         C12 C22   0;...
         0   0 C33];
     X11 = LAMINA(5);
     X22 = LAMINA(6);
     S12 = LAMINA(7);
     % Strenght parameters
     strengh = [ X11; X22;S12];

% Unitary directors of damage
q = zeros(3);

% Fibre rupture
q(1,1)=1; q(3,1)=0;
% Matrix cracking first transverse direction
q(2,2)=0; q(3,2)=0;

% Strain rate
e_rate = (eps_rot'-epsOld') / dt ;


% Damage diagonal tensor
for i=1:3
    M(i,i)=1/(1-w(i));
end
%'Damaged' stiffness tensor
Dw = inv(M)*D;

% Constitutive law
 sig = Dw*eps_rot;
% F matrices derived from stress-based classical failure criteria
F = zeros(3,3,3);
%     Fibre rupture (t) F(,,1)
       F(1,1,1)=1/((1-w(1))^2*X11^2);
       F(3,3,1)=1/((1-w(3))^2*S12^2);
%     Matrix cracking in first transverse direction (t) F(,,3)
       F(2,2,2)=1/((1-w(2))^2*X22^2);
       F(3,3,2)=1/((1-w(3))^2*S12^2);

% G matrix
for j=1:3
G(:,:,j)=Dw'*F(:,:,j)*Dw;
A(:,:)=G(:,:,j);
```

```
B=A';
% Gradient vectors: Nabla_g
Nabla_cols_g(j,:)=eps_rot'*(A+B);
Nabla_g=Nabla_cols_g';
end
% Damage growth functions
phi=e_rate*Nabla_g;
%  Damage rule
w_rate=phi(1)*q(:,1)+phi(2)*q(:,2)+phi(3)*q(:,3);
% Yield
for i=1:2
    if sig(i)>=0
        if (sig(i)-sigOld(i)>=0) && (sig(i)<strengh(i))
            w_rate(i)=0;
        end
    else
        if (sig(i)-sigOld(i)<0) && (sig(i)> (-1)*strengh(i))
            w_rate(i)=0;
        end
    end
end


% Update damage
w=w+w_rate'*dt;
% Upperbound for damage variables
for i=1:3
    if w(i)>1.
        w(i)=0.999999;
    elseif w(i)<0.
        w(i)=0;
    end
end
% Update persistent variables
sigOld=sig;
epsOld=eps_rot;
```

Appendix C. General view of the Matlab code for the mass matrix construction

```
function [globalMass] = Mass_XFEM(DOF,EE,anglecrack)
% DOF = Total Degree of Freedom (DOF) in the model
% EE = Enriched elements
% anglecrack = Angle of the crack respect to the horizontal


 % Define the global Mass matrix
globalMass = sparse(DOF,DOF);
globalDOF=DOF;

% Definition of variables
[row_index,col_index,totalsize,nElemX,nElemY] = Initializate(DOF,EE);
nIndex  = 0;

 % Loop over elements
 for el = 1:(nElemY*nElemX)

% Nodes for each element, nodal information
 [n1,n2,n3,n4,nnenriched,elem_data] = NODES_id(el,EE);

 local_Mass = 0;
 % Locations
 local  = [n1*2-1 n1*2 n2*2-1 n2*2 n3*2-1 n3*2 n4*2-1 n4*2];
 id_Loc   = 9;

  if (nnenriched == 0)
     % Unenriched nodes (traditional FE)
```

```
    [M_FEM] = mass_element_FEM_XFEM(el);
    % Mass matrix of element without enrichment
    local_Mass = M_FEM;

  elseif nnenriched > 0
      % Enriched nodes
      [M_FEM] = mass_element_FEM_XFEM(el);
       M_enr = [];

       index=1;
       for i = 1:4 % Loop over nodes
         if elem_data(i,2) ~= 0
         % Heaviside enrichment.

              [M_heavi] = mass_heaviside_XFEM(el);

              M_enr(index:(index+1),index:(index+1)) = M_heavi;
              index = index+2;

local(id_Loc:(id_Loc+1)) = [2*elem_data(i,2)-1 2*elem_data(i,2)];
              id_Loc = id_Loc+2;

          elseif elem_data(i,4) ~= 0
         % Crack-tip enrichment
         [ M_ct] = mass_tip_XFEM (el,i,anglecrack);
              M_enr(index:(index+7),index:(index+7)) = M_ct;
              index = index+8;

 local(id_Loc:(id_Loc+7)) = [2*elem_data(i,4)-1 2*elem_data(i,4)...
               2*elem_data(i,6)-1  2*elem_data(i,6)...
              2*elem_data(i,8)-1 2*elem_data(i,8) ...
              2*elem_data(i,10)-1 2*elem_data(i,10)];
              id_Loc = id_Loc+8;

         end
       end
  % End loop over nodes

  % Mass matrix of the element
       local_Mass = [ M_FEM zeros(rows(M_FEM),cols(M_enr));...
       zeros(rows(M_enr),cols(M_FEM)) M_enr];
  end
```

```
      if length(local_Mass) == 8
    % Unenriched element
        for i = 1:8
            for j = 1:8
                nIndex = nIndex+1;
                row_index(nIndex) = local(i);
                col_index(nIndex) = local(j);
                totalsize(nIndex) = local_Mass(i,j);
            end
        end
      else

        globalMass(local,local) = globalMass(local,local) + local_Mass;
    end

 end
 % end loop over elements
   globalMass = globalMass +
   sparse(row_index,col_index,totalsize,globalDOF,globalDOF);
end
```

Appendix D. General view of the Matlab code for the stiffness matrix construction

```
function [globalK] = KMatrix_XFEM(anglecrack,DOF,EE)

globalK = sparse(DOF,DOF);
[K_FEM,D,row_index,col_index,totalsize,nElemX,nElemY]= initia(DOF,EE);
index_G  = 0;

for el = 1:(nElemY*nElemX)

 % Nodes for each element, nodal information
 [n1,n2,n3,n4,nnenriched,elem_data] = NODES_id_K(el,EE);

 % Initizalize K
    local_K = 0;
    local  = [n1*2-1 n1*2 n2*2-1 n2*2 n3*2-1 n3*2 n4*2-1 n4*2];
    id_Loc   = 9;
    if (nnenriched == 0)
   % Unenriched element
    local_K=K_FEM;

    elseif nnenriched > 0
    % Enriched element
    [x1,y1,x2,y2,x3,y3,x4,y4] = coord(n1,n2,n3,n4);

        if nnenriched == 4
        % Fully enriched element
[gauss_p,weight,Jaco] = gauss_jaco_weight(x1,x2,x3,x4,y1,y2,y3,y4,el);
```

```
        else
         % Partially enriched element
        [gauss_p,weight,Jaco]= partially;
        end
        % Loop over gauss points
        for i = 1:length(gauss_p)
            W = weight(i);
[N_x,N_y,X_gauss,Y_gauss,N,detJ]=
derivative(gauss_p,weight,Jaco,i,x1,x2,x3,x4,y1,y2,y3,y4);

      Bu = [N_x(1)   0   N_x(2)   0   N_x(3)   0   N_x(4)   0;...
              0   N_y(1)   0   N_y(2)   0   N_y(3)   0   N_y(4);...
            N_y(1) N_x(1) N_y(2) N_x(2) N_y(3) N_x(3) N_y(4) N_x(4)];
            B_Enr = [];

            indice = 1;
            % Loop over nodes
            for node = 1:4
                if elem_data(node,2) ~= 0
                    [H]= heavi(N,elem_data,node,n1,n2,n3,n4);

                    Ba = [N_x(node)*H      0;
                                0     N_y(node)*H;
                          N_y(node)*H N_x(node)*H];
                    B_Enr(:,indice:(indice+1)) = Ba;
                    indice = indice+2;

                    if (i == length(gauss_p))
local(id_Loc:(id_Loc+1)) = [2*elem_data(node,2)-1 2*elem_data(node,2)];
                        id_Loc = id_Loc+2;
                    end
                elseif elem_data(node,4) ~= 0
[B_ct]= ...
B_crack_tip(anglecrack,X_gauss,Y_gauss,node,i,elem_data,id_Loc,gauss_p,
N,N_x,N_y,indice);

                    B_Enr(:,indice:(indice+7)) = B_ct;

                    indice = indice+8;

                    if (i == length(gauss_p))
 local(id_Loc:(id_Loc+7)) = [2*elem_data(node,4)-1 2*elem_data(node,4) ...
```

```
 2*elem_data(node,6)-1   2*elem_data(node,6)...
 2*elem_data(node,8)-1  2*elem_data(node,8)  ...
 2*elem_data(node,10)-1  2*elem_data(node,10)];
                                id_Loc = id_Loc+8;
                        end
                    end
                end

                B = [Bu B_Enr];
                local_K = local_K + W*B'*D*B*detJ;
            end
        end
        if length(local_K) == 8
            % FEM element
            for i = 1:8
                for j = 1:8
                    index_G = index_G+1;
                    row_index(index_G) = local(i);
                    col_index(index_G) = local(j);
                    totalsize(index_G) = local_K(i,j);
                end
            end
        else
            globalK(local,local) = globalK(local,local) + local_K;
        end
end

globalK = globalK + sparse(row_index,col_index,totalsize,DOF,DOF);
```